Universitat Autònoma de Barcelona

UAB CEI CAMPUS OF INTERNATIONAL EXCELLENCE

# Synthesis of Microwave Circuits Based on Metamaterials Using Aggressive Space Mapping Algorithms


**Ph.D. Thesis written by**

**Jordi Selga Ruiz**

**Under the supervision of**

**Ferran Martín Antolín**


cimitec


Bellaterra (Cerdanyola del Vallès), September 2013



The undersigned, Prof. **Ferran Martín Antolín**

Professor of the Electronic Engineering Department (Engineering School) of the *Universitat Autònoma de Barcelona*,

**CERTIFY**:

That the thesis entitled "*Synthesis of microwave circuits based on metamaterials using Aggressive Space Mapping algorithms*" has been written by **Jordi Selga Ruiz** under his supervision.

And hereby to acknowledge the above, sign the present.

**Signature:** Ferran Martín Antolín

Bellaterra, September 27th 2013.

# Contents

# Acknowledgements

The present work was possible thanks to many people who helped me during these last years, and hence this also belongs in part to them.

I would like to give special thanks to my supervisor, Prof. Ferran Martín for his constant guidance, help and never-ending novel ideas. Thank you Ferran for your confidence and for your mentoring during these years through your explanations and interesting discussions. Also, I would like to thank Ana Rodríguez and Prof. Vicente Boria, from *Universitat Politècnica de València*, who have been working with us side by side during this period, forming a solid collaboration. Also, I would like do mention AURORASAT S.L. for supporting this work.

I also want to thank the people from GEMMA/CIMITEC, the Electronic Engineering Department and *Escola d'Enginyeria*, for their support and for providing me good times. Paris, Simone, J. Naqui, Núria, Yepes, Vanessa, Eloi, Gabriel, M. López, J. Agustí, J. Giner, G. Sisó and J. Hellín. I have to give special mention to M. Durán-Sindreu who has worked with me in several occasions, F. Paredes for his technical help, G. Zamora for his support, and J. Bonache for having solved my innumerable questions.

It is noteworthy that, without the initial guidance of M. Gil, who introduced me in the research world, the present work would have never been possible. Thank you Marta!

Of course, I also want to express my gratitude to my family and to all my friends who helped me with their affection and understanding.

And last, but not least, this is also a tribute to two persons who, wherever they are, they have always guided me . *In memoriam,* Carme Casarramona and Dra. Dolors Selga.

# Summary

In microwave engineering some of the main challenges are size reduction and design flexibility. These are key aspects in communication devices and, as a result, many efforts have been made in this direction. A clear example of that are the so-called transmission lines based on metamaterials. Such artificial lines exhibit controllable characteristics, are electrically small and provide new functionalities. However, due to their complexity, metamaterial transmission lines usually require a cumbersome design process, based on the experience of the designers. In last decades, several optimization techniques based on Space Mapping (SM), which combine the accuracy of the electromagnetic simulators with the speed of circuit simulators, have been reported. This reduces design time and provides the ability to automate the design process. For this reason, these techniques are good candidates to deal with complex problems such as the design of metamaterial transmission lines. Thus, the main objective of the work compiled in this thesis is to develop a new tool for the automated synthesis of such structures from the knowledge of the reactive elements of its equivalent circuit. Specifically, it deals with the automatic synthesis of transmission lines loaded with Complementary Split Ring Resonators (CSRRs) by using the technique known as Aggressive Space Mapping (ASM). Different strategies for the development of the ASM algorithm and its improvements are provided, including a technique to determine whether for a given set of circuit parameters that meet specifications the structure can be synthesized or not, and the reduction of the convergence time. Moreover, the ASM algorithm has been applied to the design of several microwave devices, such as Wi-Fi filters and dual-band power dividers for GSM applications, among others.

# 1

# Motivation and objectives

Artificial transmission lines based on metamaterial concepts have been a hot topic during the last years. Such lines exhibit controllable dispersion and characteristic impedance, this being the main relevant advantage as compared to conventional lines, or to other artificial transmission lines. In metamaterial transmission lines, the presence of reactive elements increases the design flexibility of the lines. However, the number of design parameters and their mutual dependence typically leads to a complex synthesis process for this kind of lines. This fact means a high design time, and nowadays it is the bottleneck for the widespread use of these structures.

Several optimization techniques for microwave circuits have been developed for a long time. One of the widely used techniques is Space Mapping (SM). This technique allows us to take advantage of the high speed of circuit simulators combined with the accuracy of electromagnetic (EM) solvers. To this end, it is necessary a good modeling of the structure under optimization. Thereby, SM techniques are revealed to be very useful for the automatic synthesis of metamaterial transmission lines, but nowadays its use is still marginal.

As previously mentioned, a key point is to find a model that describes the behavior of the structure in a wide frequency range. Furthermore, an efficient and fast parameter extraction is needed. The main idea is to merge the experience in the analysis of the aforementioned structures and the SM techniques

Accordingly, the main objective of this thesis is to demonstrate the application of SM techniques to metamaterial transmission lines. Specifically, the use of an improvement of SM technique, that is, Aggressive Space Mapping (ASM), to the synthesis of

metamaterial transmission lines based on Complementary Split Ring Resonators (CSRRs). To this end, several ASM algorithms have been developed and applied throughout this work.

Therefore, the outline of this work is as follows:

- The second chapter presents, on the one hand, the synthesis of metamaterial transmission lines based on SRRs and CSRRs in planar technology. On the other hand, Space Mapping (SM) algorithms are introduced as well as the state of the art of this technique, making a special mention to Aggressive Space Mapping (ASM).
- Chapter three is focused on Composite Right/Left Handed (CRLH) transmission lines based on the resonant approach, specifically on the design of balanced CRLH unit cells in coplanar waveguide (CPW) and microstrip technology. Moreover, the application of these unit cells to the design of microwave filters is demonstrated through several examples.
- In chapter four, the automated synthesis of CSRR-loaded transmission line unit cells through ASM is described. Two cases are considered: the negative effective permittivity unit cell, and the CRLH line. Furthermore, a novel two-step fast ASM algorithm is presented.
- Chapter five presents the potential of applying the automatic process discussed in Chapter 4 to the design of microwave devices based on CSRR-loaded transmission lines. As a proof of concept, a stop band filter and a dual-band power divider are designed by means of ASM algorithm.
- The sixth chapter proposes the application of ASM algorithms to other microwave structures. Specifically, the automated synthesis of Stepped Impedance Resonators (SIRs) and RF/microwave inductors in microstrip technology through ASM is described. Moreover, an order-3 elliptic low pass filter based on a SIR and one turn spiral inductor are designed.
- Lastly, in chapter seven, the conclusions and future research that result from this thesis are outlined.

The work conducted during the realization of this thesis was carried out within the group GEMMA (*Grup d'Enginyeria de Microones i Mil·limètriques Aplicat*)/CIMITEC (*Centre d'Investigació en Metamaterials per a la innovació en Tecnologies Electrònica i de Comunicacions*), which is part of the Electronics Engineering Department of the *Universitat Autònoma de Barcelona*. GEMMA/CIMITEC has been part of the European Network of Excellence NoE 500252-2 METAMORPHOSE (Metamaterials organized for radio, millimeter wave and photonic super lattice engineering), the main objective of which was to research, study and promote artificial electromagnetic materials and metamaterials within the European Union. It has recently given rise to the Virtual Institute for Artificial Electromagnetic Materials and Metamaterials

(METAMORPHOSE VI AISBL). Furthermore, CIMITEC is one of the centers of the Technological Innovation Network of TECNIO (ACC1Ó) of the Catalan Government, created with the objective of promoting the transference of technology to industry in the field of Information and Communication Technology and has been recognized as a Consolidated Group by the Catalan Government (AGAUR). Furthermore, this work is the result of close collaboration with the group *Grupo de Aplicaciones de Microondas* (GAM) which is part of the Institute of Telecommunications and Multimedia Applications (iTEAM) from *Universitat Politècnica de València* (UPV).

This work was supported by the Spanish and Catalan Governments by means of several projects and contracts and, specially, a research fellowship from FPU program by Spanish Government (MEC) with reference AP2008-4707. The *Universitat Autònoma de Barcelona* has contributed through the *Vicerectorat de Projectes Estratègics - Parc de Recerca*. Among the projects and contracts with the different institutions and companies that have given support to the developed research activities, we would like to highlight:

- Project TEC2007-68013-C02-02 METAINNOVA from the Spanish Government (*Dirección General de Investigación*). Project co-coordinated by the *Universitat Autònoma de Barcelona* and the *Universidad de Sevilla*. Title: *Tecnologías basadas en metamateriales y su aplicación a la innovación en componentes y subsistemas de RF microondas y milimétricas: circuitos de radiocomunicación*.

- Project CSD2008-00066 CONSOLIDER INGENIO 2010 granted to a consortium composed of eight research groups from different Spanish Universities and funded by the Spanish Government. Title: *Ingeniería de Metamateriales (EMET).*

- Project TSI-020100-2010-169 METASINTESIS granted to a consortium composed by a company, *Aurora Software and Testing S.L.*, and a research institution, *Universitat Autònoma de Barcelona*, in collaboration with *Universitat Politècnica de Valencia,* funded by Spanish Government (*Ministerio de Industria, Turismo y Comercio*) through AVANZA I+D projects. Title: *Investigación y desarrollo de una herramienta CAD para la síntesis de circuitos de comunicaciones compactos y de altas prestaciones basados en metamateriales.*

- Contract collaboration agreement between *Aurora Software and Testing S.L.*, and *Universitat Autònoma de Barcelona*, in collaboration with *Universitat Politècnica de Valencia*. Title: *Automatización del diseño de circuitos planares de microondas mediante técnicas de mapeo espacial.*

- Project TEC2010-17512 METATRANSFER granted to the *Universitat Autònoma de Barcelona* by the Spanish Government. Title: *Nuevas estrategias de diseño y síntesis de componentes de microondas basados en conceptos de METAmateriales con orientación a la TRANSFERrencia tecnológica.*

# 2

# Introduction and state of the art



This chapter is focused on two hot topics. On one hand, the synthesis of metamaterial transmission lines in planar technology [1-3] is introduced, with special attention on the resonant-type approach [4-6], where the constitutive particles are sub-wavelength resonators such as Split Ring Resonators (SRRs). Metamaterial transmission lines have a very interesting design flexibility that makes them suitable for microwave device implementation. Consequently, these lines have been used for several applications, such as broadband [7-12] and multiband [13-18] components, leaky wave antennas [19-22], novel broadband filters and diplexers with spurious suppression [23-25], among others. On the other hand, Space Mapping (SM) algorithms [26], which have been widely used in the design of microwave devices [27], are also presented. The main advantage provided by these algorithms is the combination of high speed of circuit simulators and the accuracy of electromagnetic (EM) solvers. In particular, an improvement of this technique named Aggressive Space Mapping (ASM) [28] is explained with more detail.

# 2.1 Metamaterial transmission lines

Metamaterial transmission lines consist on a host line periodically-loaded with reactive elements, and exhibiting controllable electromagnetic properties. It is possible to make an analogy between the propagation in a transmission line and the propagation of plane waves in a homogeneous and isotropic medium. In this way, we can identify its effective constitutive parameters, that is the effective permittivity ($\varepsilon_{eff}$) and permeability ($\mu_{eff}$), through the following expressions:

$$Z_s'(\omega) = j\omega\mu_{eff} \tag{2.1}$$

$$Y_p'(\omega) = j\omega\varepsilon_{eff} \tag{2.2}$$

where $Z'_s$ and $Y'_p$ are the per unit length series impedance and shunt admittance, respectively, of the equivalent T- or π-circuit model of the unit cell of the structure. This gives rise to four possibilities, regarding the signs of $Z'_s$ and $Y'_p$. If the constitutive parameters are both positive, the transmission media exhibits forward (or right handed) wave propagation but if these parameters are both negative, backward (or left handed) wave propagation occurs. Otherwise if these have opposite sign, propagation is inhibited leading to evanescent modes.

In transmission line theory, the important parameters are the electrical length (or phase constant) and the characteristic impedance. From the theory of periodic structures the dispersion relation can be inferred [29]:

$$\cosh \gamma l = \frac{A+D}{2} \tag{2.3}$$

where $\gamma = \alpha + j\beta$ is the complex propagation constant ($\alpha$ and $\beta$ being the attenuation constant and the phase constant, respectively), $l$ is the unit cell length, $A$ and $D$ are the diagonal elements of the ABCD matrix of the unit cell. In non-attenuating and propagating wave case ($\alpha=0$, $\beta\neq0$), the expression (2.3) can be rewritten as:

$$\cos \beta l = \frac{A+D}{2} \tag{2.4}$$

Moreover, we can define the characteristic impedance (also referred as the Bloch impedance) of the unit cell as

$$Z_B \pm = \frac{-2B}{A-D \mp \sqrt{(A+D)^2-4}} \tag{2.5}$$

If we now consider a symmetrical unit cell and its T- or π-circuit model, we can express equation (2.4) as:

$$\cos \beta l = 1 + \frac{Z_s(\omega)}{Z_p(\omega)} \tag{2.6}$$

where $Z_s$ and $Z_p$ are the series and shunt impedances, respectively, of the equivalent T- or π-circuit model (see Figure 2.1).

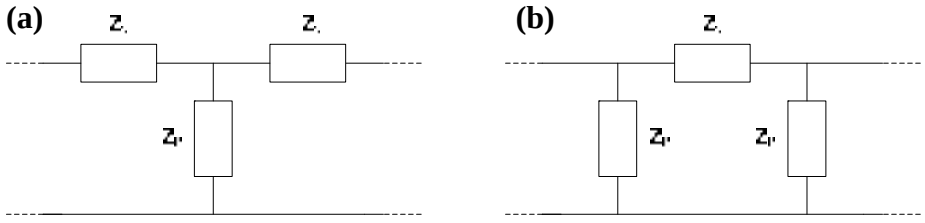


**Figure 2.1.** Generic T (a) and π (b) circuit model

The characteristic impedance for the T-circuit model can be written as:

$$Z_{B_T}(\omega) = \sqrt{Z_s(\omega)[Z_s(\omega) + 2Z_p(\omega)]} \tag{2.7}$$

and, if the structure is modeled by a π-circuit, expression (2.5) is written as follows:

$$Z_{B_\pi}(\omega) = \sqrt{\frac{Z_s(\omega)Z_p(\omega)/2}{1 + \dfrac{Z_s(\omega)}{2Z_p(\omega)}}} \tag{2.8}$$

## 2.1.1 Transmission line theory of effective media

Let us consider a periodic network formed by a cascade of series capacitances and shunt inductances that is the dual version of the equivalent circuit model of a conventional planar transmission line without losses (see Figure 2.2). In contrast to conventional line, the dual (or left handed) transmission line exhibits backward wave propagation. Although this network does not describe any natural propagating structure, it can be analyzed from the theory of periodic structures (or Bloch mode theory) [29]. If we consider the T-circuit shown in Figure 2.2(c), we can obtain the dispersion relation from (2.6) by introducing its corresponding impedances:

$$\cos(\beta_L l) = 1 - \frac{1}{2LC\omega^2} \tag{2.9}$$

and using (2.7) the characteristic impedance can be written as follows:

$$Z_{BL} = \sqrt{\frac{L}{C}\left(1 - \frac{\omega_{cL}^2}{\omega^2}\right)} \tag{2.10}$$

where $\omega_{cL}=1/2(LC)^{1/2}$ is an angular cut-off frequency. Notice that the sub-index L denotes that the structure exhibits left-handed wave propagation, as can be seen in the dispersion diagram depicted in Figure 2.3(b), where in the portion of the diagram where the phase constant is negative the group velocity is positive. The characteristic impedance dependence with frequency is depicted in Figure 2.3(d) where it can be observed that at low frequencies the impedance is zero and at high frequencies it tends to the maximum value, that is, the impedance of a conventional transmission line.

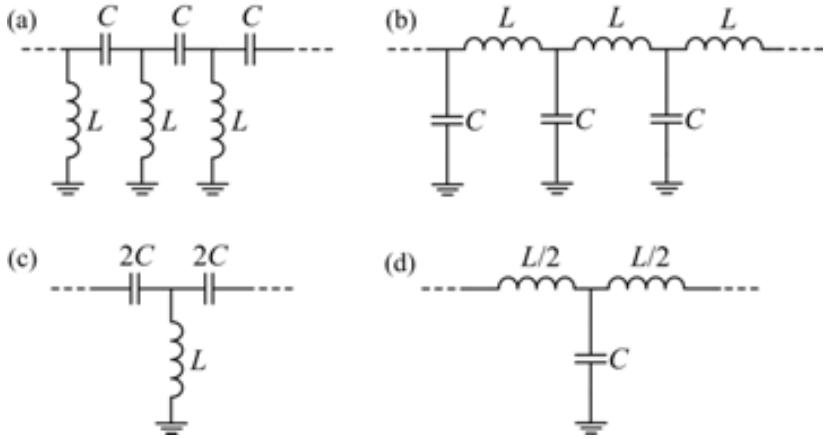


**Figure 2.2.** Equivalent circuit model of a backward (a) and a forward (b) transmission lines. The T-circuit models of the basic cell structures are also indicated in (c) and (d). Figure extracted from. [30].

On the other hand, if we consider the network depicted in Figure 2.2(b), that is the model of an ideal lossless conventional planar transmission line, an identical analysis can be done by means of its T-circuit model [Figure 2.2(d)] and the following expressions can be inferred:

$$\cos\beta_R l = 1 - \frac{LC}{2}\omega^2 \tag{2.11}$$

$$Z_{BR} = \sqrt{\frac{L}{C}\left(1 - \frac{\omega^2}{\omega_{cR}^2}\right)} \tag{2.12}$$

where $\omega_{cR}=2/(LC)^{1/2}$ is an angular cut-off frequency and the subindex R refers to right-handed (i.e., forward) wave propagation of the structure. The dispersion relation as well as the dependence of the characteristic impedance on frequency are depicted in Figure 2.3(a) and (c) respectively. This circuit is only valid in the long wavelength limit i.e., for frequencies well below the cut-off frequency ($\omega << \omega_{cR}$ or where wavelength satisfies $\lambda >> l$). In order to correctly model an ideal lossless transmission line at higher frequencies, we need to reduce the period of the structure, and, consequently, the per-

section inductance and capacitance of the line with the result of a higher cut-off frequency. In this way, an ideal transmission line without dispersion can be described by the circuit of Figure 2.2(b). Under the long wave limit approximation we can rewrite equations (2.11) and (2.12) as follows:

$$\beta_R = \omega\sqrt{L'C'} \tag{2.13}$$

$$Z_{BR} = \sqrt{\frac{L'}{C'}} \tag{2.14}$$

where $L'$ and $C'$ are the per unit-length inductance and capacitance of the transmission line. These equations [(2.13) and (2.14)] are well-known expressions of the conventional transmission lines. Furthermore, we can obtain the phase and group velocities of these conventional (or forward) transmission lines from (2.13):

$$v_{pR} = \frac{\omega}{\beta_R} = \frac{1}{\sqrt{L'C'}} = \frac{l}{\sqrt{LC}} \tag{2.15}$$

$$v_{gR} = \left(\frac{\partial\beta_R}{\partial\omega}\right)^{-1} = \left(\sqrt{L'C'}\right)^{-1} = v_{pR} \tag{2.16}$$

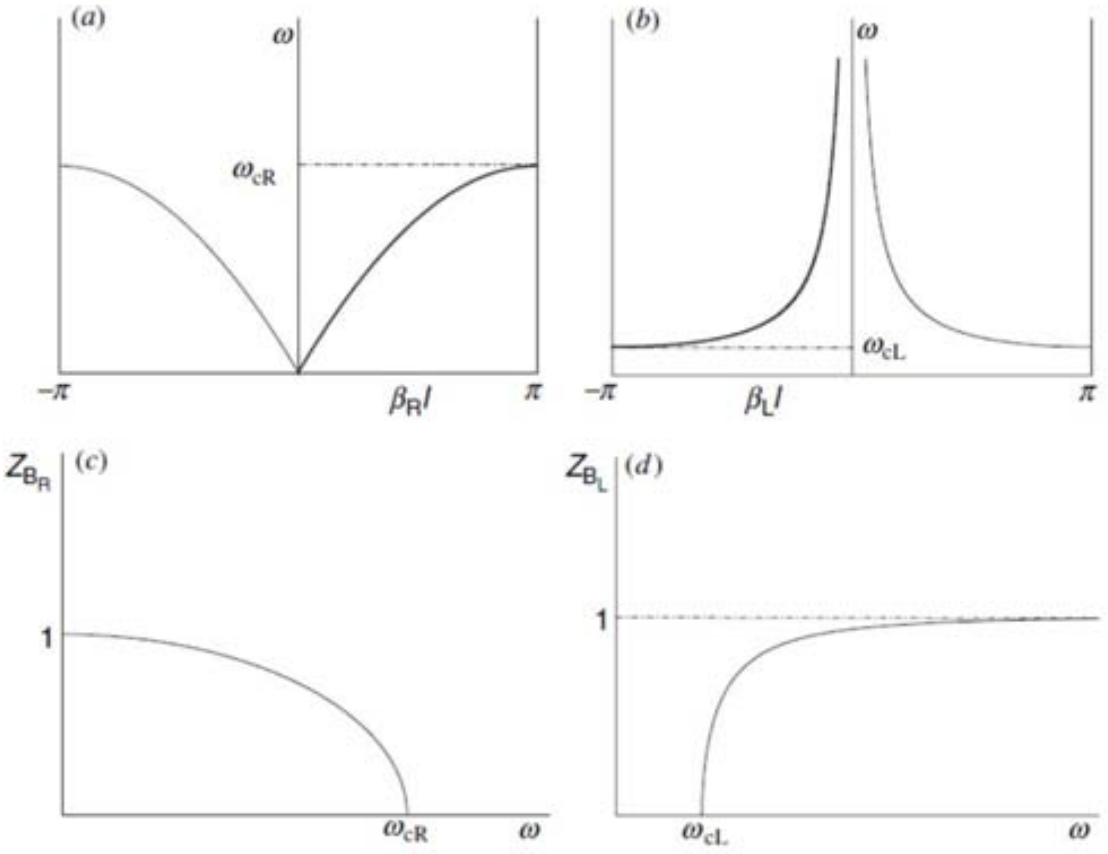


**Figure 2.3.** Typical dispersion diagram of a forward (a) and backward (b) transmission line model. The dependence of the normalized ($Z_B/Z_{lw}$) Bloch impedance with frequency is shown in (c) and (d) for the

forward and backward lines, respectively. $Z_{lw}$ is the maximum value of the impedance. Extracted from [30].

On the contrary, the backward transmission line is dispersive even in the long wavelength limit. However, it only can be considered as an effective propagating medium under this approximation. Nevertheless, the structure depicted in Figure 2.2(b) supports backward waves; hence it is a left-handed transmission line. In many circuit applications, the operation under long wave limit approximation is not a due because these applications are based on their left-handedness instead of their effective medium properties. However, for coherence, to infer the following expression concerning the phase constant, the characteristic impedance, as well as the phase and group velocities the aforementioned approximation is applied. On one hand, to obtain the phase shift, a second order Taylor polynomial is applied:

$$\cos(\beta_L l) \approx 1 - \frac{(\beta_L l)^2}{2} \tag{2.17}$$

and equation (2.9) could be expressed as follows:

$$\beta_L l = -\frac{1}{\omega\sqrt{LC}} \tag{2.18}$$

On the other hand, considering that $\omega >> \omega_{cL}$, the characteristic impedance is given by:

$$Z_{BL} = \sqrt{\frac{L}{C}} \tag{2.19}$$

The phase and group velocities are obtained as follows:

$$v_{pL} = \frac{\omega}{\beta_L} = -\omega^2 l\sqrt{LC} \tag{2.20}$$

$$v_{gL} = \left(\frac{\partial\beta_L}{\partial\omega}\right)^{-1} = \left(\frac{-1}{\omega^2}\frac{-1}{l\sqrt{LC}}\right)^{-1} = +\omega^2 l\sqrt{LC} = -v_{pL} \tag{2.21}$$

and these velocities have opposite signs.

For the forward line, the effective permittivity and permeability are given by:

$$\varepsilon_{eff} = C / l \tag{2.22}$$

$$\mu_{eff} = L / l \tag{2.23}$$

Whereas for the backward transmission line, the constitutive parameters are:

$$\varepsilon_{eff} = -\frac{1}{\omega^2 Ll} \tag{2.24}$$

$$\mu_{eff} = -\frac{1}{\omega^2 C l} \tag{2.25}$$

Thereby, these lines behave as an effective media with negative permittivity and permeability, and consequently exhibiting left-handed wave propagation.

## 2.1.2 Composite Right-/Left Handed (CRLH) transmission lines

In the previous section, the backward transmission line was presented. From a theoretical point of view, it is possible to achieve left-handed wave propagation with a structure composed by means of series capacitors and shunt inductors, but in practice to implement these lines a host line is needed, regardless the technology used (microstrip, coplanar waveguide, stripline, etc). The incorporation of this host line introduces thus parasitic elements that should be taken into account to describe accurately the propagation characteristics of the lines. These structures exhibit left-handed or right-handed wave propagation depending on the working frequency range, therefore, they have been named as CRLH transmission lines [1]. In Figure 2.4 the equivalent circuit model of these structures is shown. Notice that the reactive elements have been renamed with respect to the previous section as $C_L$ and $L_L$ concerning backward transmission line as well as $C_R$ and $L_R$ for the host line elements, where the subindex $L$ and $R$ indicates left and right handedness respectively. By using the dispersion relation (2.6) and the characteristic impedance equation (2.7), we obtain for the CRLH transmission line case:

$$\cos \beta l = 1 - \frac{\omega^2}{2\omega_R^2}\left(1 - \frac{\omega_s^2}{\omega^2}\right)\left(1 - \frac{\omega_p^2}{\omega^2}\right) \tag{2.26}$$

$$Z_B = \sqrt{\frac{L_R}{C_R}\frac{\left(1 - \frac{\omega_s^2}{\omega^2}\right)}{\left(1 - \frac{\omega_p^2}{\omega^2}\right)} - \frac{L_R^2 \omega^2}{4}\left(1 - \frac{\omega_s^2}{\omega^2}\right)^2} \tag{2.27}$$

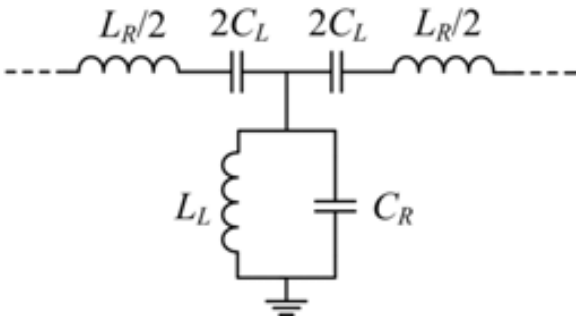


**Figure 2.4.** Equivalent circuit model of the CRLH transmission line. Figure extracted from. [30].

where in order to simplify the mathematical formulas the following variables

$$\omega_R = \frac{1}{\sqrt{L_R C_R}} \tag{2.28}$$

$$\omega_L = \frac{1}{\sqrt{L_L C_L}} \tag{2.29}$$

and the series and shunt resonance frequencies

$$\omega_R = \frac{1}{\sqrt{L_R C_R}} \tag{2.30}$$

$$\omega_L = \frac{1}{\sqrt{L_L C_L}} \tag{2.31}$$

have been introduced. The typical dispersion diagram and characteristic impedance of the structure can be seen in Figure 2.5 (equations (2.26) and (2.27), respectively). It can be observed that the parameters $C_L$ and $L_L$, corresponding to the backward transmission line, are dominant in the low frequency region, thus, backward wave propagation is allowed. By contrast, above the frequency band gap, the situation is reversed since the domain of the parasitic elements of the host line ($C_R$ and $L_R$) leads to a right-handed behavior. Hence, we have a structure for low frequencies that behaves like a left-handed line and at high frequencies as a conventional line, where the two bands are separated by a frequency gap limited by those frequencies satisfying:

$$\omega_{G1} = \min(\omega_s, \omega_p) \tag{2.32}$$

$$\omega_{G2} = \max(\omega_s, \omega_p) \tag{2.33}$$

Concerning the phase constant of this structure, in the long wavelength limit approximation, the expression (2.26) is rewritten as:

$$\beta = \frac{s(\omega)}{l}\sqrt{\frac{\omega^2}{\omega_R^2}\left(1-\frac{\omega_s^2}{\omega^2}\right)\left(1-\frac{\omega_p^2}{\omega^2}\right)} \tag{2.34}$$

where $s(\omega)$ is the following sign function:

$$s(\omega) = \begin{cases} -1 & \text{if} \quad \omega < \min(\omega_s, \omega_p) \\ +1 & \text{if} \quad \omega > \max(\omega_s, \omega_p) \end{cases} \tag{2.35}$$

From the phase constant (2.34), the phase and group velocities can be easily inferred, these velocities being of opposite sign in the left-handed band and both being positive in the right-handed band.

For the CRLH transmission line case, the constitutive parameters can be inferred from Figure 2.4 by using the expressions (2.1) and (2.2):

$$\varepsilon_{eff} = \frac{C_R}{l} - \frac{1}{\omega^2 L_L l} \tag{2.36}$$

$$\mu_{eff} = \frac{L_R}{l} - \frac{1}{\omega^2 C_L l} \tag{2.37}$$

and depending on the frequency range, they can be positive or negative. Notice that at low frequencies these expressions tend to equations (2.24) and (2.25), that is, left-handed behavior. In contrast, at high frequencies the expressions of the constitutive parameters look like equations (2.22) and (2.23), as in the case of a conventional line.

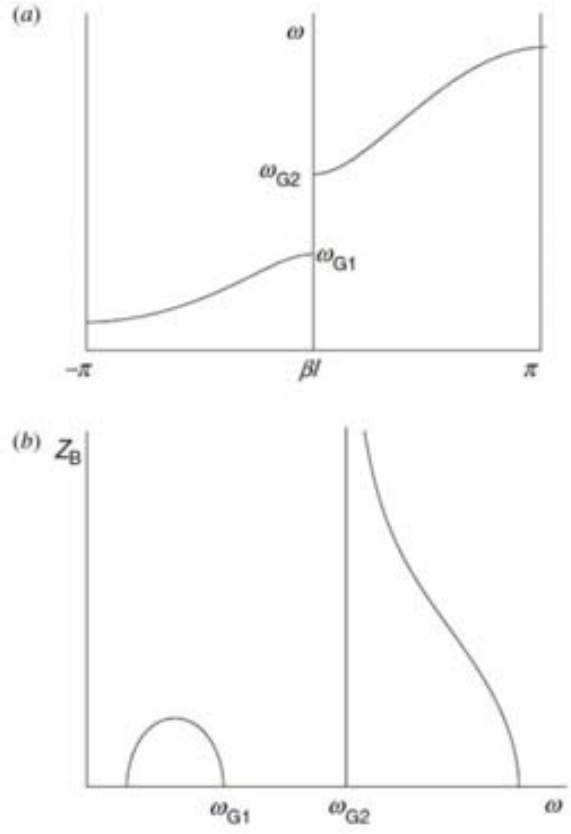


**Figure 2.5.** Typical dispersion diagram (a) and variation of Bloch impedance (real part) with frequency (b) in a CRLH transmission line model (in this example, $\omega_s<\omega_p$). Figure extracted from. [30].

A particular case of interest is the CRLH balanced line. In this case, there is not a frequency gap between the two bands because the series and shunt resonances are forced to be identical, namely $\omega_s=\omega_p=\omega_0$ [1, 31]. As a result, a single transmission band with left- and right-handed characteristics at different frequencies is obtained. As can be observed in Figure 2.6 the characteristic impedance reaches its maximum at the transition frequency, $\omega_0$, where:

$$Z_B = \sqrt{\frac{L_R}{C_R}} = \sqrt{\frac{L_L}{C_L}} \tag{2.38}$$

and decreases as frequency increases or decreases from $\omega_0$. Notice that in the vicinity of the transition frequency, $Z_B$ is not very dependent on frequency. This fact is interesting for broadband matching. Furthermore, at this frequency the phase velocity exhibits a pole, the phase constant is zero, whereas the group velocity if finite, contrary to the unbalanced case, in which at resonance frequencies ($\omega_s$, $\omega_p$) the group velocity is zero. Thus, in balanced CRLH transmission lines there is energy transmission at the transition frequency.

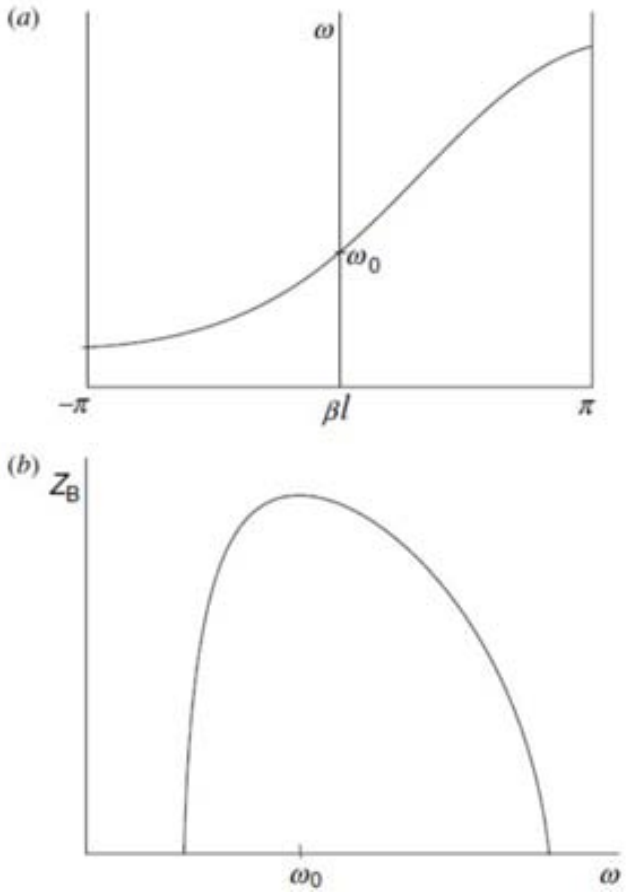


**Figure 2.6.** Typical dispersion diagram (a) and variation of Bloch impedance with frequency (b) in a balanced CRLH transmission line. Figure extracted from. [30].

## 2.1.3 Resonant approach

Soon after the appearance of the first CRLH transmission line implemented by loading a host line with series capacitances and shunt inductances, that is, based on the CL-loaded transmission line approach (Caloz *et al.* [32]) several authors presented another transmission lines, based on sub-wavelength resonators, exhibiting CRLH properties. This approach is called resonant-type approach and in this work we will focus on the

use of the Split Ring Resonator (SRR) [33] and its complementary counterpart, the Complementary Split Ring Resonator (CSRR) [34], to obtain a left-handed or a CRLH behavior.

### 2.1.3.1 CRLH lines loaded with SRRs

The first resonant-type metamaterial transmission line was reported by Martin *et al.* [4] consisting of a coplanar waveguide (CPW) loaded with SRRs and shunt-connected metallic strips. The SRR is formed by two concentric open metallic rings with slits etched in opposite sides. This resonator, presented by Pendry *et al.* [33], can be excited by an axial (directed along *z*-axis) time-varying external magnetic field and due to its small electrical size can be analyzed by using the quasi-static condition, resulting in a parallel *LC* tank as its equivalent circuit model [35] . In Figure 2.7, the topology as well as equivalent circuit model of a SRR is shown. $C_0$ corresponds to the distributed capacitance between rings ($C_0=2\pi r_0 C_{pul}$), where $C_{pul}$ is the per unit-length edge capacitance. The inductance, $L_s$, can be approximated as the inductance of a single ring of average radius $r_0$ and width $c$. The resonance frequency of the SRR is given by following expression:

$$\omega_0 = \frac{1}{\sqrt{L_s C_s}} \tag{2.39}$$

At this frequency, the perimeter of the resonator is smaller than half the wavelength of the exciting wave. Thus, the electrical size of the resonator along *x* and *y* axis can be significantly smaller than $\lambda/2\pi$. Furthermore, an array of these particle exhibits effective negative permeability at certain frequency region. Exploiting this property, the first left-handed medium was synthesized by Smith *et al.* [36] combining an array of SRRs to introduce the negative permeability with metallic posts to introduce negative permittivity. However, the first left-handed transmission line based on SRRs in planar technology was reported by Martin *et al.* [4]. Indeed, the structure exhibits a CRLH behavior, although the work was focused on demonstrating its backward wave propagation.


**Figure 2.7.** Topology and equivalent circuit of a SRR. Figure extracted from [35].

In Figure 2.8, a typical layout of a unit cell of this kind of lines is depicted. The equivalent circuit model is depicted in Figure 2.9(a), where the SRRs are modeled as parallel *LC* tanks coupled to the host line, by a mutual inductance *M*/2. This equivalent circuit model can be transformed to the one shown in Figure 2.9(b) by means of the following expressions [37]:

$$L_s' = 2M^2 C_s \omega_o^2 \frac{\left(1+\frac{L}{4L_p}\right)^2}{1+\frac{M^2}{2L_pL_s}} \tag{2.40}$$

$$C_s' = \frac{L_s}{2M^2\omega_o^2}\left(\frac{1+\frac{M^2}{2L_pL_s}}{1+\frac{L}{4L_p}}\right)^2 \tag{2.41}$$

$$L' = \left(2+\frac{L}{2L_p}\right)\frac{L}{2} - L_s' \tag{2.42}$$

$$L_p' = 2L_p + \frac{L}{2} \tag{2.43}$$

where $\omega_0^2 = 1/L_sC_s$ is the resonance frequency of the parallel *LC* tank in Figure 2.9(a), that is, the resonance of the SRR. Notice that there is a transmission zero to the left of the left-handed band not given by SRR resonance but by the resonance of *LC* tank formed by $L_s'$ and $C_s'$ that, according to the transformation equations, is given by:

$$\omega_z = \frac{1}{\sqrt{L_sC_s\left(1+\frac{M^2}{2L_pL_s}\right)}} \tag{2.44}$$

and depends on $L_p$, that is, the shunt inductors connected to the ground.

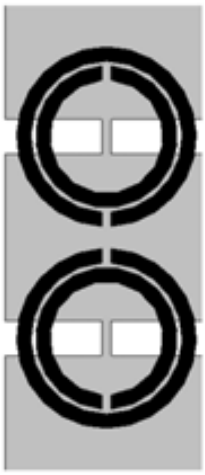

**Figure 2.8.** Typical layout of a CRLH SRR-based unit cell in CPW technology. The SRRs are etched in the back substrate side and the CPW is loaded with shunt inductances. Figure extracted from [37].

Thus, the series and shunt impedances of the equivalent π-circuit model depicted in Figure 2.9(b) can be expressed as follows:

$$Z_s = j\omega L^{'} + j\omega \frac{L_s^{'}}{1-\omega^2 L_s^{'} C_s^{'}} = j\left(\frac{\omega\left[\left(L^{'}+L_s^{'}\right)-\omega^2 L_s^{'} C_s^{'} L^{'}\right]}{\left(1-\omega^2 L_s^{'} C_s^{'}\right)}\right) \tag{2.45}$$

$$Z_p = j\omega \frac{L_p^{'}}{1-\omega^2 L_p^{'} \frac{C}{2}} = j\left(\frac{L_p^{'}\omega}{1-\omega^2 L_p^{'} \frac{C}{2}}\right) \tag{2.46}$$

Furthermore, according to (2.8) the characteristic impedance for its model is given by:

$$Z_B = \left(\frac{-\omega^3 {L_p^{'}}^2 \left(L^{'}+L_s^{'}\right)\left(1-\frac{\omega^2}{{\omega_s}^2}\right)}{\left(1-\frac{\omega^2}{{\omega_p}^2}\right)^2\left(1-\frac{\omega^2}{{\omega_z}^2}\right)\left(\frac{\omega\left(L^{'}+L_s^{'}\right)\left(1-\frac{\omega^2}{{\omega_s}^2}\right)}{\left(1-\frac{\omega^2}{{\omega_z}^2}\right)}+\frac{2\omega L_p^{'}}{\left(1-\frac{\omega^2}{{\omega_p}^2}\right)}\right)}\right)^{\frac{1}{2}} \tag{2.47}$$

where, ${\omega_s}^2 = \left(L^{'}+L_s^{'}\right)\Big/\left(C_s^{'} L_s^{'} L^{'}\right)$ and ${\omega_p}^2 = 2\Big/L_p^{'} C$ . This expression, as well as, the shunt and series reactance of the equivalent circuit model is depicted in Figure 2.10(a), (b) and it can be seen that at the upper limit of the left-handed band, the impedance tends to zero if the series resonance is smaller than the shunt one (i.e. $\omega_s<\omega_p$) and

otherwise tends to infinity. In the same way, at the lower limit of the right-handed band, the impedance tends to infinity if it is the first case and to zero if it is the second one (i.e. $\omega_p<\omega_s$). However, if the resonances are identical, that is the balanced case, the characteristic impedance exhibits a continuous variation in the vicinity of the transition frequency. This particular case, as well as its design procedure, will be discussed in more detail in section 3.2.

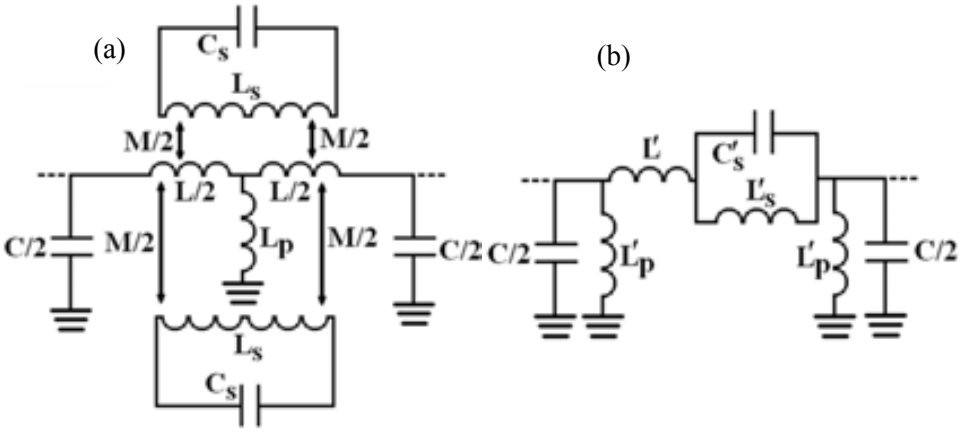


**Figure 2.9.** Circuit model for the basic cell of the CRLH SRR-based CPW structure (a). Transformation of the model to a π–circuit (b). Figure extracted from [37].

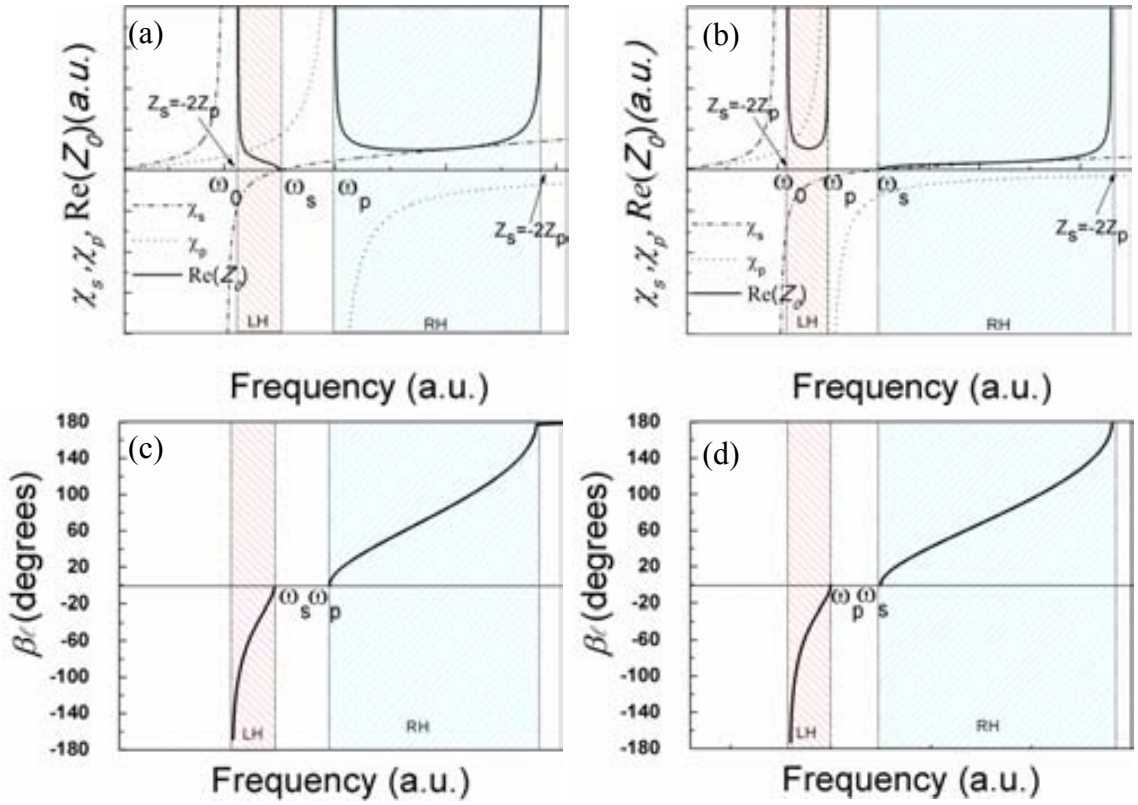


**Figure 2.10.** Series, shunt reactances, characteristic impedance and dispersion diagram for the model depicted in Figure 2.9(b). Two cases are represented: (a) and (c) for the case where $\omega_s<\omega_p$ and (b) and (d) for the case where $\omega_s>\omega_p$.

### 2.1.3.2 CRLH lines loaded with CSRRs

In the same way as in the previous section, it is possible to implement CRLH lines by means of CSRRs which are the dual or complementary particle of the SRR. The typical topology and its equivalent circuit model are depicted in Figure 2.11.

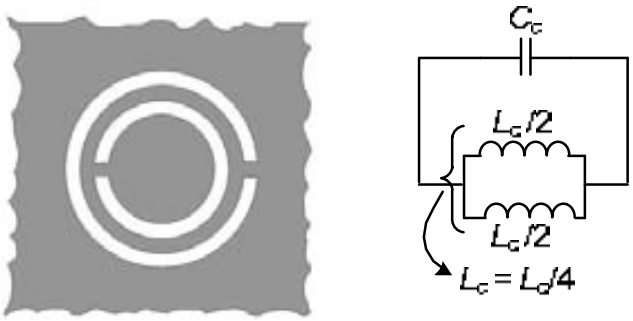


**Figure 2.11.** Typical topology and equivalent circuit model of a CSRR. The metallic zones are depicted in gray. Figure extracted from [35].

The CSRR is obtained by replacing the metal parts of the original structure (SRR) with apertures, and the apertures with metal plates. Considering the Babinet principle, it can be demonstrated that, if the effects of the metal thickness and losses as well as those of the dielectric substrate are neglected a perfect dual behavior is expected, that is, given the same dimensions, the CSRR resonates at the same frequency as the SRR. To this end, an excitation by an axial electric field is needed.

Thus, resonant-type metamaterials can be implemented by means of microstrip lines loaded with CSRRs and series gaps. In this way, the first left-handed line based on CSRRs was presented by Baena *et al.* [35]. Although, that work was centered in the demonstration of the left-handed behavior of this kind of lines, it was, indeed, the first CRLH line loaded with CSRRs. The Typical topology of the unit cell of this kind of lines is shown in Figure 2.12, as well as, its equivalent circuit model and the transformed T-model, where the CSRR is etched in the ground plane to be excited by the axial electric field present in the host microstrip line. According to the model of Figure 2.12(b) the CSRR is modeled as a shunt parallel *LC* tank by means of $L_c$ and $C_c$ parameters, it is electrically coupled to the host line that is modeled by inductance $L/2$ and shunt capacitance $C_L$. Moreover, the series gap in the host line is modeled by a π-model that is composed by a series capacitance $C_s$ and two fringing capacitances $C_f$. However, in order to simplify the analysis, the equivalent circuit model of Figure 2.12(b) can by transformed to the one depicted in Figure 2.12(c). To this end, the following conditions are considered [38]:

$$2C_g = 2C_s + C_{par} \tag{2.48}$$

$$C = \frac{C_{par}(2C_s + C_{par})}{C_s} \tag{2.49}$$

where $C_{par} = C_f + C_L$. As in the case of CRLH loaded with SRRs, the structure behaves as a conventional CRLH with an additional transmission zero, in this case due to the resonance of the shunt branch (i.e. due to the presence of an extra capacitance $C$)

Thereby, analyzing the equivalent T-circuit model depicted in Figure 2.12(c), its series and shunt impedances can be expressed as follows:

$$Z_s = \frac{j}{2}\left( L\omega - \frac{1}{C_g\omega} \right) = j\left( \frac{LC_g\omega^2 - 1}{2C_g\omega} \right) \tag{2.50}$$

$$Z_p = j\left( \frac{L_c\omega}{1 - L_cC_c\omega^2} - \frac{1}{C\omega} \right) = j\left( \frac{L_c\left(C_c + C\right)\omega^2 - 1}{\left(1 - L_cC_c\omega^2\right)C\omega} \right) \tag{2.51}$$

and according to the Bloch impedance expression for a T-circuit model (2.7), the characteristic impedance of these kind of lines can be written as:

$$Z_B = \sqrt{\frac{L}{C}\left(1 - \frac{\omega_s^{\,2}}{\omega^2}\right) + \frac{L}{C_c}\frac{\left(1 - \frac{\omega_s^{\,2}}{\omega^2}\right)}{\left(1 - \frac{\omega_p^{\,2}}{\omega^2}\right)} - \frac{L^2\omega^2}{4}\left(1 - \frac{\omega_s^{\,2}}{\omega^2}\right)^2} \tag{2.52}$$

where, $\omega_s^{\,2} = 1/LC_g$ and $\omega_p^{\,2} = 1/L_cC_g$, corresponding to series and shunt resonance, frequency, respectively. And the transmission zero frequency that corresponds to the resonance of the shunt branch is:

$$\omega_z = \frac{1}{\sqrt{L_c(C_c + C)}} \tag{2.53}$$

It is worth to mention that, in this case, the characteristic impedance tends to zero at the beginning of left-handed band and at the end of the right-handed band, in contrast to the previous case (CRLH loaded with SRRs). Similarly, we have to take in account two different cases, if $\omega_s < \omega_p$ the characteristic impedance at the upper limit of the left-handed band tends to zero and at the lower limit of the right-handed band tends to infinity. Conversely, if the shunt resonance is smaller than the series resonance (i.e. $\omega_s > \omega_p$), the characteristic impedance tends to infinity and zero at the end of the left-handed band and at the beginning of the right-handed band, respectively. The dependence with frequency of the aforementioned impedance, as well as that of the series and shunt reactance, are depicted in Figure 2.13(a), (b) for each case. Moreover, the dispersion diagram is shown in Figure 2.13(c), (d). The balance case will be discussed in more detail together with its design in section 3.1.

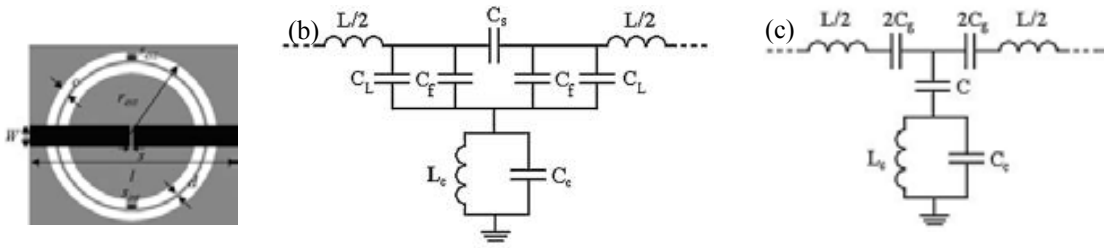


**Figure 2.12.** Typical topology of a CRLH line unit cell based on the combination of CSRRs and series gaps (a), and lumped element equivalent circuit model (b). The CSRRs are etched in the ground plane, depicted in grey. The transformed T-model is depicted in (c).

Furthermore, the automatic synthesis of these CSRR-based lines will be considered using optimization algorithms, as can be seen in section 4.2.

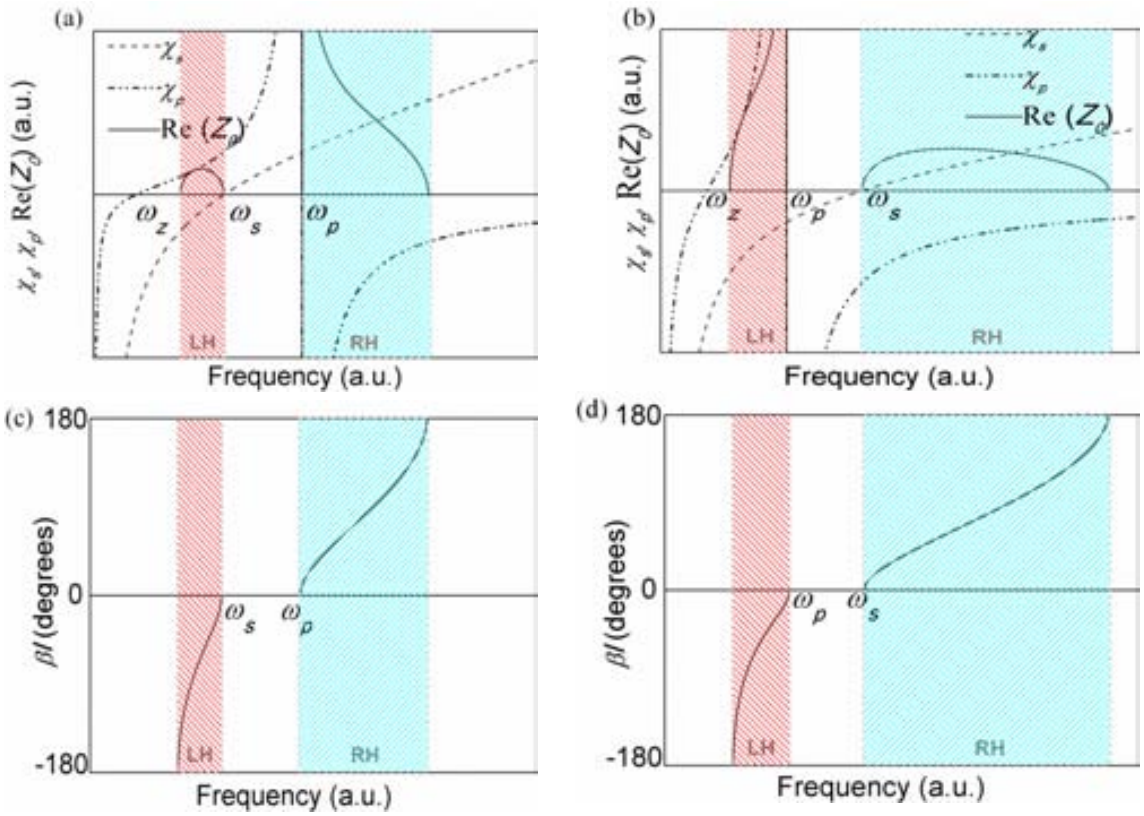


**Figure 2.13.** Series, shunt reactances, characteristic impedance and dispersion diagram for the model depicted in Figure 2.12. Two cases are represented: (a) and (c) for the case where $\omega_s<\omega_p$ and (b) and (d) for the case where $\omega_s>\omega_p$.

## 2.2 Space Mapping Algorithms

For a long time, in engineering, optimization techniques and computer aided design (CAD) have been used in order to determine a set of physical parameters to satisfy certain specifications. Specifically, in microwave engineering, during the 1980s,

electromagnetic (EM) simulators have been developed by several companies like *Ansoft Corp.*, *Hewlett-Packard EEsof* (now *Agilent Technologies*) or *Sonnet Software*. These simulators can be able to solve Maxwell's equations for complex geometries and nowadays are used to obtain accurate simulations or for validity. However, the determination of an optimal solution depends on engineers experience and a properly knowledge of each structure. One attracting idea for microwave engineers was to employ EM solvers for direct optimization but such solvers are CPU intensive and they also have non-differentiable response evaluation and non-parameterized design variables. In order to ease this, in 1990, through Optimization Systems Associates (OSA), Bandler introduced OSA90 [39], the world's first friendly microwave optimization engine for performance-driven and yield-driven design. It provided an interface to external simulators based either on circuit or EM simulations. In Swanson's words, "OSA90 is the first commercially successful optimization scheme which included a field-solver inside the optimization loop" [40-42]. Due to the success of this optimization engine the company *Hewlett-Packard EEsof* purchased OSA.

Nevertheless, the successful interconnection of EM solvers with powerful optimization techniques only partially solved the EM-based design bottleneck, since EM simulation remained CPU-intensive. Thus, conventional mathematical optimization algorithms insufficiently satisfied the microwave community's ambitions for automated EM-based design optimization.

To this end, Bandler *et al.* [26] proposed an effective idea in order to join the efficiency of circuit optimization with the accuracy of EM solvers. The idea was called Space Mapping (SM) technique and it consisted on mapping the optimized circuit models to the corresponding EM models. This technique uses a coarse model which is fast but inaccurate and a fine model that is EM based, more accurate than the coarse model, but more expensive in terms of computation. In microwave engineering, the fine model is usually linked to EM simulation and the coarse model can be described by an analytical model, a circuit model or a physically based model with less accuracy than EM simulation.

In the next subsection, the concept of SM as well as the implementation of SM algorithm will be discussed in detail.

## 2.2.1 Introduction to Space mapping algorithms

Let us, consider an optimization problem for a given set of design specifications and two simulation spaces. On one hand, we have the $\mathbf{X}_c$ space linked to a coarse model, which is simple and efficient, although not accurate. In this space, the vector containing model parameters is denoted by $\mathbf{x}_c$. On the other hand, we have the $\mathbf{X}_f$ space concerning the fine model, which is more accurate but CPU-intensive and more complex, and its corresponding vector $\mathbf{x}_f$. As depicted in Figure 2.14, the corresponding responses are

denoted by $\mathbf{R}_c$ and $\mathbf{R}_f$ for the coarse and fine models, respectively. The main idea is to find a mapping $\mathbf{P}$ to generate an appropriate parameter transformation

$$\mathbf{x}_c = \mathbf{P}(\mathbf{x}_f) \tag{2.54}$$

such that

$$\mathbf{R}_c(\mathbf{P}(\mathbf{x}_f)) \approx \mathbf{R}_f(\mathbf{x}_f) \tag{2.55}$$

in some predefined region.

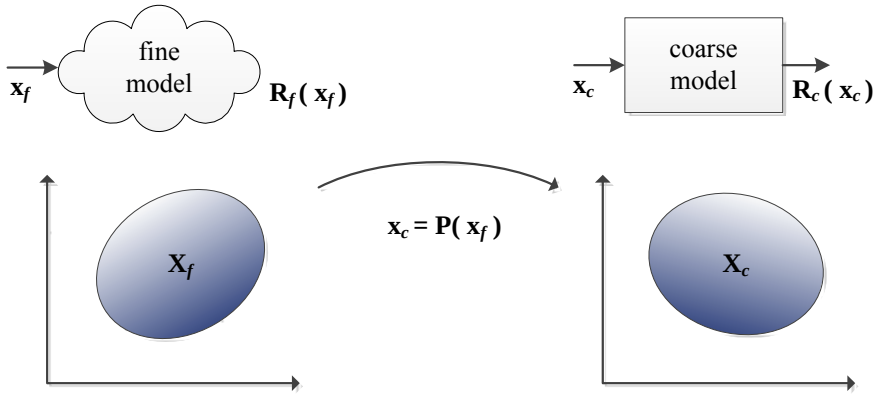


**Figure 2.14.** Illustration of SM

We can find the fine model solution, which is the image of $\mathbf{x}_c^*$, the coarse model optimal solution by the following relation:

$$\mathbf{x}_f^{(j)} = \mathbf{P}^{-1}(\mathbf{x}_c^*) \tag{2.56}$$

where the key aspect is to find an appropriate determination of $\mathbf{P}$ following the iterative process described below.

First of all, we need a set of $m_0$ base points, it is suggested to take $\mathbf{x}_f^{(1)} = \mathbf{x}_c^*$, thus, the first point is taken as the optimal coarse solution. The rest $m_0 - 1$ points are selected by perturbation with $m_0 \geq n + 1$. Then, the response for every point in the fine model is simulated and a corresponding set of points of the coarse model are obtained through the Single-Point Extraction (SPE) process, that is, these points satisfying the following expression.

$$\mathbf{x}_c^{(i)} = \arg\left\{\min_{\mathbf{x}_c} \left\|\mathbf{R}_f(\mathbf{x}_f^{(i)}) - \mathbf{R}_c(\mathbf{x}_c)\right\|\right\} \tag{2.57}$$

In these conditions, we are able to find the first mapping approximation $\mathbf{P}^{(0)}$ as a linear mapping, as was assumed by Bandler *et al.* [26].

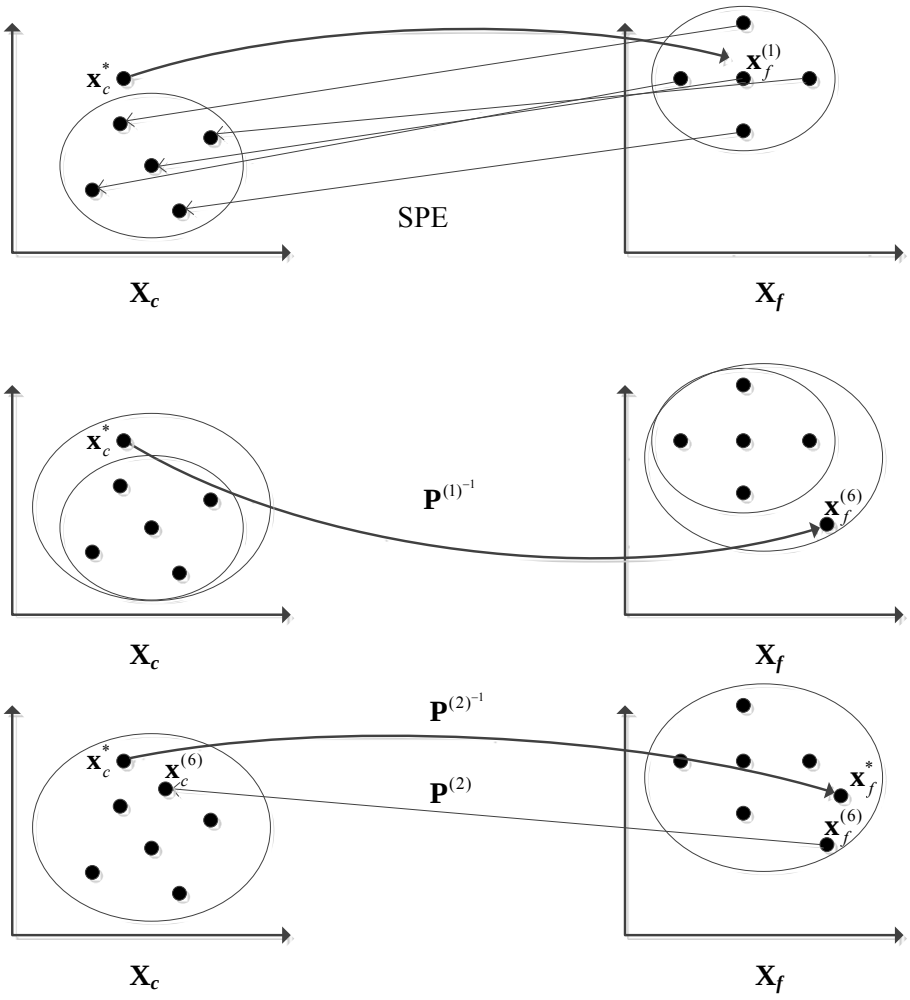


**Figure 2.15.** Illustration of SM optimization process

The next step is to obtain a new point in the fine model using (2.56), and then the response of this point is evaluated and performing coarse model parameter extraction a new point on the coarse space is obtained. In this way, at *j*th iteration, the sets of points in both spaces may be expanded to contain $m_j$ points, which are used to update mapping $\mathbf{P}^{(j)}$. The process is iterated until convergence is achieved, i.e., the response of the fine model $\mathbf{R}_f(\mathbf{x}_f^{(m_j+1)})$ is close enough to the target coarse model response $\mathbf{R}_c(\mathbf{x}_c^*)$. Thus, by satisfying the following expression:

$$\left\| \mathbf{R}_f(\mathbf{x}_f^{(m_j+1)}) - \mathbf{R}_c(\mathbf{x}_c^*) \right\| \leq \varepsilon \tag{2.58}$$

where ε is a certain small value.

The SM optimization process is illustrated in Figure 2.15. It starts by setting the first fine model base point $\mathbf{x}_f^{(1)}$ to be the optimal coarse model $\mathbf{x}_c^*$. Then four additional base points are selected in the vicinity of $\mathbf{x}_f^{(1)}$. SPE is carried out on all five fine model base points to generate the corresponding five coarse model base points. The inverse transformation (inverse of $\mathbf{P}^{(1)}$) is found by using the two existing sets of points and

applied to generate the next fine model base point, the point $m_j+1$, $\mathbf{x}_f^{(6)}$. This point does not satisfy the expression (2.59), thus, the point $\mathbf{x}_c^{(6)}$ is obtained by performing coarse model parameter extraction and applying the updated inverse transformation the final point $\mathbf{x}_f^*$ is obtained.

In this subsection, the original SM approach proposed by Bandler *et al.* has been presented and, as can be seen, the algorithm is simple but has several drawbacks. First, EM analysis must be performed in $m_0$ points at first iteration, and this means high-cost in terms of CPU. Second, a linear mapping may not be valid for certain models. Finally, non-uniqueness in the PE process may lead to an erroneous mapping estimation.

### 2.2.2 Aggressive Space Mapping (ASM)

The ASM algorithm [28] is an improvement of the original SM previously mentioned because quasi-Newton iteration is introduced using the classical Broyden formula [43]. The main idea is to solve the following system of non-linear equations:

$$\mathbf{f}(\mathbf{x}_f) = \mathbf{P}(\mathbf{x}_f) - \mathbf{x}_c^* = 0 \tag{2.59}$$

Let $\mathbf{x_f}^{(j)}$ be the $j$-th approximation to the solution of (2.59) and $\mathbf{f}^{(j)}$ the error function corresponding to $\mathbf{f}(\mathbf{x_f}^{(j)})$. The next vector of the iterative process $\mathbf{x_f}^{(j+1)}$ is obtained by a quasi-Newton iteration according to

$$\mathbf{x}_f^{(j+1)} = \mathbf{x}_f^{(j)} + \mathbf{h}^{(j)} \tag{2.60}$$

where $\mathbf{h}^{(j)}$ is a solution of

$$\mathbf{B}^{(j)}\mathbf{h}^{(j)} = -\mathbf{f}^{(j)} \tag{2.61}$$

and $\mathbf{B}^{(j)}$ is an approximation to the Jacobian matrix $\mathbf{J}_m$ of $\mathbf{f}$ with respect to $\mathbf{x}_f$ at $\mathbf{x}_f^{(j)}$:

$$\mathbf{J}_m(\mathbf{x}_f^{(j)}) = \left( \frac{\partial \mathbf{f}^T(\mathbf{x}_f)}{\partial \mathbf{x}_f} \right)^T \Bigg|_{\mathbf{x}_f = \mathbf{x}_f^{(j)}} \tag{2.62}$$

If the mapping between the two spaces deal with the same type of variables the initial approximation of $\mathbf{J}_m$ is taken as $\mathbf{B}^{(1)}=\mathbf{I}$ (the identity matrix) and $\mathbf{x}_f^{(1)} = \mathbf{x}_c^*$. Otherwise, as in the case of this work, if we have two spaces with different variables we must to determine the initial fine vector $\mathbf{x}_f^{(1)}$ related to the target in coarse space through analytical expressions and the first Broyden matrix $\mathbf{B}^{(1)}$ is initiated as follows:

$$\mathbf{B}^{(1)} = \begin{pmatrix} \frac{\partial x_{c1}}{\partial x_{f1}} & \frac{\partial x_{c1}}{\partial x_{f2}} & \cdots & \frac{\partial x_{c1}}{\partial x_{fm}} \\ \frac{\partial x_{c2}}{\partial x_{f1}} & \frac{\partial x_{c2}}{\partial x_{f2}} & \cdots & \frac{\partial x_{c2}}{\partial x_{fm}} \\ \vdots & \vdots & \cdots & \vdots \\ \frac{\partial x_{cm}}{\partial x_{f1}} & \frac{\partial x_{cm}}{\partial x_{f2}} & \cdots & \frac{\partial x_{cm}}{\partial x_{fm}} \end{pmatrix} \tag{2.63}$$

where the derivatives are obtained by means of the following scheme of finite differences:

$$\frac{\partial x_{ci}}{\partial x_{fi}} \approx \frac{x'_{ci} - x^*_{ci}}{(x_{fi} + \Delta x_{fi}) - x_{fi}} \approx \frac{\Delta x_{ci}}{\Delta x_{fi}} \tag{2.64}$$

where $\Delta x_{fi}$ is small perturbation of the parameters in the fine model and through applying direct parameter extraction the variation of the coarse model, $\Delta x_{ci}$, can be obtained. This operation is repeated $m$ times, which mean that $m$ EM simulations are needed to initialize the Broyden matrix. In the next steps this matrix is updated by the classic Broyden formula [43]:

$$\mathbf{B}^{(j+1)} = \mathbf{B}^{(j)} + \frac{\mathbf{f}(\mathbf{x}_f^{(j)} + \mathbf{h}^{(j)}) - \mathbf{f}(\mathbf{x}_f^{(j)}) - \mathbf{B}^{(j)}\mathbf{h}^{(j)}}{\mathbf{h}^{(j)T}\mathbf{h}^{(j)}} \mathbf{h}^{(j)T} \tag{2.65}$$

and the expression is simplified by combining (2.61) and (2.65):

$$\mathbf{B}^{(j+1)} = \mathbf{B}^{(j)} + \frac{\mathbf{f}^{(j+1)}\mathbf{h}^{(j)T}}{\mathbf{h}^{(j)T}\mathbf{h}^{(j)}} \tag{2.66}$$

where $\mathbf{f}^{(j+1)}$ is obtained by evaluating (2.59) using a certain parameter extraction method providing the coarse model parameters from the fine model parameters. In this work the parameter extraction method is not the same as described in [26, 28] that uses expression (2.57). In our case, we use a direct parameter extraction method based on equivalent circuit model. In this method, the coarse model parameters, usually circuit parameters, are inferred from the *S*-parameters obtained by EM-simulation by means of certain equations at singular frequency points. However, the procedure differs in each case because it depends on the topology used. For this reason, each parameter extraction method will be described in more detail in the corresponding section for each case.

The implementation of the ASM algorithm is described by means of the flow chart depicted in Figure 2.16. The process iterates as explained before and finishes when the norm of error function $\|\mathbf{f}(\mathbf{x}_f)\|$ is smaller than a certain value, $\eta$.

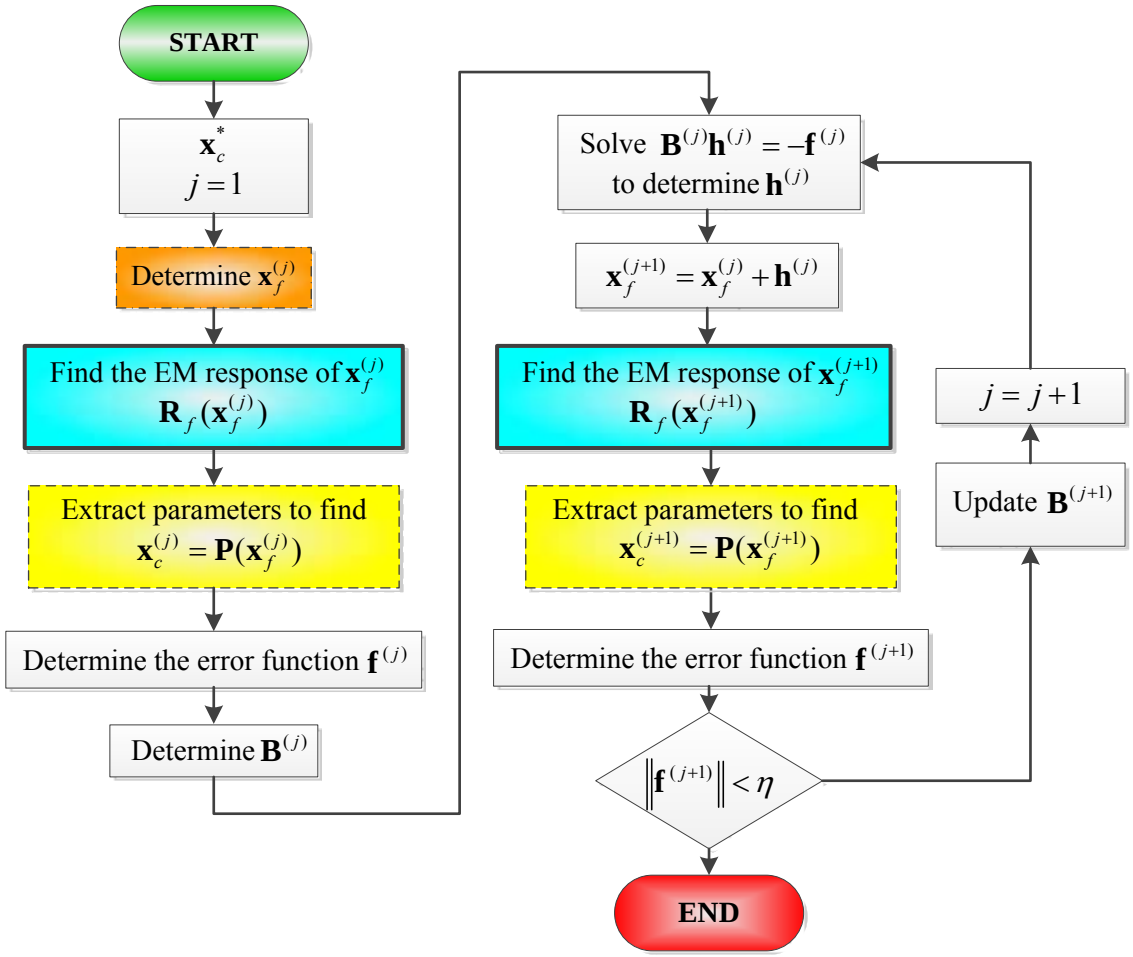


**Figure 2.16.** Flow chart of the ASM algorithm. The stages corresponding to the initial geometry calculator, EM solver and parameter extractor modules are indicated in dashed-dotted, solid and dashed lines respectively.

## 2.3 State of the art

In order to improve the optimization of microwave circuits, several variations of SM have been developed, such as Neural Space Mapping (NSM) [44-46] that uses artificial neural networks (ANNs), or its variant, Neural Inverse Space Mapping (NISM) [46], the implicit Space Mapping (ISM) [47], trust region aggressive space mapping (TRASM) [48], hybrid ASM [49], among others. However, a crucial point in these optimization algorithms is the PE method. Inadequate response data in PE process may lead to non-unique solution. As mentioned before SPE is based on finding the minimum of error function. In this way, several parameter extraction methods have been developed, such as: Multiple Parameter Extraction (MPE) [50, 51], Statistical PE [51], Penalized PE [52], Gradient Parameter Extraction (GPE) [53], among others. As previously mentioned, in

this work the Direct Parameter Extraction[1] (DPE) is used, it consist on linking the model with certain points at frequency response trough analytical expressions. The main advantage of this method falls in how quickly the parameters are extracted, for instance, if the model has four parameters, only four frequency response points are required. However, this procedure is only valid where the model is valid, that is, in that frequency range where the model describes accurately the fine model. Although this method has been widely used in several structures [37, 54], the use of DPE in SM based algorithms was first presented by our group in [55]. The main reason is that a good modeling of the structure is needed and consequently, each topology requires a different parameter extraction.

On the other hand, the application of SM algorithms to metamaterial transmission lines has not been widely used. The pioneering work that has combined SM and metamaterial transmission lines was presented by Roglá *et al.* [56] where an example of SM algorithm applied to the optimization of LH CPW filters with SRRs is reported. Nevertheless, in that article, a statistical approach for parameter extraction has been used instead of DPE. In contrast, apart from the work presented in this thesis, recent contribution has been presented [57] where SM algorithms applied to metamaterial structures by using DPE for parameter extraction, specifically, a microstrip line loaded with CSRR is optimized by means of TASM algorithm. Its results compared with our work will be discussed in section 4.1. However, this places the work presented in this thesis as a pioneer in the application of ASM algorithms to microwave circuits based on metamaterials by using equivalent circuit models and DPE.

[1] Notice that Direct Parameter Extraction (DPE) is firstly named in this work in order to distinguish it from the other parameter extraction methods.

# 3

# Design and implementation of circuits based on resonant-type CRLH unit cells



As mentioned before, the CRLH transmission lines based on the resonant approach are useful for the design of several microwave devices such as filters, power dividers, and hybrid couplers, among others. The main aim of this chapter is to demonstrate the use of a particular case of CRLH line loaded with resonators, that is, the balanced case, where the resonance of the series and shunt branch of the equivalent circuit model are equal. There is not a band gap between the left- and right-handed bands, namely, there is a continuous transition between those bands, and the characteristic impedance is almost constant around the transition frequency. These properties allow to design broadband devices such as high pass filters.

In the following sections, the design process and the several applications of these kinds of lines will be presented in the two most widely used technologies for planar microwave devices.

# 3.1 Design of balanced CRLH resonant unit cells in microstrip technology

As it was mentioned before, a possibility to design a CRLH transmission line in microstrip technology is to use a microstrip line with a series gap and a CSRR etched in the ground plane. The typical topology can be seen in Figure 2.12(a). In this subsection the design of the balance case for these structures will be demonstrated following the process reported in [25, 58-60].

From a theoretical point of view, the design of balanced lines is quite simple. We only need to force the series and shunt resonance frequencies to be equal, that is, $\omega_s = \omega_p = \omega_0$, where this frequencies are related to the electrical parameters of the equivalent circuit model depicted in Figure 2.12(c) through the following expressions:

$$\omega_p = \frac{1}{\sqrt{L_c C_c}} \tag{3.1}$$

$$\omega_s = \frac{1}{\sqrt{L C_g}} \tag{3.2}$$

In these conditions we have two equations, so the five elements of the equivalent circuit are not univocally determined, leaving three degrees of freedom to design a balanced line. An additional condition could be added if we fix the transmission zero frequency, $\omega_z$, using equation (2.53). Even so, two design parameters still need to be defined. An interesting point could be to set the characteristic impedance at two certain frequencies. This can be made by using the simplified expression for the balance case:

$$Z_B = \sqrt{\frac{L}{C_c} + \frac{L}{C}\left(1 - \frac{\omega_0^2}{\omega^2}\right) - \frac{L^2\omega^2}{4}\left(1 - \frac{\omega_0^2}{\omega^2}\right)^2} \tag{3.3}$$

Alternatively, phase shift at two frequencies could be imposed through the dispersion relation for the balanced case:

$$\cos(\beta l) = 1 - \frac{C\left(\omega^2 - \omega_0^2\right)^2}{2C_g\omega_0^4\left(L_c\left(C_c + C\right)\omega^2 - 1\right)} \tag{3.4}$$

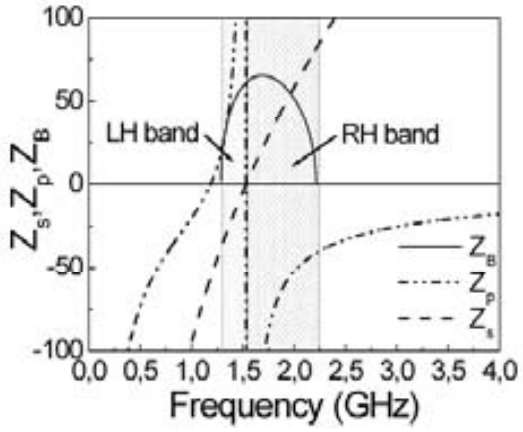


**Figure 3.1.** Reactance of the series, $Z_s$, and shunt, $Z_p$, impedance, and real part of the characteristic impedance, $Z_B$, for a model of CRLH CSRR-based transmission line for balanced case ($\omega_s=\omega_p=\omega_0$). Electrical parameters are: $L$ = 22.5 nH, $C_g$ = 0.48 pF, $C$ = 4 pF, $C_c$ = 6 pF, $L_c$ = 1.8nH. The transmission frequency has been set to 1.5 GHz. Figure extracted from [58].

In Figure 3.1 an example of the characteristic impedance corresponding to the circuit model [Figure 2.12(c)] of a balanced CRLH CSRR-based line is depicted. Notice that, contrary to the non-resonant CRLH lines, where for the balanced case the characteristic impedance reaches its maximum at $\omega_0$, for CSRR-based CRLH lines the impedance is a maximum above the transition frequency. Nevertheless, the impedance variation in the vicinity of this frequency is smooth and this is interesting to achieve broadband characteristics due to the possibility of preserving matching in a wide band.

Figure 3.2. Layout and photograph (top face) of the fabricated CSRR-based CRLH balanced line. Dimensions are: line width $W$ = 0.8 mm, external radius of the outer ring $r_{ext}$ =7.3 mm, rings width $c$ = 0.4 mm and rings separation $d$ = 0.2 mm; the interdigital capacitor is formed by 28 fingers separated 0.16 mm. Figure extracted from [58].

Although, the design of this kind of lines has been analyzed from a theoretical point of view, in practice, forcing the two frequencies to be equal is not an easy issue, mainly due to the low value of the series gap in these structures which involves a high series resonance frequency far from the shunt resonance frequency. Indeed, we need to increase the value of the capacitance $C_g$ of the transformed circuit model depicted in Figure 2.12(c) and according to the expressions (2.48), (2.49) it depends linearly on the parameters $C_f$, $C_L$ and $C_s$. The first element, $C_f$, is a parasitic element and it is supposed to be negligible. The second, $C_L$, is related to the line capacitance and to increase its

value it is necessary to widen the host line which brings us to reduce the line inductance and consequently the series inductance $L$ which is not recommended because it increases the series resonance frequency. The last element, $C_s$, actually models the series gap and in order to increase its value, it is necessary to use T-shaped gap or interdigital capacitors. In order to demonstrate the characteristics of CSRR-loaded CRLH balanced transmission lines, a unit cell structure has been designed and fabricated. The topology of the structure and a photograph of the fabricated device can be seen in Figure 3.2. This structure has been fabricated by using a commercial *Rogers RO3010* substrate with thickness $h$ = 1.27 mm and relative dielectric constant $\varepsilon_r$=10.2. Hence, the structure has been measured and compared with EM simulation, as well as with its extracted equivalent circuit model. The parameter extraction procedure is similar to that described in [54], but it will be explained in detail in section 4.2 with the automated synthesis of this kind of structures. The dispersion relation and frequency response of the designed unit cell is depicted in Figure 3.3. It can be observed in dispersion diagram [Figure 3.3(a)] that there is a small gap between the LH and RH band; hence, to be precise, it is a CRLH structure roughly balanced, but also a broad transmission band is obtained, as it can be seen in the frequency response [Figure 3.3(b)]. Good agreement between all the curves has been achieved, except at high frequencies, where the equivalent circuit model depicted in Figure 2.12(c) fails since the unit cell is not electrically small, and the effects of distributed parameters are not negligible. Nevertheless, the structure has a broadband frequency response up to 3 GHz and it is potentially a candidate to be applied to the design of high pass filters, as it will be discussed in section 3.3.

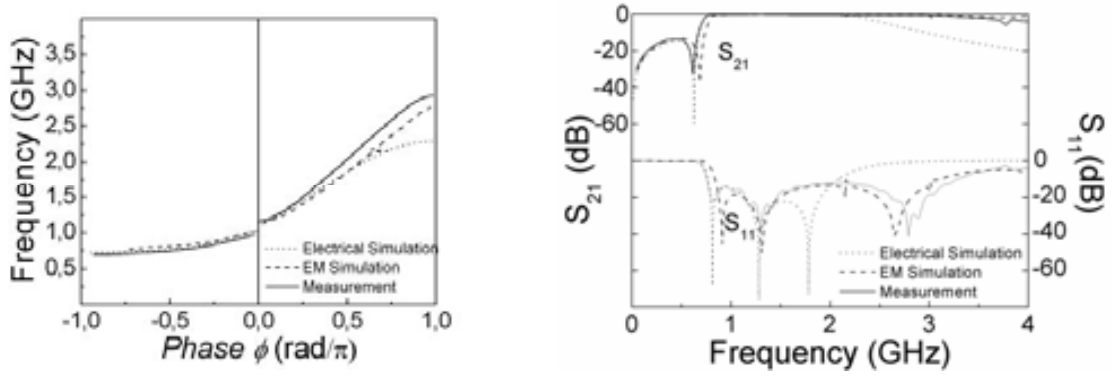


(a) (b)

**Figure 3.3.** Dispersion diagram (a) and frequency response (b) of equivalent circuit model (dotted line), EM simulation (dashed line) and Measurement (solid line) corresponding to the designed cell of Figure 3.2. Figure extracted from [58].

### 3.1.1 CRLH transmission lines loaded with Complementary Spiral Resonators

Another example of the design of a resonant type CRLH transmission line is by means of a Complementary Spiral Resonator (CSR). The design process is roughly the same to the previous described one, but in this case the resonator is electrically smaller than the CSRR, which is interesting for size reduction [35]. In this subsection, the use of CSR for the design of CRLH balanced lines will be analyzed, and an example of a designed unit cell is shown.

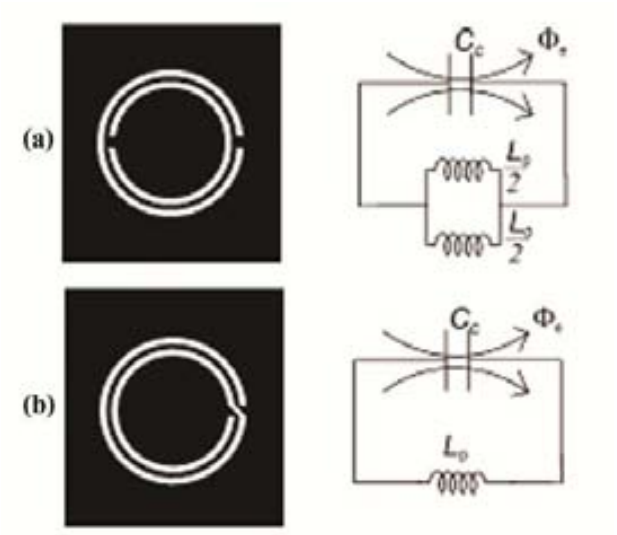


**Figure 3.4.** Topology of the CSRR (a) and CSR (b). The equivalent circuit model of the respective particles are also indicated on the right. Figure extracted from [59].

The CSR is a sub-wavelength resonator etched in a metallic layer like the CSRR, but in this case the outer and inner rings are connected through a slot connection. In Figure 3.4 the typical topology of both resonators are depicted, as well as their equivalent circuits. Notice that, the capacitance is the same in both resonators, nonetheless, the inductance of CSR is the inductance of the inter-ring metal, and otherwise the inductance of the CSRR is the parallel combination of the two inductances connecting the inner disk to the ground. As a result, the inductance of CSR is four times that of the CSRR. Consequently, the resonance frequency of CSR is half the resonance frequency of the CSRR. This explains that the electrical length, specifically the diameter, of the CSR is roughly half that of the CSRR for the same resonance frequency.

**Figure 3.5.** Topology of the unit cell of CSR-loaded CRLH microstrip lines. Figure extracted from [59].

In order to demonstrate the potentially to use a CSR for CRLH balanced lines, a unit cell has been designed [59]. The design process is similar to the one described before for a CSRR, since a microstrip line with series gap is loaded with CSR instead of CSRR. So the equivalent circuit of the unit cell is the same, and therefore also the design equations. The main difference in this case is that to balance the CRLH line, the inductance of the host line has had to be increased in addition to the series capacitance. To this end, meander lines have been used. The topology of the designed unit cell is depicted in Figure 3.5. Notice that, part of ground plane has been etched beneath the interdigital capacitor in order to reduce the line capacitance and consequently reduce the capacitance *C*. This has been done in order to locate the transmission zero close to the band. The frequency response and the dispersion diagram are depicted in Figure 3.6. Good agreement between both the EM and circuit simulation results, except at high frequencies, where the equivalent circuit model fails.

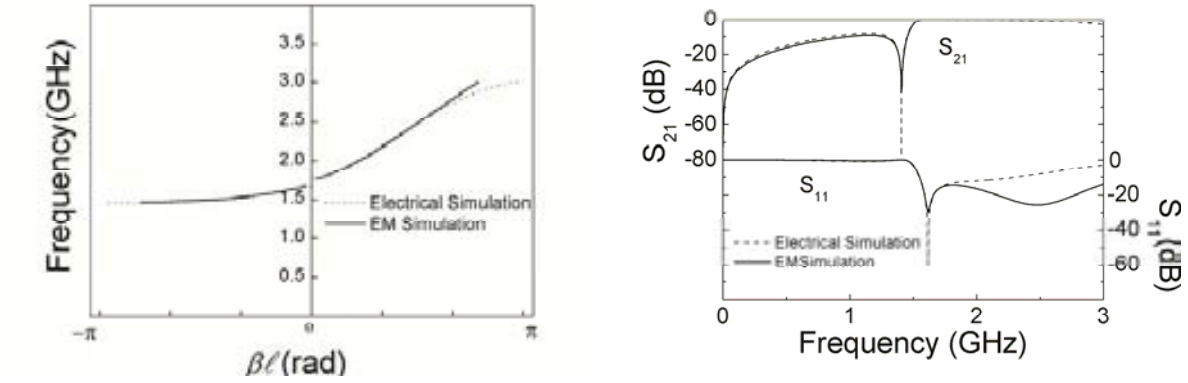


(a) (b)

**Figure 3.6.** Dispersion diagram (a) and frequency response (b) of the designed CSR-loaded unit cell shown in Figure 3.5, dimensions are: external radius of the CSRs $r_{ext}$ = 2.55 mm, width of the rings $c_{in}$ = 0.294 mm, $c_{out}$ = 0.221 mm and rings separation $d$ = 0.225 mm. The interdigital capacitances are implemented by means of 14 fingers 0.16 mm wide and separated a distance of 0.16 mm. Line width is $W$ = 0.2 mm and the circular window etched in the ground plane has radius of 0.95 mm. Figure extracted from [59].

## 3.2 Design of balanced CRLH cells in CPW technology

Previously, the implementation of CRLH transmission lines by means of SRRs in CPW technology was discussed. In this section, the balanced case for this kind of lines is demonstrated [61]. Following the case of CSRR-loaded CRLH balanced lines, the design process and an illustrative example is shown.

To balance the line, it is necessary to force the shunt resonance and the series resonance of the transformed π-circuit model of the Figure 2.9(b) to be equal. These frequencies are expressed as follows:

$$\omega_p = \sqrt{\frac{2}{L_p' C}} \tag{3.5}$$

$$\omega_s = \sqrt{\frac{L' + L_s'}{L' L_s' C_s'}} \tag{3.6}$$

From this, the following condition is obtained:

$$L_p' C = \frac{2 L' L_s' C_s'}{L' + L_s'} \tag{3.7}$$

and by using expressions (2.40)-(2.43) the element values of Figure 2.9(a) must satisfy:

$$\left(4L_p + L\right)\frac{C}{2} = \frac{C_s\left(2LL_pL_s + LM^2 - 4M^2C_s\omega_0^2L_sL_p - M^2C_s\omega_0^2L_sL\right)}{L_pL} \tag{3.8}$$

Similarly to the case of CSRR-loaded CRLH lines, there are three degrees of freedom in the design of this kind of lines, but it could be interesting to set the characteristic impedance of the structure close to the reference impedance of the ports (usually 50 Ω). For the balance case, expression (2.47) is simplified to:

$$Z_B = \left( \frac{-\omega^3 L_p'^2 \left(L' + L_s'\right)}{\omega\left(L' + L_s'\right)\left(1 - \frac{\omega^2}{\omega_p^2}\right)^2 + 2\omega L_p'\left(1 - \frac{\omega^2}{\omega_0^2}\right)} \right)^{\frac{1}{2}} \tag{3.9}$$

and it exhibits a continuous variation in the vicinity of the transition frequency, and the characteristic impedance is roughly constant in a wide band.

Alternatively, it may be interesting to impose conditions on the phase shift, instead of the impedance for certain purposes. To this end, the following simplified dispersion relation has to be taken in to account:

$$\cos\beta l = 1 + \frac{L'\left(\omega_p^2 - \omega^2\right)^2}{L_p'\omega_p^2\left(\omega_0^2 - \omega^2\right)} \tag{3.10}$$

Furthermore, the transmission zero frequency can also be used to force an additional condition for the element values of the equivalent circuit model. It could be useful if a certain level of rejection is required in a particular frequency.

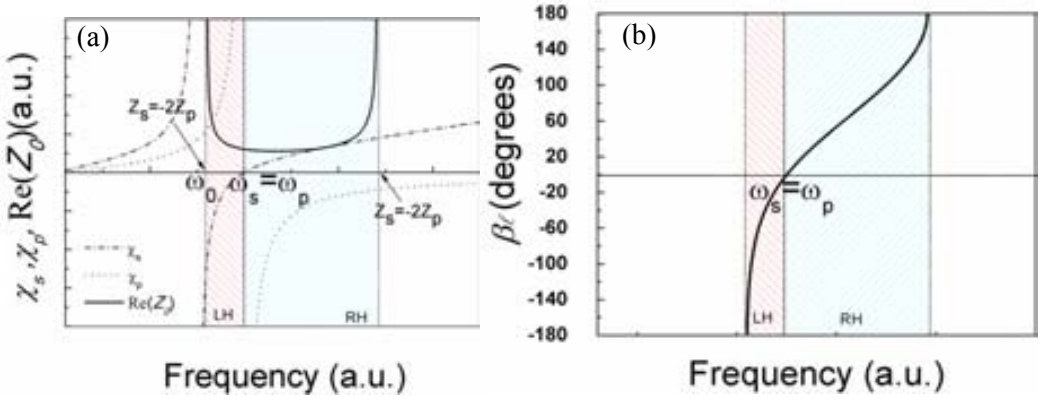


**Figure 3.7.** Series and shunt reactance, characteristic impedance (a) and dispersion diagram (b) for the model depicted in Figure 2.9(b). for the balanced case where $\omega_s = \omega_p$.

In Figure 3.7 the characteristic impedance and dispersion diagram of SRR-based CRLH lines for the balanced case is depicted. It could be seen that the characteristic impedance begins from infinity at LH band and reaches its minimum above the transition frequency at RH band and tends to infinity at the end of this band.

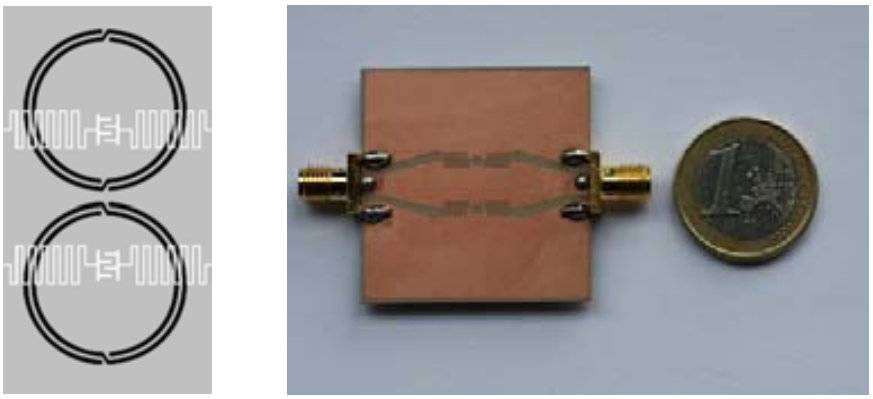

**Figure 3.8.** Layout and photograph (top face) of the fabricated device. Dimensions are: external radius of SRR $r_{ext}$ = 4.68 mm, rings width $c$ = 0.223 mm and rings separation $d$ = 0.237 mm. Meander width $W_m$ = 0.2 mm and separation distance $s_m$ = 0.2 mm. The gap distance between the line and the ground planes is $g$ = 0.16 mm.

Concerning the design of SRR-loaded CRLH balanced lines, forcing the two frequencies to be identical, in practice, is a difficult because the inductance $L_p'$ as well as the capacitance $C$, of the transformed circuit model of Figure 2.9(b) must be higher than that of the typical values that can be extracted from the structure depicted in Figure 2.8. To this end, the capacitance of the host line is increased, since it is related to the element $C$. It can be achieved by means of interdigital capacitors. Additionally, it is necessary to increase the shunt inductance connected to the ground, since the inductance $L_p'$ depends strongly on its value, according to the expression (2.43). Hence, meander lines are required. As an illustrative example, a balanced CRLH transmission line loaded with SRR has been designed and fabricated on a substrate with dielectric

constant $\varepsilon_r$ = 11.2 and thickness $h$ = 1.27 mm . The layout of the unit cell is depicted in Figure 3.8 and relevant dimensions are indicated. In Figure 3.9, the dispersion diagram inferred from EM simulation, measurement and from circuit simulation from the model depicted in Figure 2.9(b) with the extracted parameters using the method reported in [62], are depicted. Although perfect balance is not achieved, as occurs in the case of CSRR-loaded balanced lines, the effects of the small gap between the two bands on the transmission characteristics of the device are irrelevant, and it is suitable for filter applications, as will be discussed in section 3.3.

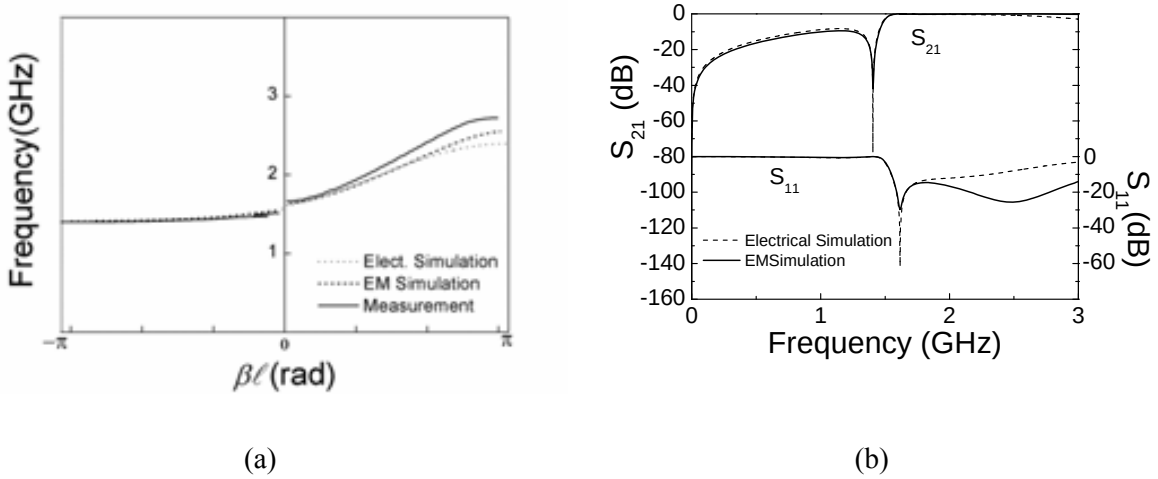


(a) (b)

**Figure 3.9.** Dispersion diagram (a) and frequency response (b) of equivalent circuit model (dotted line), EM simulation (dashed line) and Measurement (solid line) corresponding to the designed unit cell.

## 3.3 Application to the design of high pass filters based on CRLH cells

To illustrate the potentiality of balanced CRLH lines loaded with subwavelength resonators, like the CSRRs or the SRRs, to the design of wideband filters, several prototype device examples are provided. Mainly, these examples are based on the balanced unit cells shown in the previous sections. Specifically, by cascading several of these cells, high pass filters can be obtained.

First of all, a three-stage high pass filter based on CSRRs is presented. The design of the filter to satisfy any given specifications can be done through the equivalent circuit model of the unit cell depicted in Figure 2.12. Nonetheless, in this case, an arbitrary balanced line has been designed to demonstrate the capabilities of this kind of lines. Specifically, the unit cell previously studied (see Figure 3.2), has been used to form the three-stage device depicted in Figure 3.10. This structure was first presented in [60] as a high pass filter. Indeed, it is a band pass filter as reported in [25], but the upper stop

band is not controllable, contrary to other examples using the resonant approach [23, 63-65].

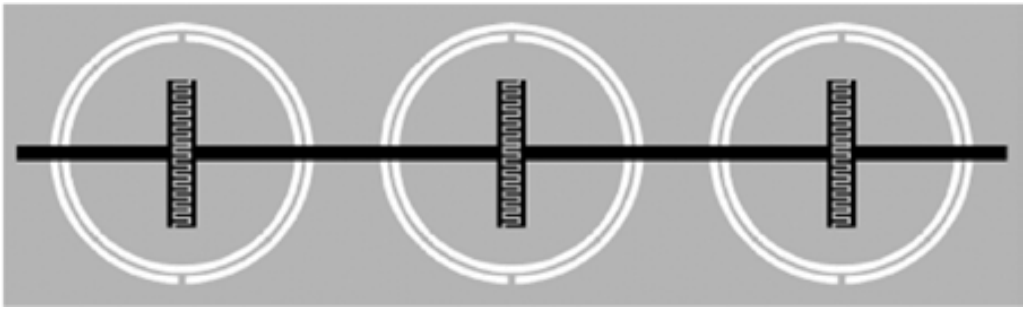

**Figure 3.10.** Layout of the filter formed by three CSRR-loaded cells. Dimensions are: total length $l$ = 55 mm, line width $W$ = 0.8 mm, external radius of the outer rings $r_{ext}$ =7.3 mm, rings width $c$ = 0.4 mm and rings separation $d$ = 0.2 mm; the interdigital capacitor is formed by 28 fingers separated 0.16 mm. Figure extracted from [60].

In order to illustrate the feasibility of these filters by means of CSRR-loaded CRLH balanced lines, the designed three-stage high pass filter has been fabricated. Measured and simulated frequency response of the device is shown in Figure 3.11. Furthermore, two- and four- stage structures have been simulated and their frequency response is also depicted in Figure 3.11. The cutoff frequency is located at 0.75 GHz with a rejection level better than 40dB below the transmission frequency. Good agreement between simulation and measurement results, except at high frequencies.

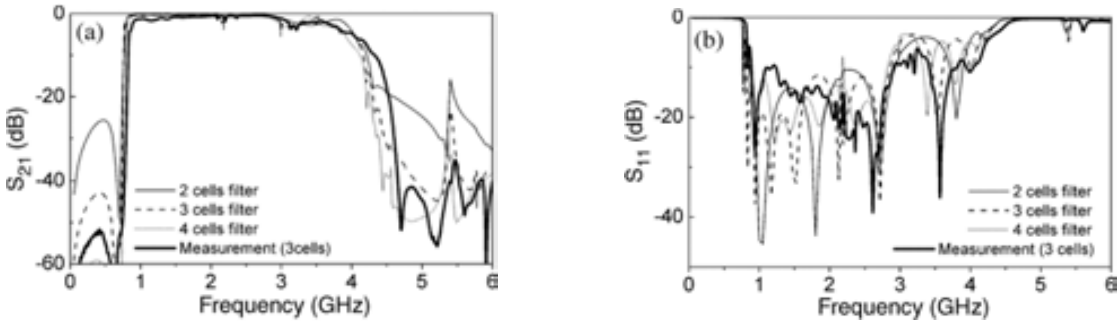


**Figure 3.11.** Frequency response of EM Simulation: (a) transmission coefficient ($S_{21}$) (b) reflection coefficient ($S_{11}$) of the three filters composed of two-, three-, and four-stages identical to those of Figure 3.10. The measured frequency response of the fabricated prototype is also depicted. Figure extracted from [25].

The second example is a high pass filter based on CSRs. In this case, a four-stage filter has designed in order to achieve a sharp cutoff. The unit cell previously mentioned (see Figure 3.5) has been used to demonstrate its potential for high pass filter implementation. The layout and a photograph of the fabricated device is shown in Figure 3.12. This filter has been designed to exhibit a 3dB cutoff frequency at 1.5GHz and a good rejection below it. To this end, the transmission zero has been situated near the pass band, and to achieve it, the circular window etched within the CSR has been added. The simulated and measured frequency response of the device is depicted in

Figure 3.13. Good agreement between simulation and measurement is obtained, as well as, a good performance. The insertion loss in the band pass is IL < 2.2dB, the rejection level is better than 40 dB to the left of the transmission zero and there is a sharp transition between pass and stop band (a rise of 40 dB in just 150 MHz).

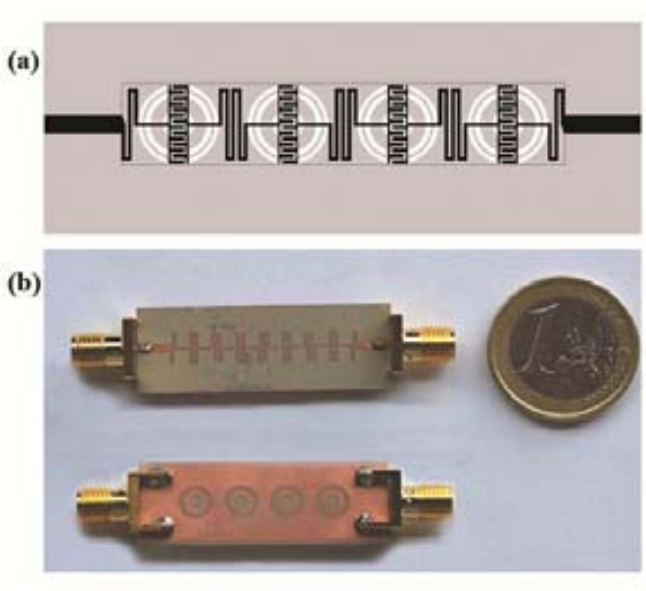


**Figure 3.12.** Layout (a) and photograph (b) of the fabricated filter formed by four CSR-loaded cells. Dimensions are: total length $l$ = 28.8 mm, external radius of the CSRs $r_{ext}$ = 2.55 mm, width of the rings $c_{in}$ = 0.294 mm, $c_{out}$ = 0.221 mm and rings separation $d$ = 0.225mm. The interdigital capacitances are implemented by means of 14 fingers 0.16 mm wide and separated a distance of 0.16 mm. Line width is $W$ = 0.2 mm and the circular window etched in the ground plane has radius of 0.95 mm. Figure extracted from [59].

It is worth mentioning that the filter length, excluding access lines, is 28.8 mm, which is only $0.37\lambda_g$, where $\lambda_g$ is the guided wavelength at the cutoff frequency (1.5 GHz). Hence, the miniaturization of high pass filters based on CRLH lines by means of CSRs has been demonstrated.

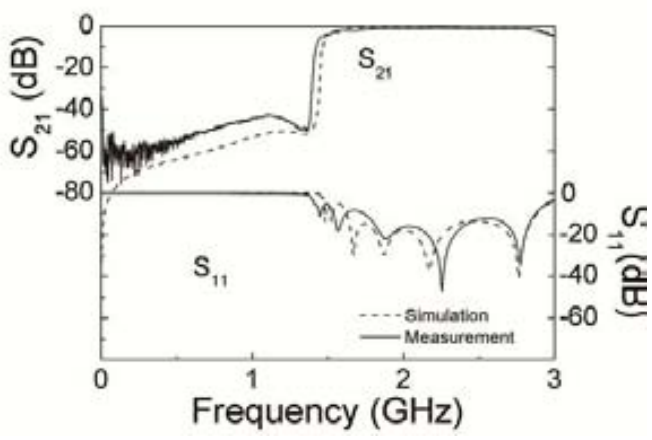


**Figure 3.13.** Simulated (dashed) and measured (solid) frequency response of the fabricated filter depicted in Figure 3.12. Figure extracted from [59].

At last, but not least, a high pass filter implemented by means of SRR in CPW technology is presented. Similarly to the previous examples, a device based on a balanced unit cell has been designed and fabricated. In this case, a three-stage high pass filter with transmission zero located around 1.4 GHz has been designed. The layout, as well as a photograph of the device is depicted in Figure 3.14, the total dimensions of the filter (excluding access lines) are 20.8 mm x 35.2 mm. The frequency response of EM simulation and Measurement of the device is depicted in Figure 3.15. Good agreement between simulation and experiment results except some frequency shift due to fabrication tolerances. The rejection in the stop band is better than 30dB and insertion losses in the band pass are IL < 2dB in the measured response.

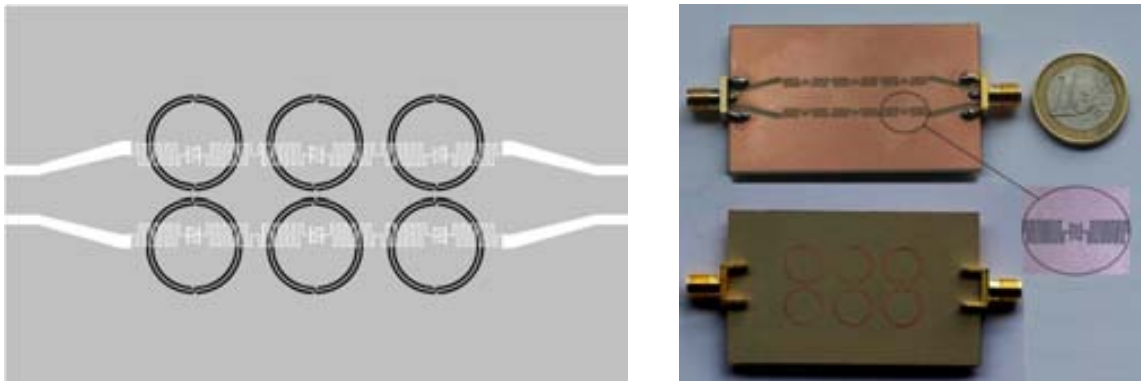

(a) (b)

**Figure 3.14**. Photograph of the fabricated filter, dimensions are: external radius of the SRRs $r_{ext}$ = 4.68mm, width of the rings $c$ = 0.223mm, and rings separation $d$ = 0.237mm. The shunt inductance has been implemented by means of a meander with width $w_m$ = 0.2mm and separation distance $s_m$ = 0.2mm. Furthermore, the gap distance between the line and the ground planes is $g$ = 0.16mm. Figure extracted from [61].

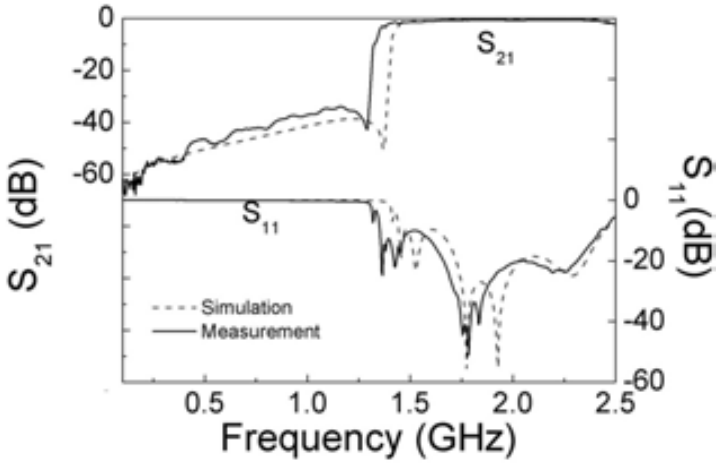


**Figure 3.15.** Simulated (dashed) and measured (solid) frequency response of the fabricated filter shown in Figure 3.14. Figure extracted from [61].

In **summary**, the design and implementation of circuits based on resonant-type CRLH unit cells have been introduced in this chapter. Specifically, the use of CSRR, CSR and SRR to obtain balanced unit cells has been reported. The characteristic impedance and dispersion relation have been analyzed for the balanced case and the design equations related to the circuit model parameters have been shown. Finally, the application of resonant type CRLH balanced lines to the design of microwave broadband filters has been demonstrated and several illustrative examples have been presented in the two most widely used technologies for planar microwave devices (microstrip and CPW technology).

# 4

# Automated synthesis of CSRRs based circuits through ASM



In this chapter the automated synthesis of circuits based on sub-wavelength resonators is introduced. Specifically, the synthesis of CSRR-loaded transmission line unit cells through ASM is considered including the negative effective permittivity unit cell, and the CRLH line, both in microstrip technology. The core of the algorithm as well as the main functions are discussed in detail for each case. Furthermore, algorithm improvements like the determination of the convergence region and the reduction of the time to convergence through a novel two-step algorithm are shown.

## 4.1 Negative effective permittivity microstrip cell based on CSRRs

In this section, the iterative ASM procedure presented in section 2.2 (see Figure 2.16) is applied to the synthesis of a microstrip line with a CSRR [34] etched in the ground plane [see Figure 4.1(a)]. This structure is the unit cell for the design of planar structures exhibiting a negative value of the effective permittivity [6, 34]. They can also be used as building blocks for the design of stop band filters [66]. However, the main reason for choosing a CSRR-loaded microstrip transmission line as the first case study for the application of the implemented ASM algorithm is the relative complexity associated with the synthesis of these structures, where distributed and semi-lumped elements (CSRRs) are combined.

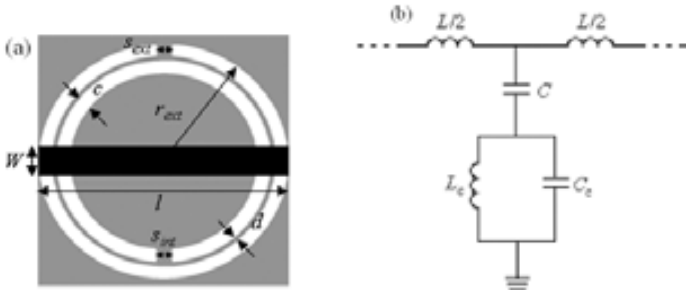


**Figure 4.1.** Typical topology (unit cell) of a CSRR-loaded microstrip line (a) and equivalent T-circuit model (b). The relevant geometrical parameters of the structure are indicated

The equivalent circuit model of the CSRR-loaded microstrip line is depicted in Figure 4.1(b) [35]. This model is similar to the one presented in section 2.1(see Figure 2.12), but in this case without gap and, in contrast to the CSRR-loaded CRLH line, there is not LH propagation band. In this model, $L$ is the inductance of the line, $C$ accounts for the capacitance between the upper metallic strip (line) and the metallic region inside the CSRR, whereas $L_c$ and $C_c$ account for the inductance and capacitance of the CSRR. These elements are the coarse model parameters. Although seven geometrical parameters are necessary to define the layout of the structure [see Figure 4.1(a)], we will consider from now on that the microstrip line length is twice the external radius of the CSRR, $l = 2r_{ext}$. Moreover, split dimensions are taken as $s_{ext} = 0.07r_{ext}$ for the external ring, and $s_{int} = 0.07(r_{ext}\text{-}c\text{-}d)$ for the internal ring. This corresponds, approximately, to a gap aperture of 4 degrees for each ring. In that way, the considered geometrical parameters are reduced to four: $c$, $d$, $r_{ext}$ and $W$ (these are the variables of the fine model). The validity of the model of Figure 4.1(b) is subjected to two conditions: (i) the CSRR must be electrically small, and (ii) the microstrip line must not extend much beyond the limits of the CSRR (so that parasitic transmission line effects are precluded). For this last reason we have forced $l = 2r_{ext}$. In some cases, a small portion of line length (typically around 1%-2%) can be added, for example, if it is necessary to cascade several cells or to ensure that the ports of the structures are accessible.

In the following subsections, the different main modules and the core program of the ASM algorithm for the considered structure will be explained. First of all, the initial geometry calculator that estimates the first vector in the fine model will be presented. Second, the module responsible to find the frequency response of $\mathbf{x}_f^{(j)}$, the so-called EM solver module, will be explained. In the third subsection, the parameter extraction method for the CSRR-loaded microstrip line is reported. Finally, the whole process of automated synthesis of the aforementioned structure by means of ASM algorithm will be illustrated through an example.

### 4.1.1 Initial geometry estimation

Concerning the module for the determination of the initial geometry, namely the initial geometry calculator, the analytical model for a microstrip structure [29] and the CSRR model reported in [35], have been used. Specifically, from the values of $C$ and $L$, we infer the characteristic impedance of the host line (2.14), and from well-known formulas [29] we determine the width $W$ of the line corresponding to this impedance value:

$$\frac{W}{h}=\begin{cases}\dfrac{8e^{A}}{e^{2A}-2} \\ \dfrac{2}{\pi}\left[B-1-\ln(2B-1)+\dfrac{\varepsilon_r-1}{2\varepsilon_r}\left\{\ln(B-1)+0.39-\dfrac{0.61}{\varepsilon_r}\right\}\right]\end{cases} \quad \begin{matrix}\text{for} \\ W/h<2\end{matrix} \tag{4.1}$$

where

$$A=\frac{Z_0}{60}\sqrt{\frac{\varepsilon_r+1}{2}}+\frac{\varepsilon_r-1}{\varepsilon_r+1}\left(0.23+\frac{0.11}{\varepsilon_r}\right) \tag{4.2}$$

$$B=\frac{377\pi}{2Z_0\sqrt{\varepsilon_r}} \tag{4.3}$$

and $\varepsilon_r$ and $h$ are the dielectric constant and thickness of the substrate, respectively. Obviously, from the values of $L$ and $C$, the length of the host line can also be determined, by rewriting expression (2.15) as follows:

$$l=v_p\sqrt{LC} \tag{4.4}$$

However, since we are considering that $l = 2r_{ext}$, the length of the host line for the initial layout is determined after the CSRR dimensions are obtained. To determine the CSRR dimensions, we set the value of the rings width to a reasonable value, namely, $c$ = 0.25 mm, and from the values of $C_c$ and $L_c$, we can univocally determine $r_{ext}$ and $d$. To this end, the model reported in [35] has been used. Actually, the model provides the reactive elements of the CSRR from its geometry, so that we have swept $d$ and $r_{ext}$

(driven through a minimum finder algorithm combined with a program developed by Baena *et al.*) until the required values of $C_c$ and $L_c$ are found. This is, however, very fast since only two design parameters are involved in the optimization process. The capacitance $C_c$ is given by expression (1) in [35], whereas the inductance $L_c = L_o/4$, where $L_o$ is the inductance corresponding to a circular CPW structure of length $2\pi r_o$, strip width $d$, and slot width $c$ (the detailed formula is given in [67]).

### 4.1.2 EM solver

The main function of EM solver module is to provide the frequency response for a given vector in the fine model $\mathbf{x}_f^{(j)}$. This module acts as a link between the main program and the corresponding EM simulator. In our case, the MATLAB commercial software is used to control the main program as well as its modules and *Agilent Momentum* is used as the EM simulator. It is worth mentioning that this module can be implemented to call different EM simulators, such as, *Ansoft Designer*, *CST*, among others. Indeed, our co-workers from iTEAM-UPV use *Ansoft Designer* in their EM solver module [68-70]. Once the fine model vector is given, on the one hand, the topology of the strip line (upper metal layer) is provided by giving the rectangle vertices and, on the other hand, the topology of the CSRR (lower metal layer) is generated from polar to Cartesian coordinate transformation, and the circumferences defining the perimeter of the rings are actually 180-side polygons. With these points, the EM solver creates a suitable text file containing the layout information and with predefined substrate characteristics, frequency range and mesh options *Agilent Momentum* is called to perform the EM full-wave simulation. Then, the frequency response is obtained and transferred to the main program. The development and block diagram of the EM solver will be discussed in more detail in Appendix A.

### 4.1.3 Parameter extraction method

With regard to the parameter extractor module, the results of the EM solver are used to obtain the parameters of the circuit model of Figure 4.1(b). These parameters are inferred from the EM simulated S-parameters according to the procedure described in [54], where three singular frequencies must be identified: (i) the transmission zero frequency, $f_z$,

$$f_z = \frac{1}{2\pi\sqrt{L_c(C+C_c)}} \tag{4.5}$$

where the impedance of the shunt branch of the circuit model nulls (similarly to the case mentioned in section 2.1), (ii) the frequency that opens the shunt branch, $f_o$,

$$f_o = \frac{1}{2\pi\sqrt{L_c C_c}} \tag{4.6}$$

where $S_{11}$ intercepts the unit resistance circle in the Smith Chart (this frequency is the resonance frequency of the CSRRs); and (iii) the frequency providing –90º phase shift for $S_{21}$ ($f_{-\pi/2} = \omega_{-\pi/2}/2\pi$), where the series and shunt impedances of the circuit model satisfy [54]:

$$Z_s(\omega_{-\pi/2}) = -Z_p(\omega_{-\pi/2}) \tag{4.7}$$

As we have mentioned, at the frequency where $S_{11}$ intercepts the unit resistance circle in the Smith Chart, the shunt branch opens and hence the impedance of the circuit model, $Z_{in}(f_o)$, can be written as:

$$Z_{in}(f_o) = Z_o + j2\pi f_o L \tag{4.8}$$

$Z_o$ being the reference impedance of the ports ($Z_o = 50\Omega$). Thereby, equations (4.5)-(4.8) are the four required conditions to determine the parameters of the circuit model. By means of the EM solver module, the S-parameters generated by EM simulator (e.g. *Agilent Momentum*) are exported to the main program controlled by MATLAB and the parameter extraction module uses these data to identify the frequencies $f_z$, $f_o$ , $f_{-\pi/2}$ and the impedance $Z_{in}(f_o)$, and to solve equations (4.5)-(4.8). Thus the parameters of the equivalent circuit model of Figure 4.1(b) are extracted and transferred to the main program and its corresponding module (in order to determine the error function or obtain the initial Broyden matrix, as will be explained in the following subsection).

### 4.1.4 Automated synthesis

Let us now consider the whole process of automated synthesis of a negative effective permittivity unit cell. First of all, we determine the initial geometry by using the corresponding module. From this geometry, we find the EM frequency response by means of the EM solver module and by using the parameter extractor module, the circuit parameters are obtained, and hence we have the error function **f** expressed as follows:

$$\mathbf{f}(\mathbf{x_f}) = \mathbf{x_c^*} - \mathbf{x_c} = \left(L^* - L, \quad C^* - C, \quad L_c^* - L_c, \quad C_c^* - C_c\right) \tag{4.9}$$

The next step is to determine the first Broyden matrix $\mathbf{B}^{(1)}$ that, in this case, can be expressed as follows:

$$\begin{pmatrix} \frac{\delta L}{\delta W} & \frac{\delta L}{\delta r_{ext}} & \frac{\delta L}{\delta c} & \frac{\delta L}{\delta d} \\ \frac{\delta C}{\delta W} & \frac{\delta C}{\delta r_{ext}} & \frac{\delta C}{\delta c} & \frac{\delta C}{\delta d} \\ \frac{\delta L_c}{\delta W} & \frac{\delta L_c}{\delta r_{ext}} & \frac{\delta L_c}{\delta c} & \frac{\delta L_c}{\delta d} \\ \frac{\delta C_c}{\delta W} & \frac{\delta C_c}{\delta r_{ext}} & \frac{\delta C_c}{\delta c} & \frac{\delta C_c}{\delta d} \end{pmatrix} \tag{4.10}$$

In order to obtain the derivatives, each geometrical parameter is slightly perturbed from the value obtained in the first layout. Hence, the EM response is found and the circuit parameters corresponding to each geometry variation are extracted. Once the Broyden matrix is known, the equation (2.61) is solved and from (2.60) the geometry of the following iteration is derived (in order to avoid too extreme geometrical dimensions, either not implementable in a certain technology or electrically non-small, the constrained approach has been used[2] [71]). Then, the EM response is found for the new geometry and the circuit parameters are extracted, the error function $\mathbf{f}(\boldsymbol{x}_f)$ is evaluated according to the following standard norm:

$$\left\|\mathbf{f}(\mathbf{x}_f)\right\| = \sqrt{\left(L^* - L\right)^2 + \left(C^* - C\right)^2 + \left(L_c^* - L_c\right)^2 + \left(C_c^* - C_c\right)^2} \tag{4.11}$$

where the capacitive values are given in pF and the inductances in nH (this is the standard procedure used in ASM algorithm, but a better form to evaluate the error function will be discussed in subsection 4.2.4).

Finally, the process is iterated as explained in section 2.2 until convergence is obtained. It is worth to mention that, for next iterations the Broyden matrix is updated following the Broyden formula [43] in its simplified expression (2.66), thus, the EM solver is no needed to update it.

Notice that, the circuit model of Figure 4.1(b) is valid in a limited frequency range. Although the considered frequency interval is not critical, it must include the frequencies of interest, namely, those necessary to extract the circuit parameters present in equations (4.5)-(4.8). Hence, the maximum considered frequency is set to $f_{max}=2f_z$.

As previously mentioned, the core program is controlled from the MATLAB commercial software. Thus, the constitutive modules as well as the ASM algorithm have been developed by using MATLAB language.

To illustrate the automatic synthesis of negative effective permittivity microstrip unit cells based on CSRR and its capabilities, two different examples will be shown. The

[2] The constrained approach consist on decrease vector $\boldsymbol{h}^{(j)}$ in the same quasi-Newton direction by a shrinking factor $\delta$, when the new solution of equation (2.60) is not within certain limits.

considered substrate in both cases is the *Rogers RO3010* substrate with dielectric constant $\varepsilon_r$ = 10.2 and thickness $h$ = 1.27 mm.

#### 4.1.4.1 Example 1

Let us consider the first case where the target circuit parameters are: $L^*$=5.08nH, $C^*$=4.43pF, $L_c{}^*$=2.98nH, and $C_c{}^*$=4.06pF. By using the initial geometry module, the first layout of the structure has been inferred (see Table II for the geometrical parameters), the first Broyden matrix has been calculated as previously explained and the algorithm has evolved until convergence. Specifically, in this case, the algorithm has been forced to stop when the norm is smaller than 0.05 and it has been achieved after 15 iterations.

TABLE I COARSE PARAMETERS OF EXAMPLE 1

| | $x_c$ | | | |
|---|---|---|---|---|
| | $L$[nH] | $C$[pF] | $L_c$[nH] | $C_c$[pF] |
| **Target** | **5.08** | **4.43** | **2.98** | **4.08** |
| **Final** | **5.09** | **4.45** | **2.96** | **4.09** |

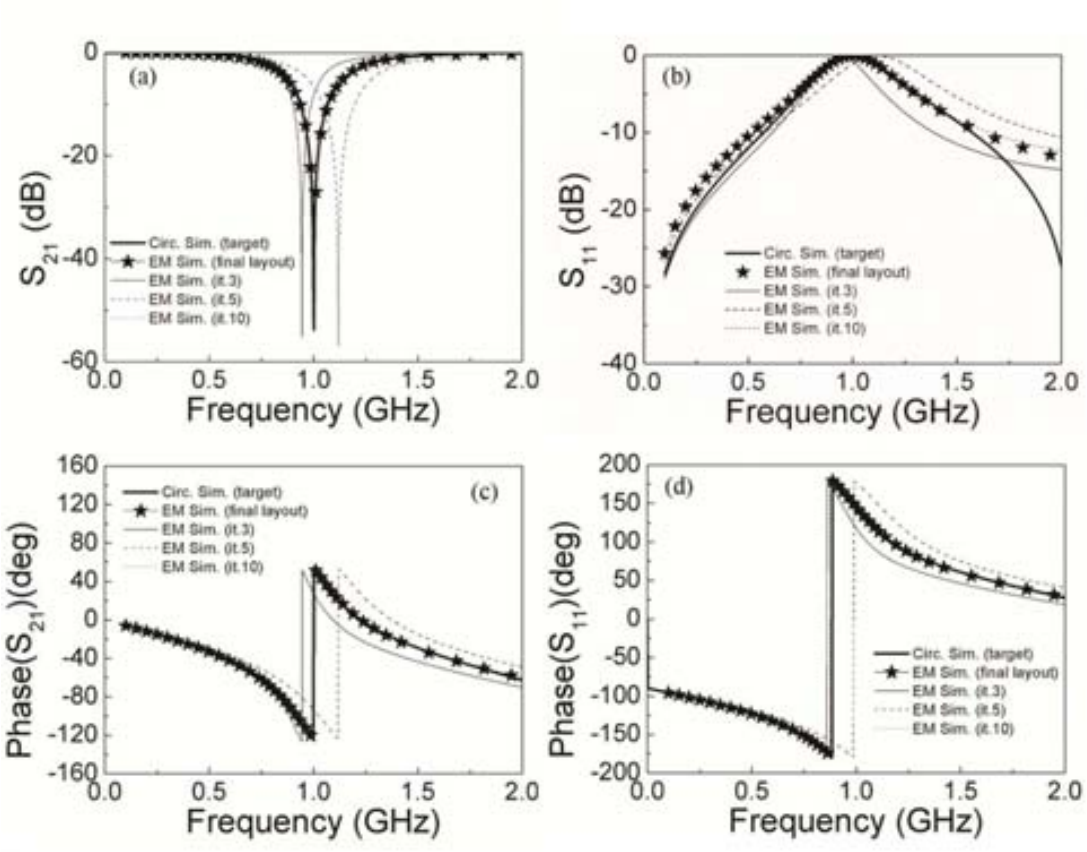


**Figure 4.2.** Target frequency response for the structure of example 1 and EM simulation at the indicated steps and after convergence. (a) Insertion losses; (b) return losses; (c) phase of S21; (d) phase of S11.

The circuit and geometrical parameters of initial and final structure are given in Table I and Table II, respectively. Notice that, the resulting circuit parameters (Table I) are very close to the target parameters. In Figure 4.2, the target frequency response, that is, the circuit simulation of the model of Figure 4.1(b) by considering the target circuit parameters, the EM simulation of final layout, and the EM simulation at iterations 3, 5 and 10 are depicted. As can be seen in Figure 4.2, there is a very good agreement between the EM simulation of the final solution and the target circuit simulation.

TABLE II FINE PARAMETERS OF EXAMPLE 1

| | $x_f$ | | | |
|---|---|---|---|---|
| | $r_{ext}$[mm] | $W$[mm] | $c$[mm] | $d$[mm] |
| **Initial** | **5.33** | **2.42** | **0.25** | **0.37** |
| **Final** | **5.60** | **5.08** | **0.26** | **0.25** |

The target circuit parameters of the current example were chosen according to those inferred from parameter extraction presented in [54] in order to validate the algorithm implementation. The geometrical dimensions of the generated CSRR-loaded line are slightly different than those of the structure of [54]. This is due to the sensitivity of the geometrical parameters. However, it has been demonstrated that it is possible to automatically synthetize a similar structure through the presented algorithm.

### 4.1.4.2 Example 2

For the second example, a set of target parameters in the coarse model have been chosen in order to obtain a desired frequency response. The set of circuit parameters are: $L^*$ = 6.00nH, $C^*$ = 1.815pF, $L_c^*$ = 2.00nH, and $C_c^*$ = 3.00pF and the resulting frequencies of interest are: $f_z$ = 1.622 GHz, $f_0$ = 2.055 GHz and $f_{-\pi/2}$ = 1.427 GHz. The algorithm has been applied in the same way than in the previous example, but in this case the norm of the error function has been set to be smaller than $\eta$ = 0.01. The convergence has been achieved after 30 iterations (the evolution of the norm evaluated by expression (4.11) is depicted in Figure 4.3, where it can be seen a global exponential decay showing a very good convergence rate, even though some small peaks due to the gradient-based iterative algorithm are present).

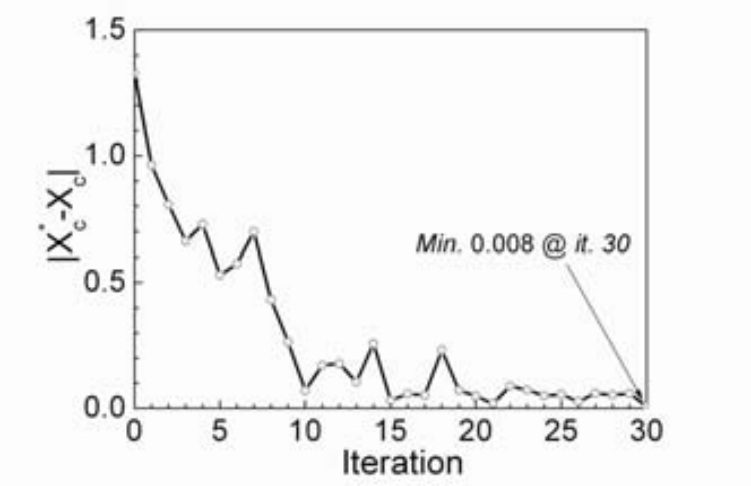


**Figure 4.3.** Evolution of the norm of the error function for the example considered.

The final dimension *s* of the structure are given in Table IV compared with the initial ones, whereas the resulting circuit parameters after convergence are given in Table III where it can be seen that they are very close to the target parameters.

TABLE III COARSE PARAMETERS OF EXAMPLE 1

| | $x_c$ | | | |
|---|---|---|---|---|
| | $L$[nH] | $C$[pF] | $L_c$[nH] | $C_c$[pF] |
| **Target** | **6.000** | **1.815** | **2.000** | **3.000** |
| **Final** | **6.001** | **1.821** | **2.004** | **2.997** |

TABLE IV FINE PARAMETERS OF EXAMPLE 1

| | $x_f$ | | | |
|---|---|---|---|---|
| | $r_{ext}$[mm] | $W$[mm] | $c$[mm] | $d$[mm] |
| **Initial** | **4.18** | **0.88** | **0.25** | **0.55** |
| **Final** | **4.61** | **2.25** | **0.25** | **0.56** |

The target frequency response, the EM simulation of final layout, and the EM simulation at iterations 3, 5 and 10 are depicted in Figure 4.4, where it can be appreciated that the intermediate responses progressively evolve to the final response.

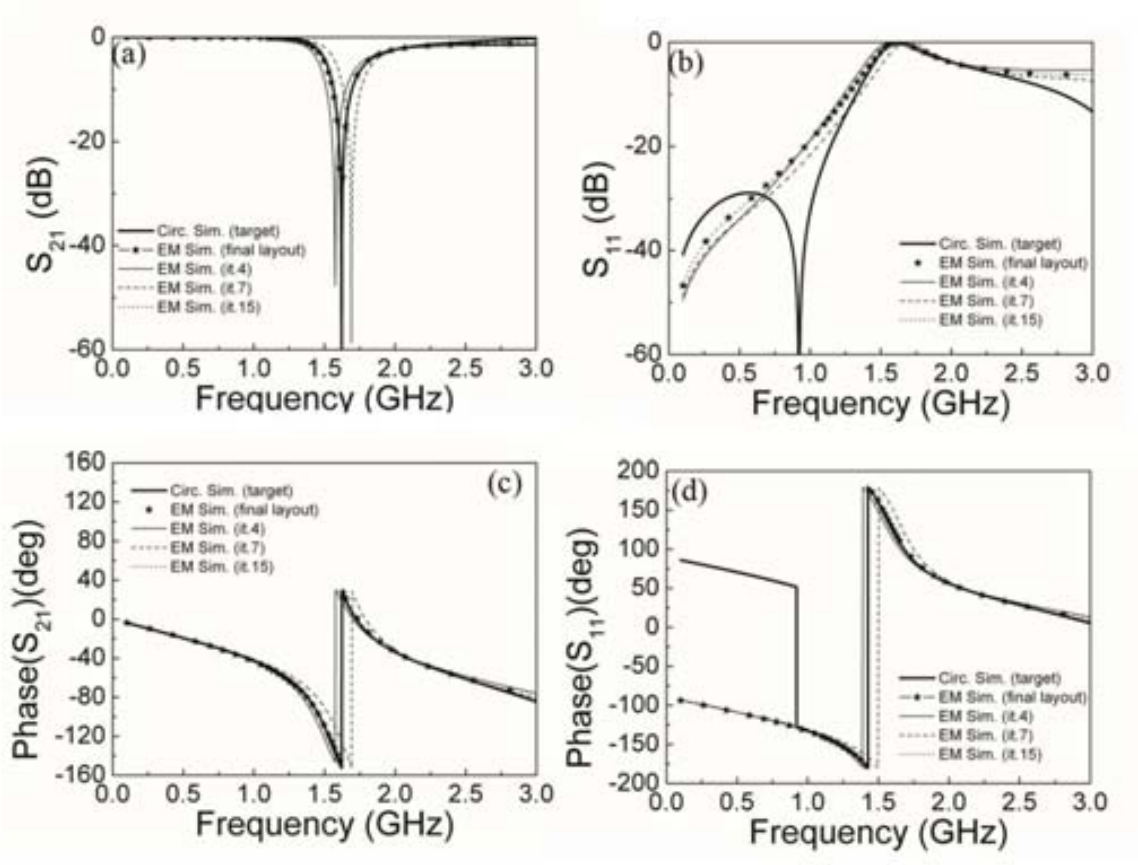


**Figure 4.4.** Target frequency response for the structure of example 2 and EM simulation at the indicated steps and after convergence. (a) Insertion losses; (b) return losses; (c) phase of S21; (d) phase of S11

As it can be observed in Figure 4.4, there is a disagreement in the low frequency region of $S_{11}$ that is caused by the fact that the image impedance of the cell corresponding to the target circuit parameters of this example varies very slightly in the vicinity of the port impedance (50Ω). Such impedance is exactly 50Ω at the reflection zero frequency, which is very sensitive to the variation of the circuit parameters. Since the parameter extraction is based on singular frequencies in the vicinity of the transmission zero frequency, it is not surprising that the EM simulation of the final layout might exhibit some deviation from the circuit model at lower frequencies. Nevertheless, in a linear scale the agreement is very good, and it is excellent in the region of interest. At higher frequencies, the discrepancies are due to the fact that the CSRR cannot be considered to be electrically small and the circuit model starts to fail.

## 4.2 CRLH microstrip cell based on CSRRs

This section is focused on the synthesis of CSRR-loaded microstrip CRLH lines. As previously mentioned in section 2.1.3, this kind of lines is useful in many applications that require tailoring their dispersion diagram, but its design is cumbersome and requires designer experience. For this reason, in this section, the application of ASM algorithm to the automated synthesis of CRLH microstrip lines loaded with CSRRs and

series gaps is demonstrated. The procedure is similar to the one presented in the previous section but the presence of the gap in such lines enhances the complexity of the ASM algorithm. The topology and circuit model of this kind of lines was explained in section 2.1.3 (see Figure 2.12). In this case, although eight geometrical parameters are necessary to define the layout of the structure of Figure 2.12(a) the same criteria as in the previous section has been used, therefore, the geometrical parameters considered in the optimization process (fine model variables) are reduced to five: $r_{ext}$, $c$, $d$, $W$ and $s$ (where the new variable $s$ corresponds to the gap separation). Concerning the coarse model, the five circuit parameters of the transformed T-model of CSRR-based CRLH transmission line [Figure 2.12(c)], $L$, $C$, $C_g$, $L_c$ and $C_c$ are the chosen set of design variables in $\boldsymbol{x_c}$.

In the following subsections, the main modules and the core program of the ASM algorithm for the CSRR-loaded CRLH microstrip unit cell will be compared with those presented in the previous section (in the case of negative effective permittivity based on CSRRs unit cell) highlighting the main differences. Moreover, a synthesis example of the considered structure will be shown in order to validate the implemented algorithm.

## 4.2.1 Initial geometry estimation

The initial geometry of the unit cell is found similarly to the previous case, by using the analytical model for a microstrip structure [29] and the CSRR model [35]. In contrast, the line capacitance is inferred from the value of $C_L$ from the transformed T-model of Figure 2.12(c). In order to obtain this value, the equations (2.48) and (2.49) are inverted, values of $C$ and $C_g$ are used and $C_s$ and $C_{par}$ are obtained. It is noteworthy that $C_{par}$ is typically dominated by the line capacitance $C_L$, therefore, we can neglect $C_f$ in a first order approximation, and consider $C_L$=$C_{par}$. With this value and the value of the line inductance, $L$, we can estimate the characteristic impedance of the host line (2.14) and, using equations (4.1)-(4.3) [29] we can infer the line width, $W$, proceeding in the same way as in the previous case. With the line width, $W$, the substrate parameters ($h$ and $\varepsilon_r$), and the value of $C_s$, we can determine the gap separation, $s$ by using the expression reported in [67]. Regarding the initial geometry of the CSRR, the same procedure as in the case of the negative effective structure is used, that is by using the equations reported in [35] and fixing the rings width $c$ in order to find a deterministic solution. Thus, the vector $\boldsymbol{x_f}^{(1)}$ has been obtained and is available for the core program of ASM algorithm.

## 4.2.2 EM solver

Concerning the EM solver module, a given vector in the fine model $\mathbf{x_f}^{(j)}$ is used to provide the frequency response in the same way that was explained before in section 4.1. The main difference is that, in this case, we have to define a gap in the strip line. To this

end, two rectangles are defined separated by a gap with distance *s*. The vertices of these rectangles describe the topology of the upper metal layer, the topology of the CSRR has been generated in the same way as in the case of negative effective permittivity unit cell since there is no variation in the topology of the lower metal layer.

### 4.2.3 Parameter extraction method

The main function of the parameter extraction module, as previously mentioned, is to obtain the circuit parameters of the model depicted in Figure 2.12(c) from the results of the EM solver module. In this case, four singular frequencies can be identified: (i) the transmission zero frequency, $f_z$, (ii) the resonance frequency of the CSRR, $f_0$, that is, the frequency at the intercept point of $S_{11}$ with the unit resistance circle in the Smith chart, (iii) the frequency where the phase shift of the unit cell is $-\pi/2$, $f_{-\pi/2}$ , and (iv) the resonance frequency of the series branch, $f_s$,

$$f_s = \frac{1}{2\pi\sqrt{LC_g}} \tag{4.12}$$

where $S_{11}$ intercepts the unit conductance circle in the Smith Chart. The frequencies $f_z$, $f_0$ and $f_{-\pi/2}$ are related to the circuit parameters through equations (4.5), (4.6), (4.7), respectively. Thus, we have four independent equations but considering the fact that at $f_0$ the shunt branch opens, the input impedance of the circuit model, $Z_{in}(f_o)$, can be written as:

$$Z_{in}(f_o) = Z_o + j\left(\frac{LC_g(2\pi f_o)^2 - 1}{C_g(2\pi f_o)}\right) \tag{4.13}$$

Therefore, we have the required equations (4.5)-(4.7), (4.12)-(4.13) to univocally infer the five parameters of the circuit model. Hence, the corresponding $\boldsymbol{x}_c$ vector is straightforwardly derived from EM solver results by using the presented module. In this case, the parameter extraction method is similar to the one described in [54], but in contrast, the value of $L$ is extracted rather than estimated.

### 4.2.4 Automated synthesis

The whole process of automated synthesis of a CSRR-based CRLH unit cell in microstrip technology will be compared with the automated synthesis of a negative effective permittivity unit cell. As previously mentioned, first of all, the initial geometry is determined, the EM frequency response is found and the circuit parameters are obtained by using the corresponding modules, and hence the error function **f** can be found. Notice that, in this case, an additional parameter has been added in contrast to the previous case, thus, the expression (4.9) is modified as follows:

$$\mathbf{f}(\mathbf{x_f}) = \mathbf{x_c^*} - \mathbf{x_c} = \left(L^* - L, \quad C^* - C, \quad C_g^* - C_g, \quad L_c^* - L_c, \quad C_c^* - C_c\right) \tag{4.14}$$

and the first Broyden matrix $\mathbf{B}^{(1)}$ is expressed as follows:

$$\begin{pmatrix} \frac{\delta L}{\delta W} & \frac{\delta L}{\delta r_{ext}} & \frac{\delta L}{\delta s} & \frac{\delta L}{\delta c} & \frac{\delta L}{\delta d} \\ \frac{\delta C}{\delta W} & \frac{\delta C}{\delta r_{ext}} & \frac{\delta C}{\delta s} & \frac{\delta C}{\delta c} & \frac{\delta C}{\delta d} \\ \frac{\delta C_g}{\delta W} & \frac{\delta C_g}{\delta r_{ext}} & \frac{\delta C_g}{\delta s} & \frac{\delta C_g}{\delta c} & \frac{\delta C_g}{\delta d} \\ \frac{\delta L_c}{\delta W} & \frac{\delta L_c}{\delta r_{ext}} & \frac{\delta L_c}{\delta s} & \frac{\delta L_c}{\delta c} & \frac{\delta L_c}{\delta d} \\ \frac{\delta C_c}{\delta W} & \frac{\delta C_c}{\delta r_{ext}} & \frac{\delta C_c}{\delta s} & \frac{\delta C_c}{\delta c} & \frac{\delta C_c}{\delta d} \end{pmatrix} \tag{4.15}$$

Once the initial Broyden matrix is known, the geometry of the next iteration is obtained, the new EM response is found and the circuit parameters are extracted, in the same way that in the subsection 4.1.4. In this case, the error function $\mathbf{f}(\boldsymbol{x}_f)$ is evaluated in the normalized form and its norm is defined as follows:

$$\left\|\mathbf{f}(\mathbf{x}_f)\right\| = \sqrt{\left(1-\frac{L}{L^*}\right)^2 + \left(1-\frac{C}{C^*}\right)^2 + \left(1-\frac{C_g}{C_g^*}\right)^2 + \left(1-\frac{L_c}{L_c^*}\right)^2 + \left(1-\frac{C_c}{C_c^*}\right)^2} \tag{4.16}$$

where the inductive and capacitive values are expressed in nH and pF, respectively. It is noteworthy that, this alternative form to evaluate the error function is applied due to the fact that the values of the circuit parameters may not be of the same order of magnitude. Specifically, the value of C is typically at least ten times greater than the value of the other parameters. The process is iterated as explained in section 2.2 until convergence is obtained. As mentioned before, the frequency interval must include the frequencies of interest in order to extract the circuit parameters, thus, in this case, the maximum considered frequency is set to $f_{max}$=1.8$f_s$, to cover beyond the frequency range where the circuit model of Figure 2.12(c) is valid.

In order to demonstrate the capabilities of the automatic synthesis of CSRR-based CRLH microstrip line, an application of the aforementioned ASM algorithm will be reported. The considered substrate is the commercial *Rogers RO3010* with thickness $h$ = 1.27 mm and dielectric constant $\varepsilon_r$ = 10.2.

In the example, the optimal coarse solution (target) is chosen to be equal to the one provided in [54] (see Table V) and the resulting frequencies of interest are: $f_z$ = 432 MHz, $f_0$ = 1.389 GHz and $f_s$ = 2.214 GHz.. The estimation of the first fine model vector,

$\boldsymbol{x}_f^{(1)}$, for the considered example by using the initial geometry estimation module are given in Table VI. Then, the ASM algorithm has been forced to stop when the norm of the normalized error function is smaller than $\eta = 0.04$ and it has been achieved after 25 iterations (it means a time around 90 minutes in a computer with Intel® Core™2 Quad CPU @ 2.83 GHz).

TABLE V COARSE PARAMETERS

| | $\boldsymbol{x}_c$ | | | | |
|---|---|---|---|---|---|
| | $L$[nH] | $C$[pF] | $C_g$[pF] | $L_c$[nH] | $C_c$[pF] |
| **Target** | **4.92** | **35.87** | **1.05** | **3.41** | **3.85** |
| **Final** | **4.94** | **36.98** | **1.05** | **3.44** | **3.83** |

TABLE VI FINE PARAMETERS

| | $\boldsymbol{x}_f$ | | | | |
|---|---|---|---|---|---|
| | $r_{ext}$[mm] | $W$[mm] | $s$[mm] | $c$[mm] | $d$[mm] |
| **Initial** | **5.46** | **1.14** | **0.11** | **0.25** | **0.33** |
| **Final** | **5.62** | **3.90** | **0.31** | **0.31** | **0.19** |

In Figure 4.5, it can be seen that the simulation results for the optimal coarse solution $\boldsymbol{x}_c^*$ and the final layout $\boldsymbol{x}_f^*$ exhibit a very good agreement. It must be noticed that the dimensions of the final solution (see Table VI) are very close to the ones published in [54].

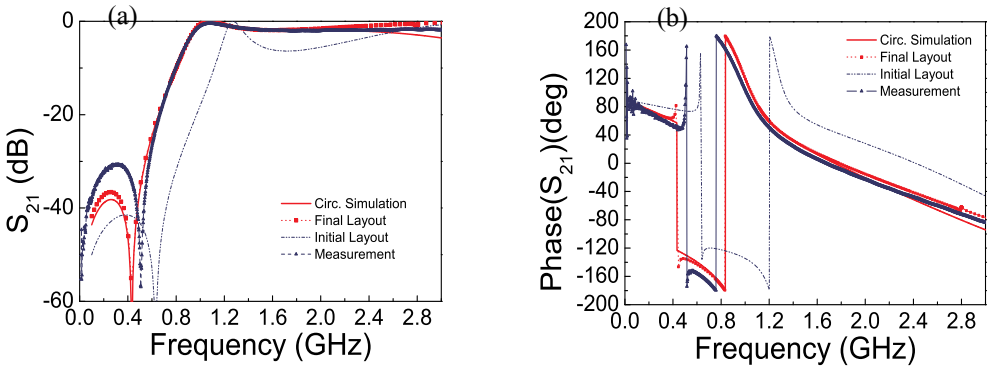


**Figure 4.5.** Magnitude (a) and phase (b) of the transmission coefficient at initial solution $\boldsymbol{x}_f^{(1)}$,, final solution $\boldsymbol{x}_f^*$, target response $\boldsymbol{x}_c^*$, and measurement.

# 4.3 Algorithm improvements

Although the automated synthesis of microstrip lines loaded with CSRRs (with and without series gaps) through ASM algorithms has been demonstrated, on the one hand, the implementable layouts of CSRR based lines are limited to certain combinations of the element values of the circuit model, since some values may lead to an unrealizable geometry. In spite of some efforts having made by means of parametric analysis [38],

there is not a systematic method to determine if an implementable geometry for a given set of circuit elements of the equivalent circuit model exists or not. On the other hand, one of the main drawbacks of the ASM algorithm is the determination of the initial layout. This estimation can lead the process to be very slow or a not converging algorithm. For these reasons, in the following subsections, the convergence region, as well as, a new method to obtain better initial geometry estimation will be presented [72].

The considered substrate is the *Rogers RO3010* substrate with dielectric constant $\varepsilon_r$ = 10.2 and thickness either $h$ = 1.27 mm or $h$ = 0.635 mm.

### 4.3.1 Convergence region

First of all, let us consider the case of negative effective permittivity lines loaded with CSRRs (or otherwise called CSRR-loaded metalines). As mentioned before, we have four geometrical variables in the fine model: $r_{ext}$, $W$, $c$, $d$, where the relation $l = 2r_{ext}$ is considered. Actually, in this case, the line length, $l$, is taken instead of the external radius of the CSRR, $r_{ext}$, as optimization variable in the fine model.

Given a set of circuit (target) variables, $L^*$, $C^*$, $L_c^*$ and $C_c^*$, a procedure to determine if this set of variables has a physically implementable layout is needed. According to the circuit model, $L^*$ and $C^*$ are physically realizable as long as these values are not too extreme and a microstrip line with reasonable width and length results. The key aspect is thus, given a pair of implementable values of $L^*$ and $C^*$, to determine the convergence region for the circuit values modeling the CSRR ($L_c$ and $C_c$). Thus, the strategy consists on calculating the line geometry that provides the element values $L^*$ and $C^*$ under four different scenarios corresponding to the extreme values of $c$ and $d$, namely, $c_{min}$-$d_{min}$, $c_{max}$-$d_{max}$, $c_{min}$-$d_{max}$, and $c_{max}$-$d_{min}$. The parameters $c_{min}$ and $d_{min}$ are the minimum achievable slot and strip widths, respectively, with the technology in use (we have set $c_{min} = d_{min}$ = 0.15 mm, unless otherwise specified). On the other hand, $c_{max}$ and $d_{max}$ are set to a reasonable (maximum) value that guarantees the validity of the model in the frequency region of interest. It has been found that for values exceeding 0.4-0.5 mm, the coupling between the slot rings is very limited and hence we have set $c_{max} = d_{max}$ = 0.4-0.5 mm (larger values expand the convergence region, but at the expense of less accuracy in the final solutions).

For each case, the single geometrical variables are $l$ and $W$ ($c$ and $d$ are fixed and $r_{ext} = l/2$). These variables must be optimized with the goal of recovering the $L$ and $C$ values corresponding to the target ($L^*$ and $C^*$). The extraction of the elements of the circuit model from the EM simulation is made by means of the parameter extraction method explained in subsection 4.1.3.

For the determination of $l$ and $W$, we do also consider an ASM optimization scheme, which is very simple since only two variables in each space are involved. The initial values of $l$ and $W$ are obtained from the characteristic impedance resulting from $L^*$ and $C^*$, by means of equations (4.1)-(4.4). With the resulting line geometry, we extract the parameters of the circuit model and also initialize the Broyden matrix (the initiation of the Broyden matrix follows a similar approach to that corresponding to the previously mentioned ASM algorithms, but in this case resulting in a 2 by 2 matrix). Then the process iterates until convergence is achieved. In this pre-optimization ASM process, the stopping criterion is usually tighter than the one considered for the full-ASM optimization, i.e. smaller values of the error functions are forced. This more restrictive criterion is chosen not only to accurately determine the vertices of the convergence region, but also to obtain a better estimate of the initial layout of the core ASM algorithm, as will be explained later.

Once the $l$ and $W$ values corresponding to the target $L^*$ and $C^*$ for a given $c$ and $d$ combination (for instance $c_{min}$-$d_{min}$) are found, the whole geometry is known, and the element values $L_c$ and $C_c$ can be obtained by means of the parameter extractor. These element values ($L_c$ and $C_c$) correspond to the considered CSRR geometry ($c_{min}$-$d_{min}$), and actually define the first vertex, $P_{c150d150}$, of the polygon which defines the convergence region, see Figure 4.6. Notice that the nomenclature used for identifying the vertices indicates (subscript) the values of $c$ and $d$ in microns.

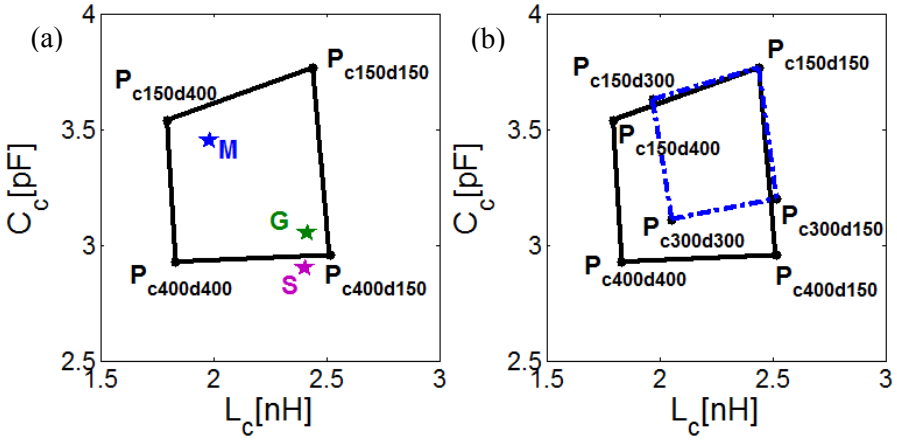


**Figure 4.6.** (a) Convergence region for a CSRR-loaded line model with $L^*$=4.86 nH and $C^*$=1.88 pF, defined by four points in the $L_c$-$C_c$ subspace, and considering $c_{min}$= $d_{min}$= 0.15 mm and $c_{max}$= $d_{max}$= 0.4 mm. (b) Various regions defined with different constraints for the same values of $L^*$ and $C^*$. The thickness of the substrate is $h$= 1.27mm.

Then, the same process is repeated for obtaining the next points, i.e, the $L_c$ and $C_c$ pairs corresponding to $c_{max}$-$d_{max}$, $c_{min}$-$d_{max}$, and $c_{max}$-$d_{min}$ with the target $L^*$ and $C^*$ (for these cases the initial values of $l$ and $W$ are set to the solutions of the previous vertex, since it provides a much better approaches to the optimal final solution). As a result, we obtain a set of points in the coarse model sub-space of $L_c$ and $C_c$ that defines a polygon (see Figure 4.6). This polygon is a rough estimate for the region of convergence in the

$L_c$-$C_c$ subspace, for the target values $L^*$ and $C^*$. The criterion to decide if the target element values can be physically implemented is the pertinence or not of the point (i.e. $L_c^*$, $C_c^*$) to the region enclosed by the polygon. It is possible to refine the convergence region by calculating more points, meaning further values/combinations of $c$ and $d$ (for instance those corresponding to a combination of an extreme and an intermediate value). Another approximation that can be done in order to shorten the pre-optimization process is to use as initial Broyden matrix **B** the one corresponding to the previous point solution. The effect is more relevant when the number of points to determine the region is bigger.

As a representative example of a CSRR-loaded line model, we have chosen $L^*$ = 4.86 nH and $C^*$ = 1.88 pF. The convergence region for the subspace $L_c$-$C_c$ calculated following the procedure explained above is depicted in Figure 4.6(a). Obviously, decreasing the maximum allowable value of $c_{max}$ and $d_{max}$ has the effect of reducing the area of the polygon, as Figure 4.6(b) illustrates. However, $c_{max}$ = $d_{max}$ = 0.4 mm is a reasonable value that represents a tradeoff between accuracy (related to the frequency responses of the fine and coarse models) and size of the convergence region.

Let us now consider the case of CSRR-loaded CRLH lines (or CSRR-gap-loaded metalines), where an additional variable is added, $C_g$ in the coarse model and gap space, $s$, in the fine model (see Figure 2.12). In this case, the convergence region can be obtained following a similar procedure, but now the target response is given by the electrical parameters that characterize the microstrip line with gap ($L^*$, $C^*$ and $C_g^*$). The pre-optimization ASM algorithm is thus more complex since it involves three variables, $l$, $W$ and $s$. As in the previous case, the initial layout for the first vertex is found analytically, similarly to the process described in subsection 4.2.1. Once the geometry of the line with gap is estimated, the electrical parameters are extracted according to the procedure given in subsection 4.2.3, the Broyden matrix is initiated, and the process is iterated until convergence is achieved. The result is a set of circuit model element values corresponding to the target elements of $L^*$, $C^*$ and $C_g^*$, and $L_c$ and $C_c$ values that depend on the considered CSRR geometry.

One differential aspect of CSRR-gap-loaded lines, as compared to CSRR-loaded lines, is the number of necessary points in the $L_c$-$C_c$ subspace to accurately determine the convergence region. It has been found that four points do not suffice in this case. Hence, the pre-optimization ASM algorithm has been applied eight times: four of them by considering the CSRR geometries with extreme values of $c$ and $d$; the other four cases by considering the following combinations: $c_{min}$-$d_{mean}$, $c_{max}$-$d_{mean}$, $c_{mean}$-$d_{max}$, and $c_{mean}$-$d_{min}$, where $d_{mean}$=($d_{min}$+ $d_{max}$)/2 and $c_{mean}$=($c_{min}$+ $c_{max}$)/2.

In some occasions, where a large gap capacitance is required, it is convenient to use a gap with T-shaped geometry (Figure 4.7). In this case, in order to preserve the number of variables in the validation space, the gap distance, $s$, is set to a small value (this helps to increase the series capacitance of the gap), and the gap width, $W_g$, is considered as the

geometry variable associated to the presence of the gap. Thus, the gap distance is set to $s$ = 0.2 mm (notice that $l_g$ –see Figure 4.7– is also set to $l_g$ = 0.2 mm to avoid an excess of variables). However, the pre-optimizer and core ASM algorithms do not experience any change by considering T-shaped gaps.

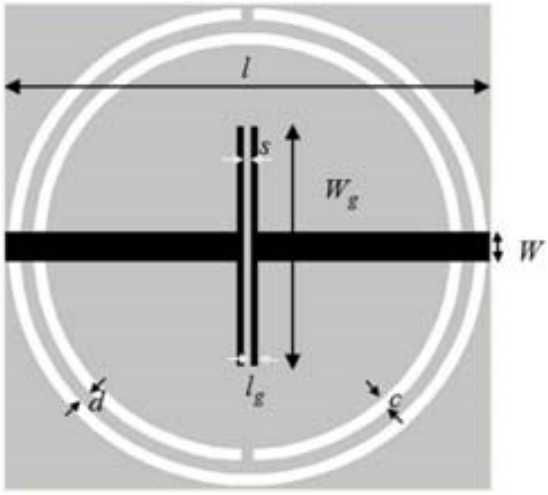


**Figure 4.7.** CSRR-based microstrip line with T-shaped gap.

In order to illustrate this pre-optimization ASM algorithm, a CSRR-gap-loaded line with T-shaped gap has been considered with the following target parameters in the coarse model: $L^*$ = 9.45 nH and $C^*$ = 17.93 pF and $C_g^*$ = 1.01 pF. The convergence region in the $L_c$-$C_c$ subspace is depicted in Figure 4.8 where it is clear that four points are not enough to determine the convergence region (notice that the $L_c$-$C_c$ points corresponding to the CSRR geometries given by $c_{min}$-$d_{mean}$, $c_{max}$-$d_{mean}$, $c_{mean}$-$d_{max}$, and $c_{mean}$-$d_{min}$ are significantly misaligned with the lines forming the polygon resulting by considering the four cases with extreme values of $c$ and $d$).

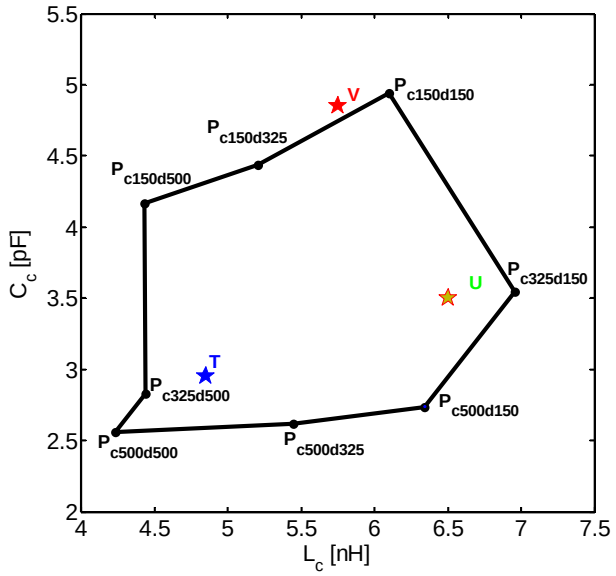


**Figure 4.8.** Convergence region for a CSRR-gap-loaded line model with $L^*$= 9.45 nH, $C^*$=17.93 pF, and $C_g^*$=1.01 pF, defined by eight points in the $L_c$-$C_c$ subspace, and considering $c_{min}$= $d_{min}$= 0.15 mm and $c_{max}$= $d_{max}$= 0.5 mm. The thickness of the substrate is $h$= 0.635mm.

### 4.3.2 New initial geometry estimation

Once the procedure to obtain the convergence region has been presented, the next step is the determination of the initial layout by using this. For a given set of circuit parameters of the circuit model for a CSRR-loaded metaline, and assuming that the previous analysis reveals that such target parameters in the coarse model space have an implementable fine model solution, it is expected that the dimensions of the CSRR after ASM optimization depend on the position of the $L_c^*$-$C_c^*$ point in the convergence region. Namely, if the $L_c^*$-$C_c^*$ point is close to a vertex, it is expected that $c$ and $d$ are similar to the values corresponding to that vertex (specifically, if $L_c^*$ and $C_c^*$ coincide with any of the vertices of the converging polygon in the $L_c$-$C_c$ subspace the layout is already known and hence no further optimization is necessary). Considering this, a new procedure to determine the initial layout is presented.

First of all, the case of CSRR-loaded lines is considered where the main aim of the procedure is to express any of the geometrical variables ($c$, $d$, $l$ or $W$) as a function of $L_c$ and $C_c$. To obtain the initial value of each geometrical dimension involved in the optimization process, we will assume it has a linear dependence with $L_c$ and $C_c$. For instance, the initial value of $c$ (for the other variables we will use identical expressions) will be estimated according to:

$$c = f(L_c, C_c) = (A + BL_c)(C + DC_c) \tag{4.17}$$

or alternatively:

$$c = f(L_c, C_c) = a_0 + a_1 L_c + a_2 C_c + a_3 L_c C_c \tag{4.18}$$

where the constants $a_i$ determine the functional dependence of the initial value of $c$ with $L_c$ and $C_c$. To determine the constants $a_i$, four conditions are needed. Let us consider the following error function:

$$f_{error} = \sum_{j=1}^{N_v} \left( c_j - f(L_{c_j}, C_{c_j}) \right)^2 \tag{4.19}$$

where the subscript $j$ is used to differentiate between the different vertices, and hence $c_j$ is the value of $c$ in the vertex $j$, and $L_{cj}$, $C_{cj}$ the corresponding values of $L_c$ and $C_c$ for that vertex. We have considered a number of vertices equal to four (corresponding to CSRR-loaded lines), but the formulation can be generalized to a higher number of vertices. Expression (4.19) can then be written as:

$$f_{error} = \sum_{j=1}^{4} c_j^2 - 2\sum_{j=1}^{4} c_j \cdot (a_0 + a_1 L_{c_j} + a_2 C_{c_j} + a_3 L_{c_j} C_{c_j}) + \\ + \sum_{j=1}^{4} (a_0 + a_1 L_{c_j} + a_2 C_{c_j} + a_3 L_{c_j} C_{c_j})^2 \tag{4.20}$$

To find the values of the constants $a_i$, we obtain the partial derivatives of the previous error function with regard to $a_i$, and force them to be equal to zero [73]:

$$\frac{\partial f_{error}}{\partial a_i} = -2\sum_{j=1}^{4} c_j \frac{\partial f(L_{c_j}, C_{c_j})}{\partial a_i} + 2\sum_{j=1}^{4}\left[ f(L_{c_j}, C_{c_j}) \frac{\partial f(L_{c_j}, C_{c_j})}{\partial a_i} \right] = 0 \tag{4.21}$$

for $i$ = 1, 2, 3, 4. Following this least-squares approach, four independent equations for the constants $a_i$ are obtained. Such equations can be written in matrix form as follows:

$$\begin{pmatrix} 4 & \sum_{j=1}^{4} L_{c_j} & \sum_{j=1}^{4} C_{c_j} & \sum_{j=1}^{4} L_{c_j} C_{c_j} \\ \sum_{j=1}^{4} L_{c_j} & \sum_{j=1}^{4} L_{c_j}^2 & \sum_{j=1}^{4} L_{c_j} C_{c_j} & \sum_{j=1}^{4} L_{c_j}^2 C_{c_j} \\ \sum_{j=1}^{4} C_{c_j} & \sum_{j=1}^{4} L_{c_j} C_{c_j} & \sum_{j=1}^{4} C_{c_j}^2 & \sum_{j=1}^{4} C_{c_j}^2 L_{c_j} \\ \sum_{j=1}^{4} L_{c_j} C_{c_j} & \sum_{j=1}^{4} L_{c_j}^2 C_{c_j} & \sum_{j=1}^{4} C_{c_j}^2 L_{c_j} & \sum_{j=1}^{4} C_{c_j}^2 L_{c_j}^2 \end{pmatrix} \begin{pmatrix} a_o \\ a_1 \\ a_2 \\ a_3 \end{pmatrix} = \begin{pmatrix} \sum_{j=1}^{4} c_j \\ \sum_{j=1}^{4} c_j L_{c_j} \\ \sum_{j=1}^{4} c_j C_{c_j} \\ \sum_{j=1}^{4} c_j L_{c_j} C_{c_j} \end{pmatrix} \tag{4.22}$$

Once the constants $a_i$ are obtained, the initial value of $c$ is inferred from (4.18). The process is repeated for the rest of geometrical parameters, and the initial geometry necessary for the initiation of the ASM algorithm is thus obtained.

In the case of CSRR-gap-loaded lines, a similar procedure is followed, although the number of vertices is higher (specifically, there are eight vertices rather than four, thus the index $j$ goes from 1 to 8). As compared to the initial geometry estimation previously explained in subsections 4.1.1 and 4.2.1, the procedure explained in this subsection leads to a geometry estimation very close to the final geometry, and this is fundamental to reduce the number of steps towards ASM convergence, as it will be shown later.

### 4.3.3 New Fast Two Step algorithm

Once convergence region determination and new initial geometry estimation have been presented, let us now consider a new fast two step ASM algorithm. It consists on a first step by means of the pre-optimization ASM algorithm and the determination of the initial fine vector, $\boldsymbol{x}_{em}^{(1)}$ (from now, the fine model vector will be denoted with sub-index *em*), described above and a second step by using a core ASM algorithm similarly that those proposed in section 4.1 and 4.2 for the CSRR-loaded and CSRR-gap-loaded metalines respectively. In this case, for the EM simulator two alternative options have been considered: the *Agilent Momentum* [74], as in the previous sections, and *Ansoft*

*Designer* [75]. Concerning the error function evaluation, the normalized form is used, thus, in the case of CSRR-loaded metalines is calculated according to:

$$\left\|\mathbf{f}(\mathbf{x}_f)\right\| = \sqrt{\left(1-\frac{L}{L^*}\right)^2+\left(1-\frac{C}{C^*}\right)^2+\left(1-\frac{L_c}{L_c^*}\right)^2+\left(1-\frac{C_c}{C_c^*}\right)^2} \qquad (4.23)$$

TABLE VII OPTIMAL COARSE SOLUTION

| | $x_c^*$ | | | |
|---|---|---|---|---|
| | $L$[nH] | $C$[pF] | $L_c$[nH] | $C_c$[pF] |
| S | 4.860 | 1.880 | 2.407 | 2.902 |
| G | 4.860 | 1.880 | 2.417 | 3.053 |
| M | 4.860 | 1.880 | 1.980 | 3.450 |

The main difference of the proposed ASM algorithm is the calculation of a very good initial geometry. First, we have applied the new ASM algorithm to the CSRR-loaded metalines whose optimal coarse parameters are detailed in Table VII, using *Ansoft Designer* as the EM-solver. In Figure 4.6(a) the location of these three different cases with respect to the shared convergence region (they have the same $L^*$ and $C^*$ values) is shown. Notice that in the case that the point is out of the convergence region but close to it, we let the algorithm to continue and change the limiting constrains of $c$ and $d$.

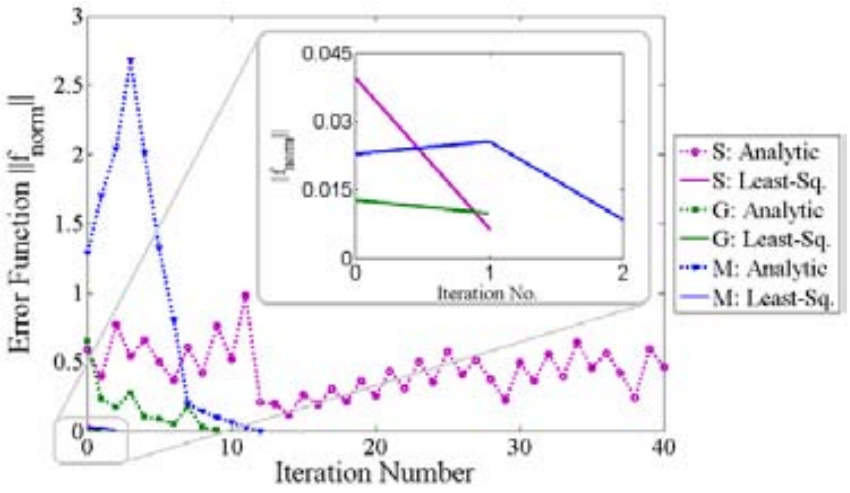


**Figure 4.9.** Evolution of the error function of the ASM algorithm for the points of Table VII. Dashed lines correspond to the evolution of the error function by considering the initial layout resulting from analytical expresssions; solid lines give the error function for the initial layout calculated from the least-squares approach proposed in this paper. M (blue), G (green) and S (pink) points.

The evolution of the error function with the iteration number is plotted in Figure 4.9, and compared to that of previously presented ASM algorithm. Convergence is much faster with the new ASM approach since the initial layout is closer to the final solution. It is noteworthy that there are points, like S, which do not converge to a final solution

with the previous ASM algorithm, whereas now convergence is obtained with the new approach. The number of iterations that needs the ASM algorithm to converge to the final layout dimensions and its corresponding evaluated error are summarized in Table VIII, for the three different examples considered ($\eta$ has been set to 0.01).

TABLE VIII FINE PARAMETERS FOR THE FINAL LAYOUT

| Case | $x_f$ | | | | Iter. num. | Error |
|---|---|---|---|---|---|---|
| | *l*[mm] | *W*[mm] | *c*[mm] | *d*[mm] | | $\|\|f_{norm}\|\|$ |
| *Analytic S* | 8.34 | 2.21 | 0.47 | 0.22 | 40 | 0.1192 |
| *Least-squares S* | 8.41 | 2.28 | 0.41 | 0.16 | 1 | 0.0066 |
| *Analytic G* | 8.44 | 2.23 | 0.35 | 0.17 | 9 | 0.0057 |
| *Least-squares G* | 8.47 | 2.22 | 0.36 | 0.17 | 1 | 0.0098 |
| *Analytic M* | 8.56 | 2.21 | 0.18 | 0.32 | 12 | 0.0038 |
| *Least-squares M* | 8.59 | 2.20 | 0.18 | 0.33 | 2 | 0.0084 |

substrate thickness $h$ = 1.27 mm

The final layout obtained for the first example (S) is slightly out of the lower boundary ($c$= 0.41 mm), as it was expected since the target S was placed out of the convergence region [see Figure 4.6(a)]. However, we have let the algorithm to continue towards convergence by relaxing the limiting values of $c$ and $d$. Thus, the fact that the target is out of the convergence region does not necessarily mean that convergence is not possible, but that the resulting geometric values might be beyond or below the considering limits of $c$ and $d$. For the S point, the close proximity to the line of the polygon corresponding to $c$=0.40 mm (Figure 4.6) explains that the final value of $c$ is 0.41mm. The agreement between the frequency response obtained by EM simulation of the final layout (obtained after a single iteration) and the circuit simulation of the target parameters is excellent, as it can be seen in Figure 4.10. This is reasonable since the value of $c$ is not far from the considering limiting value that guarantees that the CSRRs are accurately described by the models depicted in Figure 4.1.

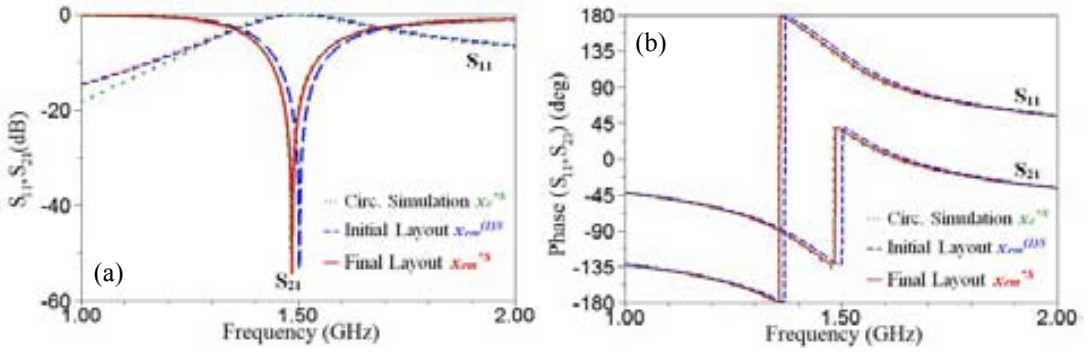


**Figure 4.10.** Magnitude (a) and phase (b) of the scattering parameters $S_{21}$ and $S_{11}$ at initial solution $x_{em}^{(1)}$, $x_{em}^{*}$, and circuital simulation of the $x_c^{*}$ for point S.

In Figure 4.11 the comparison of the frequency responses corresponding to the point G, is depicted where very good agreement between circuit simulation (target coarse parameters) and EM simulation of the final layout results.

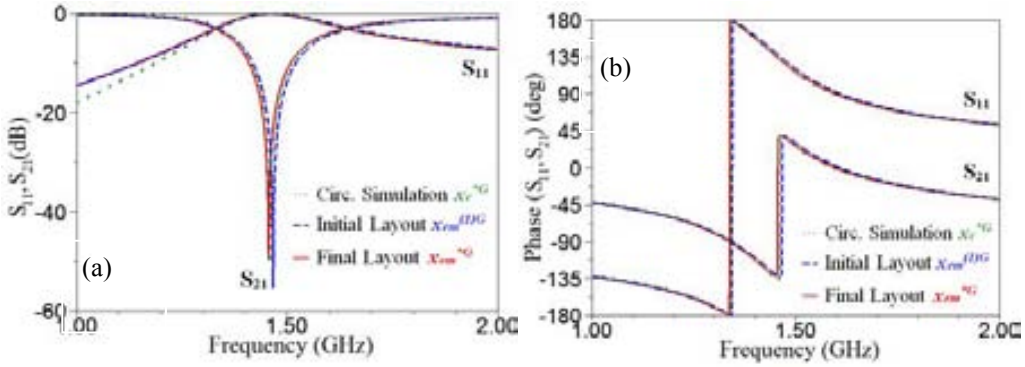


**Figure 4.11.** Magnitude (a) and phase (b) of the scattering parameters $S_{21}$ and $S_{11}$ at initial solution $x_{em}^{(1)}$, $x_{em}^{*}$, and circuital simulation of the $x_c^{*}$ for point G.

In order to illustrate the new two-step ASM algorithm applied to the case of CSRR-gap (T-shaped) loaded metalines, the targets indicated in Figure 4.8 and given in Table IX have been synthetized. The resulting geometrical values, as well as the error function with the required iteration number are given in Table X. In this case, the algorithm has been forced to stop when the normalized error function is smaller than $\eta = 0.04$ and although it is higher than in the previous examples, it is still providing very accurate results. Concerning the EM-solver, *Agilent Momentum* has been considered in this occasion. The frequency response for the initial and final layout, as well as the circuit simulation of the target parameters for the point T is depicted in Figure 4.12. The evolution of the error function for the present case can not be compared with those by using the previous version of the ASM algorithm because this was not adapted for T-shaped gaps. Thus, the convergence curves are not provided. Nevertheless, convergence speed is good (few iterations suffice to obtain a small error function), although not so fast, as compared to the CSRR-loaded structures without gap (Figure 4.9).

TABLE IX OPTIMAL COARSE PARAMETERS

| | $x_c^{*}$ | | | | |
|---|---|---|---|---|---|
| | $L$[nH] | $C$[pF] | $C_g$[pF] | $L_c$[nH] | $C_c$[pF] |
| T | 9.45 | 17.93 | 1.01 | 4.85 | 2.95 |
| U | 9.45 | 17.93 | 1.01 | 6.50 | 3.50 |
| V | 9.45 | 17.93 | 1.01 | 5.75 | 4.85 |

TABLE X FINE PARAMETERS FOR THE FINAL LAYOUT

| Case | $x_f$ | | | | | Iter. num. | Error |
|---|---|---|---|---|---|---|---|
| | $l$[mm] | $W$[mm] | $c$[mm] | $d$[mm] | $W_g$[mm] | | $\|\|f_{norm}\|\|$ |
| T | 14.2 | 0.87 | 0.34 | 0.40 | 7.13 | 6 | 0.0124 |
| U | 15.7 | 0.68 | 0.33 | 0.16 | 6.61 | 13 | 0.0292 |
| V | 17.1 | 0.56 | 0.13 | 0.21 | 6.07 | 13 | 0.0386 |

substrate thickness $h = 0.635$ mm

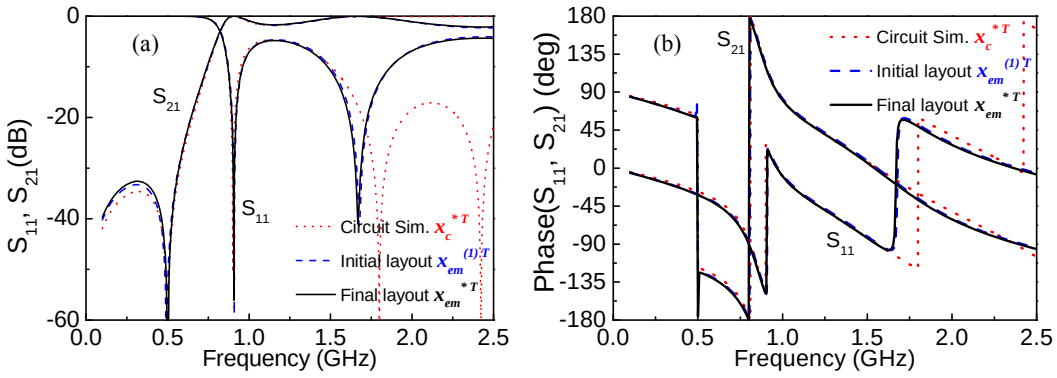


**Figure 4.12.** Magnitude (a) and phase (b) of the scattering parameters $S_{21}$ and $S_{11}$ at initial solution $x_{em}^{(1)}$, $x_{em}^{*}$, and circuital simulation of the $x_c^{*}$ for point T.

---

In **summary**, the automated synthesis of circuits based on CSRRs by means of ASM algorithms has been introduced in this chapter. Specifically, the synthesis of CSRR-loaded lines with and without series gaps has been considered. On the one hand, the main constitutive modules of the algorithm and the whole process have been explained in detail, by contrasting the main differences for each case. On the other hand, the algorithm improvements have been shown, presenting a new fast two step ASM algorithm.

# 5

# ASM algorithms applied to the design of microwave devices



The automated synthesis of CSRR-based unit cells through ASM has been demonstrated in the previous chapter. The main aim of the present chapter is to illustrate the potentially of applying this automatic process to the design of microwave devices based on such cells. On the one hand, the design process of a stop band filter in the Wi-Fi band formed by several CSRR-loaded negative effective permittivity unit cells synthesized by means of ASM algorithm will be shown. On the other hand, the application of ASM algorithm to the design of a dual-band power divider in the GSM band based on a CSRR-loaded CRLH unit cell will be presented. In both cases, the ASM algorithm allows us to semi-automate the design process, as the main cell is synthesized automatically.

# 5.1 ASM applied to the design of stop band filters based on negative effective permittivity cells

The application examples of a new fast two step ASM algorithm for the negative effective permittivity unit cells have been presented in previous chapter (see Table VIII) and can be considered as notch filters. In this section we go one step further: the implementation of stop-band filters with controllable response by using CSRR-loaded lines without gaps automatically synthetized through the new version of the ASM algorithm [72]. Compact planar stop-band filters can be designed by cascading several CSRR-loaded line unit cells. Let us illustrate this possibility through the design procedure and experimental verification of a three unit cell stop-band filter in microstrip technology.

The first step consists on the synthesis of the central unit cell, whose transmission zero frequency, $f_z$, is chosen to be the central frequency of the stop-band. We have chosen to reject the Wi-Fi band, and for this reason, this frequency has been set to 2.45GHz. The other cells involved in the design will have similar target responses, and very close transmission zero frequencies (i.e. 2.36 GHz and 2.53 GHz), the optimal coarse solutions for all the involved cells were forced to be placed in the same convergence region (i.e. with the same $L$ and $C$ values, as it is seen in Table XI) in order to speed up the design process. By cascading the three cells with the circuit elements indicated in Table XI, a satisfactory stop-band response at the circuit simulation level results. By using the ASM algorithm described in section 4.3, and considering the *Rogers RO3010* substrate with thickness $h$=1.27 mm and dielectric constant $\varepsilon_r$=10.2 three layouts have been obtained. The geometries of these synthesized unit cells as well as the number of required iterations and the norm of the error function in the second step of the algorithm are summarized in Table XII.

TABLE XI OPTIMAL COARSE SOLUTION OF UNIT CELLS

| Cell | $x_c^*$ | | | |
|---|---|---|---|---|
| | $L$[nH] | $C$[pF] | $L_c$[nH] | $C_c$[pF] |
| $C_{2.36}$ | 3.194 | 1.363 | 1.009 | 3.143 |
| $C_{2.45}$ | 3.194 | 1.363 | 0.941 | 3.120 |
| $C_{2.53}$ | 3.194 | 1.363 | 0.882 | 3.125 |

TABLE XII SYNTHESISED LAYOUTS FOR THE DIFFERENT UNIT CELLS

| Cell ($f_z$) | $x_f$ | | | | Iter. num. | Error |
|---|---|---|---|---|---|---|
| | $l$[mm] | $W$[mm] | $c$[mm] | $d$[mm] | | $\|\|\mathbf{f}_{norm}\|\|$ |
| 2.36 GHz | 5.93 | 2.16 | 0.28 | 0.25 | 3 | 0.0074 |
| 2.45 GHz | 5.91 | 2.23 | 0.34 | 0.27 | 1 | 0.0055 |
| 2.53 GHz | 5.93 | 2.25 | 0.34 | 0.33 | 5 | 0.0069 |

The next step could be to cascade the three designed cells to obtain the stop-band filter, as has been done at the circuit level or in [76]. However, coupling effects between the CSRRs can appear as occurs in this case (verified through EM simulation). Therefore, it is necessary to insert transmission line sections between the synthesized unit cells, as depicted in Figure 5.1 and Figure 5.2. The length of the transmission line sections between adjacent CSRRs has been set to 3/4 the CSRR radius (the width being identical to that of the microstrip on top of the CSRR, indicated in Table XII). With these transmission line lengths, coupling effects between adjacent CSRRs are not present, while the circuit response does not substantially change as compared to the case with direct connection between unit cells at the circuit level.

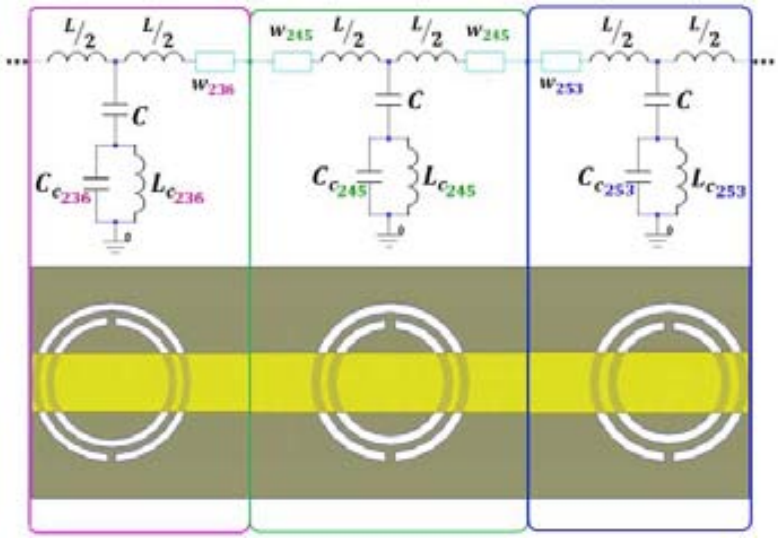


**Figure 5.1.** Equivalent circuit and layout of the implemented stop-band filter. The small blue rectangles correspond to lines of physical length equal to 2.22mm and width according to the value for each unit cell (see Table XII).

The completed manufactured stop-band filter can be seen in Figure 5.2, where tapers between the input/output 50 Ω transmission lines (needed to perform the measurements) and the designed structure are included. It was fabricated by using the circuit board plotter *LPKF ProMat S103*.


**Figure 5.2.** Photograph of the fabricated CSRR-based stop-band filter.

The measured filter response, displayed in Figure 5.3, is compared with the equivalent circuit and full-wave electromagnetic simulated responses. The measured rejection is better than 20dB within a 345MHz frequency band. The agreement between circuit and EM simulation is very good, as expected on account of the small errors that appear in Table XII. The small discrepancies in measurement and the additional reflection zero are attributed to fabrication related tolerances.

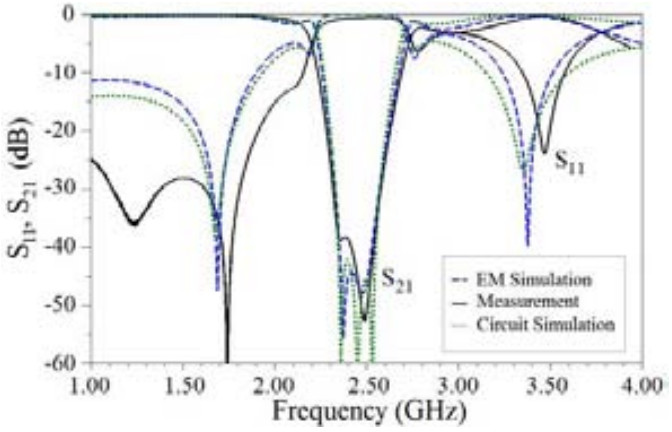


**Figure 5.3.** Frequency response of the stop-band filter: the target response (i.e., that corresponding to the equivalent circuit simulation) is depicted in green-dotted line, the full-wave EM simulation in blue-dashed line, and the measurements in black-solid lines.

## 5.2 ASM applied to the design of dual band power dividers based on CRLH cells

Let us now consider the application of the proposed two-step ASM algorithm to the synthesis of a dual-band power splitter based on a dual-band impedance inverter implemented by means of the CSRR-gap-loaded line. To achieve the dual-band functionality, the inverter must provide a phase shift of $-90^o$ and $+90^o$ at the operating frequencies, $f_1$ and $f_2$, respectively. We are thus exploiting the composite right/left handed behavior of the structure, with $f_1$ and $f_2$ located in the left handed and right handed regions, respectively (see [13]). The inverter impedance is set to 35.35Ω at both frequencies, in order to guarantee a good matching when the inverter output port is loaded with a pair of matched loads (in practice two 50Ω access lines) to implement the divider. Notice that these four conditions do not univocally determine the five circuit elements of the model of the CSRR-gap loaded line [Figure 2.12(c)]. However, we can set the transmission zero [see equation (4.5)] to a certain value, and the five parameters thus have a unique solution. Specifically, the design frequencies of the inverter have been set to $f_1$ = 0.9 GHz and $f_2$=1.8 GHz (to be used in GSM-900 and GSM-1800 bands) and the transmission zero to $f_z$ = 0.5 GHz.

Since the phase shift is ±90º and the characteristic impedance of the inverter is the same at both frequencies, we can infer from (2.6) and (2.7) the following system of equations:

$$Z_s(\omega_1) = jZ_0 \tag{5.1}$$

$$Z_p(\omega_1) = -jZ_0 \tag{5.2}$$

$$Z_s(\omega_2) = -jZ_0 \tag{5.3}$$

$$Z_p(\omega_2) = jZ_0 \tag{5.4}$$

where $\omega_1=2\pi f_1$ and $\omega_2=2\pi f_2$. And by adding the equation (4.5) the five element values can be expressed as follows:

$$L = \frac{2Z_0}{\omega_2 - \omega_1} \tag{5.5}$$

$$C_g = \frac{1}{2}\frac{\omega_2 - \omega_1}{\omega_1\omega_2 Z_0} \tag{5.6}$$

$$C = \frac{\left(\omega_z^2 - \omega_2^2\right)\omega_1^2 - \omega_1\omega_2\omega_z^2 + \omega_2^2\omega_z^2}{\omega_1\omega_2\omega_z^2 Z_0\left(\omega_1 - \omega_2\right)} \tag{5.7}$$

$$C_c = \frac{\left(\omega_1^2\left(\omega_2^2 - \omega_z^2\right) + \omega_1\omega_2\omega_z^2 - \omega_2^2\omega_z^2\right)\left(\omega_1\omega_2 - \omega_z^2\right)}{\left(\omega_2^2 - \omega_z^2\right)\left(\omega_1^2 - \omega_z^2\right)\left(\omega_2 - \omega_1\right)\omega_1\omega_2 Z_0} \tag{5.8}$$

$$L_c = \frac{\left(\omega_2^2 - \omega_z^2\right)\left(\omega_1^2 - \omega_z^2\right)\left(\omega_2 - \omega_1\right)\omega_1\omega_2 Z_0}{\left(\omega_2^2\left(\omega_1^2 - \omega_z^2\right) + \omega_1\omega_2\omega_z^2 - \omega_1^2\omega_z^2\right)^2} \tag{5.9}$$

With the previous specifications, the resulting element values are $L$ = 12.5 nH, $C$=24.9 pF, $C_g$ =1.25 pF, $L_c$ = 3.38 nH and $C_c$ = 5.10 pF. With the element values of $L$, $C$ and $C_g$, we have obtained the convergence region in the $L_c$-$C_c$ plane according to the method reported in section 4.3, and the target values of $L_c$ and $C_c$ do not belong to such region. This means that it is not possible to implement the dual-band impedance inverter by merely considering the CSRR-gap-loaded line (some element values are too extreme). However, it is expected that by cascading transmission line sections at both sides of the CSRR-gap loaded line, the element values of the cell are relaxed, and a solution within the convergence region arises. Therefore, we have cascaded two identical 35.35Ω transmission line sections at both sides of the CSRR-gap loaded line. The width of these line sections is 1.127 mm, corresponding to the indicated characteristic impedance in the considered substrate (the *Rogers RO3010*, with thickness $h$= 0.635 mm and

dielectric constant $\varepsilon_r$ =10.2). Notice that by cascading such 35.35Ω lines, the electrical length at the operating frequencies is the sum of the electrical lengths of the lines and the CSRR-based cell. Thus, the phase condition that must satisfy the CSRR-gap loaded line can be expressed as $\phi_1 = -90^o - 2\phi_L(f_1)$ and $\phi_2 = +90^o - 2\phi_L(f_2)$, where $\phi_1$ and $\phi_2$ are the electrical lengths of the CSRR-based cell at the design frequencies $f_1$ and $f_2$, and $\phi_L$ is the phase introduced by the line at the indicated frequency. Therefore, the phase shift of the unit cell is different to ±90º, and the equations (5.1)-(5.4) are not valid, thus the generic form of these equations has to be taken in account:

$$Z_s(\omega_1) = j\frac{Z_0(\cos(\phi_1)-1)}{\sqrt{1-\cos^2(\phi_1)}} \tag{5.10}$$

$$Z_p(\omega_1) = -j\frac{Z_0}{\sqrt{1-\cos^2(\phi_1)}} \tag{5.11}$$

$$Z_s(\omega_2) = -j\frac{Z_0(\cos(\phi_2)-1)}{\sqrt{1-\cos^2(\phi_2)}} \tag{5.12}$$

$$Z_p(\omega_2) = j\frac{Z_0}{\sqrt{1-\cos^2(\phi_2)}} \tag{5.13}$$

We have made a parametric analysis consisting on obtaining the element values of the CSRR-based cell for different values of the length of the cascaded transmission line sections (and hence $\phi_L(f_1)$ and $\phi_L(f_2)$). The results are depicted in Figure 5.4. It can be observed that for small values of $\phi_L(f_1)$, $L$ and $C$ are too large for being implemented. Large $L$ means a small value of $W$, but this is not compatible with a large $C$ value. On the other hand, the values of $L_c$ and $C_c$ without cascaded line sections, i.e., $\phi_L(f_1)=0^o$, give extreme values of $d$ and $c$, that is, large value of $d$ and small value of $c$. However, by increasing $\phi_L(f_1)$ (or the length of the cascaded lines), the variation of the elements of the central CSRR-gap based cell goes in the correct direction for their implementation. Specifically, we have considered a pair of transmission line sections with $\phi_L(f_1)=15^o$, which means that the required electrical lengths for the CSRR-based cell at the operating frequencies are $\phi_1 = -120^o$ and $\phi_2 = +30^o$. The element values corresponding to these phases are $L$ = 9.45 nH and $C$ = 17.9 pF, $C_g$ =1.01 pF, $L_c$ =4.85 nH and $C_c$ = 2.95 pF, and these values lead us to an implementable layout. The reason is that this phase shift gives the minimum value of $L$ (see Figure 5.4) and a reasonable small value of $C$, with $L_c$ not so small and $C_c$ no so large. Notice that $C_g$ does not experience significant variations with $\phi_L(f_1)$.

We have applied the proposed two-step ASM algorithm to the previous element values, and we have synthesized the layout of the CSRR-gap-loaded line, considering a T-shaped geometry for the gap. The geometrical parameters of the synthesized structure

are (in reference to Figure 4.7) $l$= 14.42 mm, $W$= 0.87 mm, $c$= 0.34 mm, $d$= 0.40 mm, $W_g$= 7.13 mm, and convergence (with an error of 0.012) has been obtained after 6 iterations.

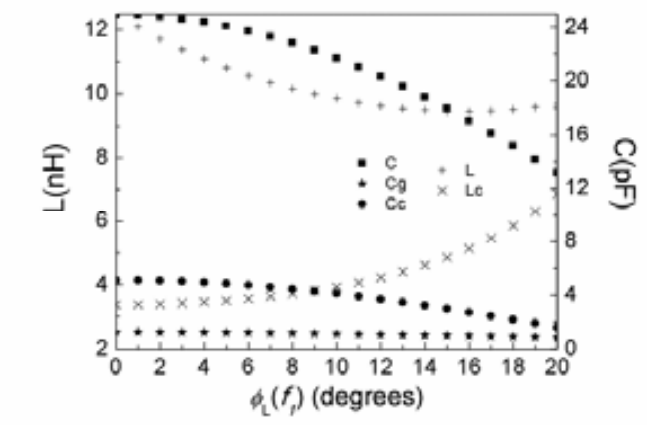


**Figure 5.4.** Dependence of the element values of the CSRR-gap loaded line with the phase of each cascaded transmission line section at $f_1$.

The comparison of the electrical length and characteristic impedance inferred from EM simulation of the synthesized impedance inverter (the CSRR-based cell plus the cascaded 35.35Ω transmission line sections) and the ones inferred from circuit simulation are shown in Figure 5.5. The agreement is excellent in the left handed region, where the model describes the structure to a very good approximation, and progressively degrades as frequency increases, as it is well known and expected. Nevertheless, the phase shift and the characteristic impedance at $f_2$ are reasonably close to the nominal values, and hence we do expect that the functionality of the power divider at $f_2$ is preserved.

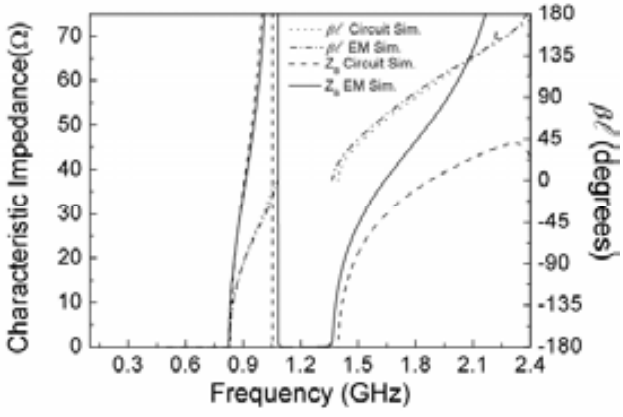


**Figure 5.5.** Comparison between the electromagnetic and circuit simulation corresponding to the characteristic impedance and electrical length of the designed dual-band impedance inverter.

We have cascaded two output 50Ω access lines for connector soldering, and the structure has been fabricated by means of a photo/mask etching process (Figure 5.6). Figure 5.7 shows the frequency response of the divider, where it can be appreciated that

optimum matching occurs at $f_1$ and slightly below $f_2$, for the reasons explained. Nevertheless, the functionality of the power divider covers both design frequencies. The discrepancy between the measured response and the target is not due to a failure of the ASM algorithm, but to the fact that the circuit model of the CSRR-gap loaded line does not accurately describe the structure at high frequencies, including part of the right handed band. A more accurate model increases the complexity of the ASM algorithm.

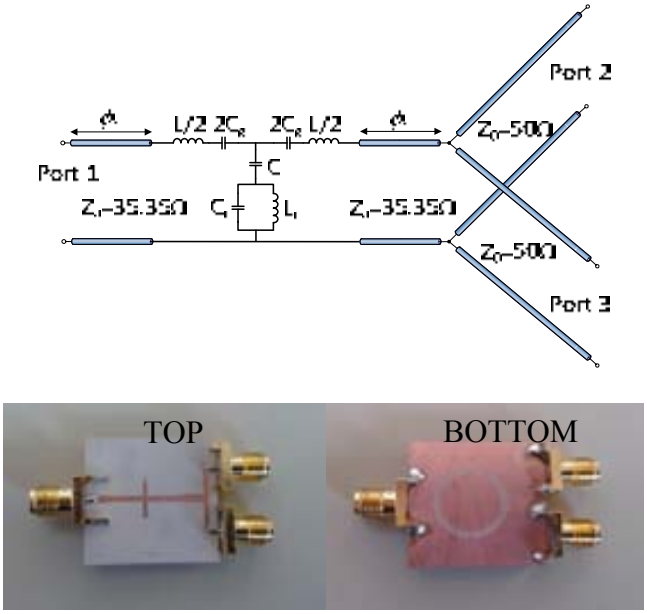


**Figure 5.6.** Schematic and photograph of the fabricated dual-band power divider.

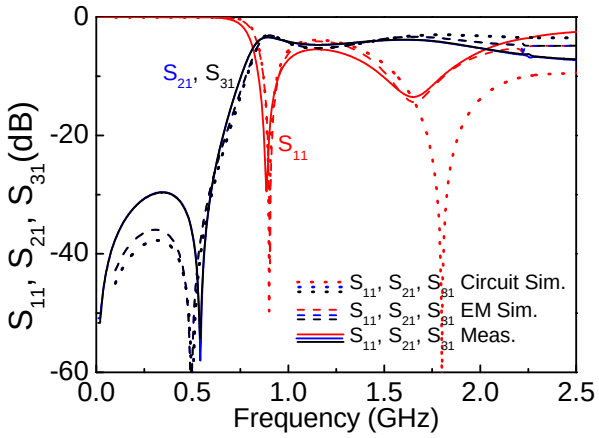


**Figure 5.7.** Frequency response (circuit and electromagnetic simulation and measurement) of the designed and fabricated dual-band power divider.

---

In **summary**, two applications of the new two-step ASM algorithm to the synthesis of CSRR-based devices have been presented. First, a stop-band filter formed by three CSRR-loaded unit cells without gaps automatically synthetized through the

aforementioned algorithm has been illustrated. Second, the tool has been applied to the design of a dual-band power divider and the pre-optimization step has revealed that the considered target values are not implementable. Nevertheless, with the addition of two transmission line sections, these element values have been relaxed and the device has been designed. Finally, both examples have been fabricated and good agreement between simulations and measurements has been found.

# 6

# ASM applied to other microwave devices



In previous chapters, the application of the ASM algorithm has been focused on microwaves structures based on metamaterials. In contrast, in this chapter the aforementioned optimization technique based on ASM is applied to other microwave structures. Specifically, the synthesis of Stepped Impedance Resonators (SIR) and planar inductors in microstrip technology through ASM is presented. In the first section, the optimization is focused on the Stepped Impedance Shunt Stub (SISS). The topology and the equivalent circuit model of this structure are analyzed and an ASM algorithm is developed in order to automatically synthesize this kind of structure. Furthermore, to illustrate the potential of this technique, an order-3 elliptic low pass filter has been designed. In the second section, synthesis of RF/microwave planar inductors by means of ASM algorithm is presented. One turn spiral inductor is considered as a first approach. Thus, the structure has been analyzed and the optimization algorithm has been applied.

# 6.1 ASM applied to SIR structures

Stepped Impedance Resonators (SIRs) are useful for the design of planar microwave components such as filters and diplexers [77, 78]. Their size can be reduced by enhancing the impedance ratio of the resonator [77, 78]. In many applications, SIRs are used in shunt connection, loading a microstrip transmission line, where there is a narrow strip that exhibits high impedance, and a wide strip that acts as a grounded capacitor (low impedance). Figure 6.1 shows a typical topology that is known as Stepped Impedance Shunt Stub (SISS), and behaves as a shunt connected series LC resonator in microstrip technology. However, this structure has limitations concerning the implementable values of the LC resonator in a wide range of frequencies and to achieve geometrical dimensions from the values of the circuit model. The first limitation was considered in [79] and we use this study to know if the desired values are implementable and to obtain the initial geometry. To solve the second aspect we need optimization since the available formulas that provide SISS dimensions from the values of the LC resonator are not accurate. The aim of this section is to demonstrate that it is possible to automatically generate a SISS layout for a given set of implementable values using an ASM algorithm.

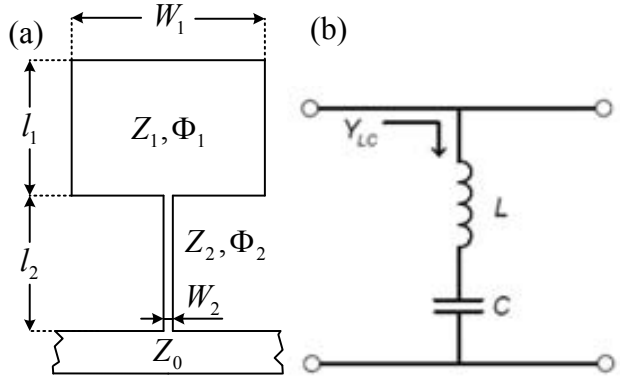


**Figure 6.1.** Topology of the SISS in microstrip technology and relevant dimensions (a) and equivalent circuit model (b).

## 6.1.1 Analysis of the SISS

The admittance of the SISS (seen from the host line) is:

$$Y_{SISS} = -j\frac{\tan \Phi_1 + K \tan \Phi_2}{Z_2 \tan \Phi_1 \tan \Phi_2 - Z_1} \tag{6.1}$$

where $\Phi_1$ and $\Phi_2$ are the electrical lengths of the low and high impedance line sections respectively, and

$$K = \frac{Z_1}{Z_2} \tag{6.2}$$

is the impedance ratio of the SISS [77]. At resonance, the denominator in (6.1) vanishes, and the following condition results:

$$K = \tan \Phi_1 \cdot \tan \Phi_2 \tag{6.3}$$

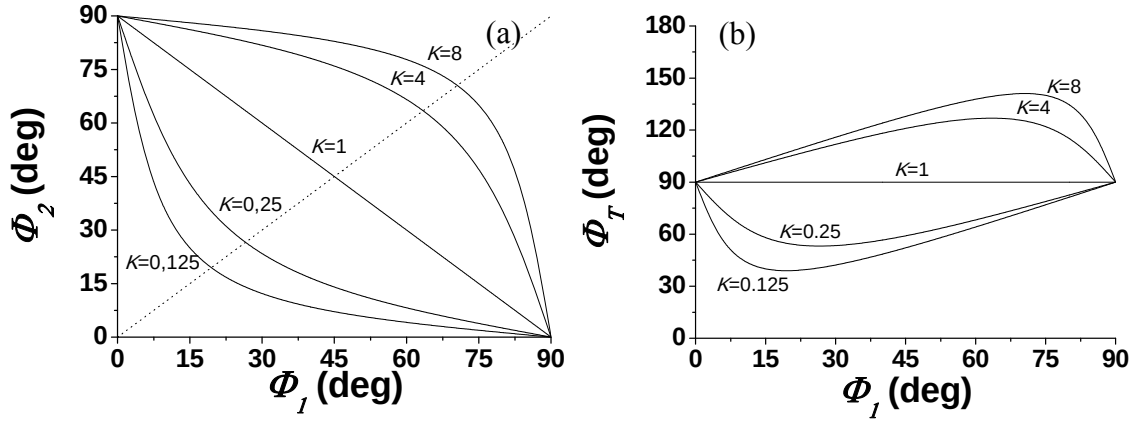


**Figure 6.2.** Electrical lengths at resonance according to expression (6.3) (a) $\Phi_1$ and $\Phi_2$ (b) $\Phi_T = \Phi_1 + \Phi_2$ and $\Phi_1$ (Reproduced from [80]).

In order to minimize the total electrical length ($\Phi_T = \Phi_1 + \Phi_2$) of the resonator, the impedance ratio must be $K<1$ (as it can be seen in Figure 6.2). Also, the higher the impedance contrast ($K<<1$), the smaller the electrical length of the SISS [77]. The reduction of $\Phi_T$ is important for two reasons: (i) to reduce the size of the SISS, and (ii) to be able to describe the SISS by means of a lumped element circuit model (series LC resonator). Under the assumption that the two transmission line sections of the SISS are electrically small, we can linearize the tangents in (6.1), and the admittance of the SISS is found to be:

$$Y_{SISS} = -j \frac{\Phi_1 + K\Phi_2}{Z_2 \Phi_1 \Phi_2 - Z_1} \tag{6.4}$$

This admittance is identical to that of an LC series resonant tank, given by

$$Y_{LC} = -j \frac{\omega C}{LC\omega^2 - 1} \tag{6.5}$$

(being $\omega$ the angular frequency), provided the following mapping is satisfied:

$$C = \frac{l_1}{v_{p1} Z_1} + \frac{l_2}{v_{p2} Z_2} = C_1 + C_2 \tag{6.6}$$

$$L = \frac{Z_2 l_2}{v_{p2}} \frac{\dfrac{l_1}{v_{p1} Z_1}}{\dfrac{l_1}{v_{p1} Z_1} + \dfrac{l_2}{v_{p2} Z_2}} = L_2 \frac{C_1}{C_1 + C_2} \tag{6.7}$$

where $v_{p1}$ and $v_{p2}$ are the phase velocities of the low and high impedance transmission line sections, respectively, $C_1$ and $C_2$ are the line capacitances, namely,

$$C_1 = \frac{l_1}{v_{p1} Z_1} = C_{pul1} \cdot l_1 \tag{6.8}$$

$$C_2 = \frac{l_2}{v_{p2} Z_2} = C_{pul2} \cdot l_2 \tag{6.9}$$

$C_{puli}$ ($i$=1,2) being the per unit length capacitances of the lines, and $L_2$ is the inductance of the high impedance transmission line section, i.e.,

$$L_2 = L_{pul2} \cdot l_2 \tag{6.10}$$

Notice that although $C$ is dominated by the capacitance of the low impedance transmission line section, $C_1$, the contribution of $C_2$ on $C$ may be non-negligible if either $K$ or $l_2$ are not very small. It is also interesting to note that $L$ is somehow affected by the capacitive line section, such inductance being smaller than the inductance of the high impedance transmission line section, $L_2$.

Since it is convenient to reduce the electrical length of the SISS as much as possible, the impedance ratio must be minimized, and for this reason the impedance $Z_2$ is set to that value of the minimum strip width achievable with the available technology (we have considered $W_2$ = 160 μm). For the low-impedance transmission line section, a maximum width must be considered in order to avoid transverse resonances. Such maximum width is chosen according to [81]:

$$W_{1\max} = \frac{c\pi}{n\omega_o \sqrt{\varepsilon_r}} - 0.4h \tag{6.11}$$

where $c$ is the speed of light in vacuum, $h$ the substrate thickness, $\varepsilon_r$ the dielectric constant, $\omega_o$ is the resonance frequency of the SISS (i.e. the transmission zero frequency), and $n$ is a dimensionless factor that gives the maximum frequency ($n\omega_o$) where transverse resonances are avoided. From $W_{1max}$ the impedance $Z_1$ can be easily inferred from a transmission line calculator.

Once the maximum and minimum values of $Z_2$ and $Z_1$, respectively, are determined, the next step for the determination of the allowable (implementable) $L$ and $C$ values is to express $\Phi_1$ and $\Phi_2$ as a function of $L$ and $C$. The following results are obtained [79]:

$$\Phi_1 = \frac{C\omega Z_1}{2}\left(1+\sqrt{1-\frac{4L}{CZ_2^2}}\right) \tag{6.12}$$

$$\Phi_2 = \frac{C\omega Z_2}{2}\left(1-\sqrt{1-\frac{4L}{CZ_2^2}}\right) \tag{6.13}$$

These electrical lengths must be smaller than a certain predetermined value at a certain frequency. Typically, a line is considered to be electrically short if its electrical length is smaller than $\pi/4$. Therefore, for an accurate description of the behavior of the SISS by means of a simple LC series resonator in shunt connection, it seems reasonable to limit the electrical lengths of the high and low impedance line sections to be smaller than $\pi/4$ up to a frequency beyond the resonance frequency, $\omega_o=(LC)^{-1/2}$ (this guarantees that the SISS can be described by means of an LC resonator in the region of interest). Thus, we can choose $\omega=n\omega_o$ in (6.12) and (6.13), with $n>1$. This leads to:

$$\Phi_1 = \frac{nZ_1}{2Z_{eq}}\left(1+\sqrt{1-4\left(\frac{Z_{eq}}{Z_2}\right)^2}\right) \tag{6.14}$$

$$\Phi_2 = \frac{nZ_1}{2Z_{eq}}\left(1-\sqrt{1-4\left(\frac{Z_{eq}}{Z_2}\right)^2}\right) \tag{6.15}$$

where

$$Z_{eq} = \sqrt{\frac{L}{C}} \tag{6.16}$$

is an equivalent impedance. Notice that expressions (6.14) and (6.15) depend on $L$ and $C$ through $Z_{eq}$, i.e., they do not depend on the specific values of $L$ and $C$, but on its ratio. By forcing (6.14) and (6.15) to be smaller than $\pi/4$, we obtain the implementable values of $Z_{eq}$ as a function of the resonance frequency. From them, we then translate the information to the LC plane [79]. That is, each resonance frequency corresponds to a certain curve in the LC plane. From the range of values of $Z_{eq}$ corresponding to such resonance frequency, the allowable values of $L$ and $C$ in each curve can be obtained. As an example, Figure 6.3 depicts the allowable regions in the LC plane for $n = 2$, for the *Rogers RO3010* substrate with thickness $h = 1.27$ mm and dielectric constant $\varepsilon_r = 10.2$. By choosing $L$ and $C$ within the region corresponding to $n = 2$, the synthesized SISS can potentially describe the shunt connected LC series resonator to a very good approximation up to at least $2\omega_o$.

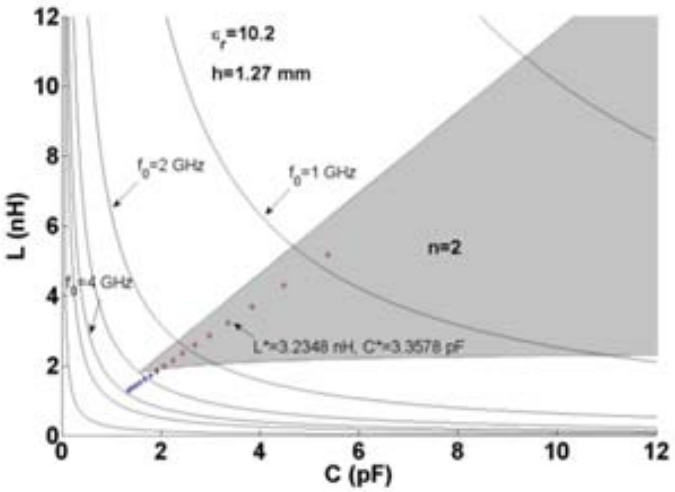


**Figure 6.3.** Allowable values of $L$ and $C$ for $n$ = 2 in the indicated substrate. The $L$ and $C$ values corresponding to the example reported in next subsection are indicated (extracted from [82])

### 6.1.2 Synthesis of the SISS through ASM optimization

Our specific objective is to use ASM to automatically generate the layout of the SISS that gives an electromagnetic response identical to that of the desired shunt connected series LC resonator [82]. To this end, the procedure presented in section 2.2 has been used. In this case, the target coarse model vector, $\mathbf{x}_c^*$, is composed by the desired values of $L$ and $C$ and the lengths $l_1$ and $l_2$ are the geometrical variables of the fine model, corresponding to the low- and high-impedance transmission line sections, respectively, that compounds the vector $\mathbf{x}_f$. The widths are set to $W_2$ = 160 μm (as mentioned before) and $W_1$ = 10 mm (slightly lower than the maximum value given by (6.11) to ensure that transverse resonances do not appear).

As in the aforementioned procedure, the following main modules are necessary: initial geometry estimation module, EM solver module and parameter extraction module. In this occasion, the geometrical variables (the lengths $l_1$ and $l_2$) can be obtained from (6.14) and (6.15) and taking into account the following relation:

$$l_i = \frac{c}{n\omega_0\sqrt{\varepsilon_{effi}}}\Phi_i \tag{6.17}$$

where $\varepsilon_{effi}$ is the effective relative permittivity of the corresponding transmission line section, that can be estimated by using the well-known microstrip formulas [29]. Concerning the EM solver module, it is similar to that previously reported, but in this case it is quite simple since the topology can be described only by rectangles. The $L$ and $C$ values can be inferred from the transmission zero and from the reactance slope at resonance, which is the main function of the parameter extraction module.

The process of automated synthesis of the SISS by using the ASM algorithm is similar to that described in section 4.1 and section 4.2, but in this case the initial Broyden matrix is computed as follows:

$$\mathbf{B}^{(1)} = \begin{pmatrix} \dfrac{\delta L}{\delta l_1} & \dfrac{\delta L}{\delta l_2} \\ \dfrac{\delta C}{\delta l_1} & \dfrac{\delta C}{\delta l_2} \end{pmatrix} \tag{6.18}$$

and the norm of the error function is expressed as follows:

$$\left\| \mathbf{f}(x_f) \right\| = \sqrt{\left(1 - \frac{L}{L^*}\right)^2 + \left(1 - \frac{C}{C^*}\right)^2} \tag{6.19}$$

As an example, a SISS with target values: $L^*$= 3.2348 nH and $C^*$ = 3.3578 pF is designed (this SISS will be later used for the design of an elliptic low pass filter and this explains these very specific values). Notice that these values lie within the convergence region in Figure 6.3 (the considered substrate is the *Rogers RO3010* with thickness $h$ = 1.27 mm and dielectric constant $\varepsilon_r$ = 10.2). The algorithm ends when (6.19) is smaller than a certain predefined value. In our case, it has been found that 12 iterations suffice to obtain an error function smaller than 0.3%.

The target response, i.e., that inferred from circuit simulation of the target $L^*$ and $C^*$ values, and the EM simulations of the initial and final layouts are all depicted in Figure 6.4 where the final layout is also included in the inset. As can be seen, the agreement between the circuit (target) and electromagnetic simulation after optimization is excellent in the frequency range shown (up to $2f_o$).

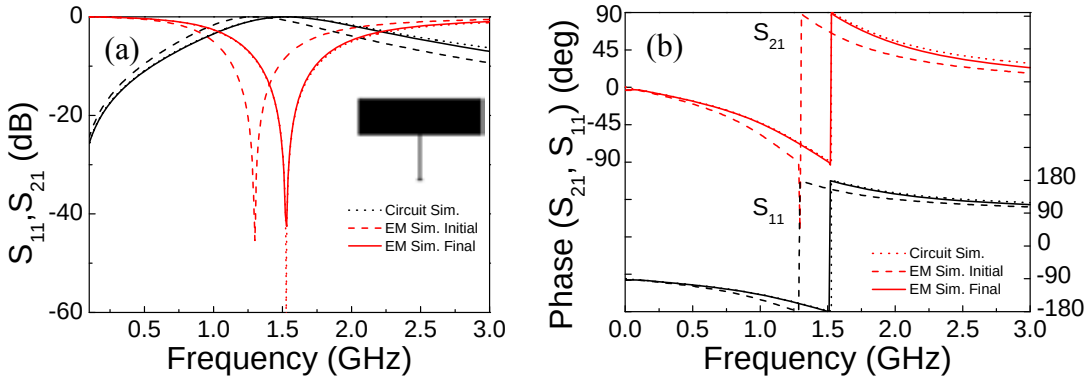


**Figure 6.4.** Magnitude (a) and phase (b) of circuit and EM simulation of the synthesized SISS. The lengths and widths of the transmission line sections for the final synthesized SISS are $l_1$ = 3.09 mm, $l_2$ = 3.65 mm, $W_1$ = 10 mm and $W_2$ = 0.16 mm.

### 6.1.3 Design of an order-3 elliptic low pass filter

In order to illustrate a potential application of the ASM algorithm to the design of microwave devices, the SISS synthesized above has been used for the design of an order-3 elliptic-function low pass filter (the circuit model is depicted in Figure 6.5). Filter specifications are: pass-band ripple $L_{Ar}$ = 0.1 dB, cutoff frequency $f_c$ = 800 MHz, and stop-band attenuation of $L_{As}$ = 18.8571 dB with the equal-ripple stop-band starting normalized frequency $\Omega_s$ = 1.6949. Such specifications give an inductance of $L_s \equiv L_1 = L_3$ = 8.289 nH, $L_2$ and $C_2$ being given by those values considered in the previous example (i.e., $L_2 = L$ = 3.2348 nH, $C_2 = C$ = 3.3578 pF). The inductance $L_s$ has been implemented by means of a narrow strip of minimum width (160 μm). However, since the inductance value is large, it has been necessary to etch a window in the ground plane. By this means, the strip exhibits a linear reactance in a wider frequency range. The strip length has been determined by optimization (i.e., by comparing the series reactance of the equivalent π-circuit to that of the inductance $L_s$). The layout and photograph of the filter are depicted in Figure 6.6. The device has been fabricated by means of the *LPKF-HF-100* drilling machine. The frequency response of the filter is depicted in Figure 6.7. The agreement between the ideal elliptic-function response and the response obtained from full wave electromagnetic simulation is very good up to 2 GHz. Above that frequency, the slight discrepancy is due to the deviation of the reactance of the series strip from the required linear (purely inductive) behavior. The measured filter response exhibits some discrepancies which are attributed to tolerances in the dielectric constant of the substrate and final dimensions. It is worth mentioning that the SISS used in the filter is exactly the same SISS synthesized before, i.e., no further post optimization has been carried out.

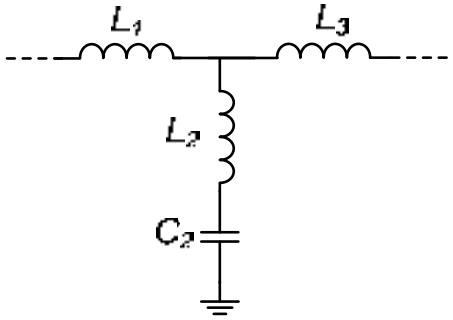


**Figure 6.5.** Circuit model of an order-3 elliptic-function low pass filter.

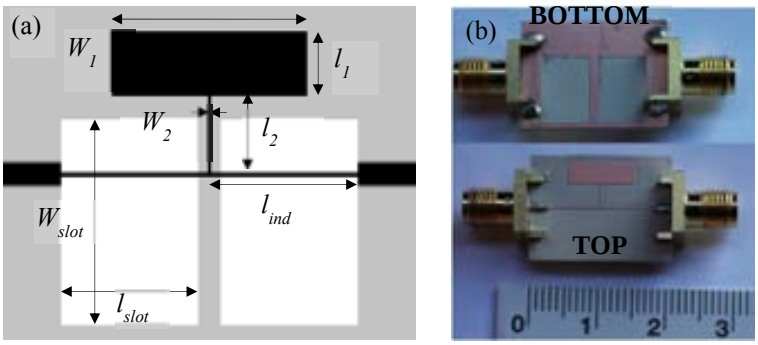


**Figure 6.6.** Layout (a) and photograph (b) of the fabricated filter. Dimensions are: $l_1$ = 3.09 mm, $l_2$ =3.65 mm, $W_1$ = 10 mm, $W_2$ = 0.16 mm, $l_{ind}$ = 7.5 mm, $l_{slot}$ = 7 mm and $W_{slot}$ = 9.8 mm (extracted from [82]).

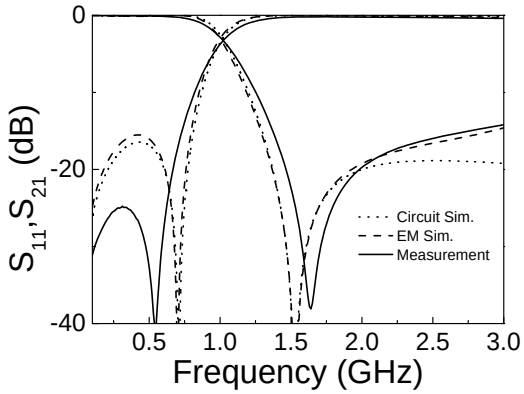


**Figure 6.7.** Frequency response of the designed filter (extracted from [82])..

## 6.2 ASM applied to the design of RF/microwave inductors

Nowadays, RF/microwave inductors are needed in most communication systems. For this reason, the idea of automatically synthesize this kind of inductors in planar technology is interesting. The main aim of this section is to demonstrate the viability of this automated synthesis by means of an ASM algorithm. As proof-of-concept, a spiral inductor has been considered (see Figure 6.8). This is a well-known structure [67], and it is possible to predict the value of the equivalent inductance, as well as the related quality factor, and self-resonance frequency, from the geometry of the structure and substrate parameters, according to analytical expressions. Therefore, it is possible to give an estimation of the particle geometry by inverting these analytical expressions. However, the analytical expressions are only approximate, and therefore optimization is required in a second step, in order to find the topology given the target element values (typically inductance and minimum required quality factor). In this section, the ASM technique will be applied to automatically synthesize a one turn inductor for a given substrate parameters and target inductance value.

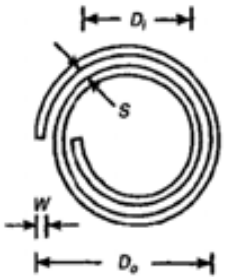


**Figure 6.8.** Topology of a spiral inductor (extracted from [67]).

### 6.2.1 Analysis of the spiral inductor

According to [67], the equivalent circuit model of the inductor given in Figure 6.8 is that depicted in Figure 6.9.9

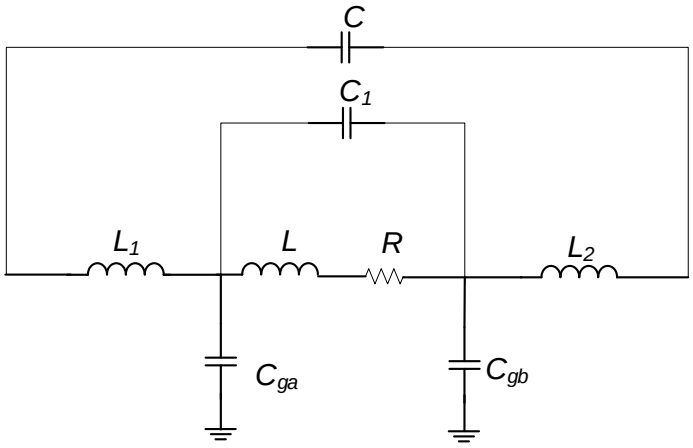


**Figure 6.9.** Equivalent circuit model of the structure depicted in Figure 6.8.

In order to simplify the model and the algorithm implementation, losses are neglected ($R = 0$) and we have considered a one turn spiral, which means that the capacitances $C_1$ and $C_2$ are not taken into account Therefore, the circuit can be simplified to that depicted in Figure 6.10.

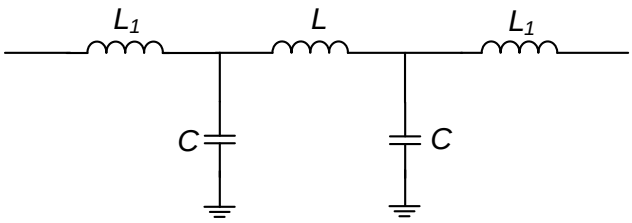


**Figure 6.10**. Simplified equivalent circuit model without losses

In order to study the behavior of this circuit, it can be transformed to its equivalent T-circuit model (Figure 6.11). Notice that, although the structure is not symmetrical, we have considered a symmetrical circuit as a first approach, where the series and shunt impedance can be written as:

$$Z_{sT_{eq}} = \frac{j\omega\left[\omega^2 LL_1 C - \left(2L_1 + L\right)\right]}{\omega^2 LC - 2} \tag{6.20}$$

$$Z_{pT_{eq}} = j\frac{1}{\omega C\left(\omega^2 LC - 2\right)} \tag{6.21}$$

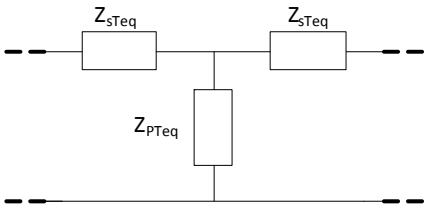


**Figure 6.11**. Equivalent T-circuit model.

In order to validate this simplified model, the S-parameters of a typical spiral inductor have been inferred from EM simulation, and compared to those obtained from the circuit simulation with the extracted parameters (the circuit parameters can be inferred by obtaining the series and shunt reactances at different frequency points and by combining equations (6.20) and (6.21)). The comparison is depicted in Figure 6.12, where good agreement between the electromagnetic simulation and the circuit simulation is visible. Obviously, any circuit model of a semi-lumped element is frequency limited, and for this reason the model fails close to the self-resonance frequency. Nevertheless, the agreement is good well below such self-resonance frequency, where it is supposed that the inductor must operate.

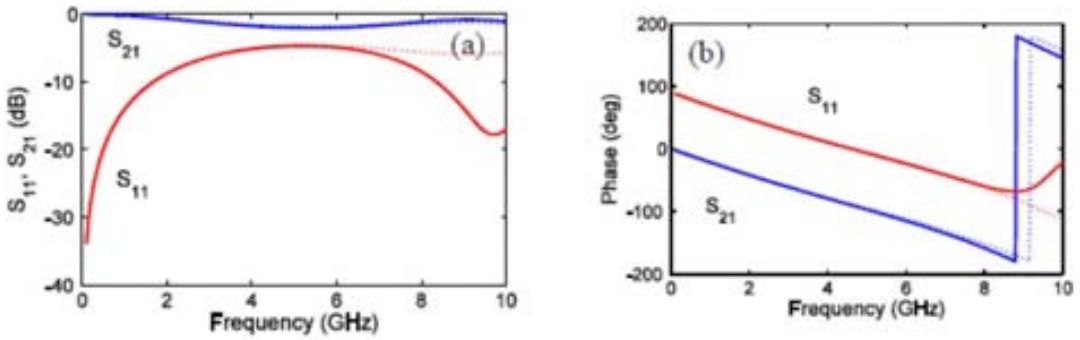


**Figure 6.12.** Magnitude (a) and phase (b) of EM simulation (solid line), and equivalent circuit model (dotted line).

Figure 6.13 shows the comparison between the series and shunt reactance of the equivalent T-circuit obtained from electromagnetic and circuit simulation, and again, the agreement is good. Therefore, these results validate the simplified circuit model considered for the structure.

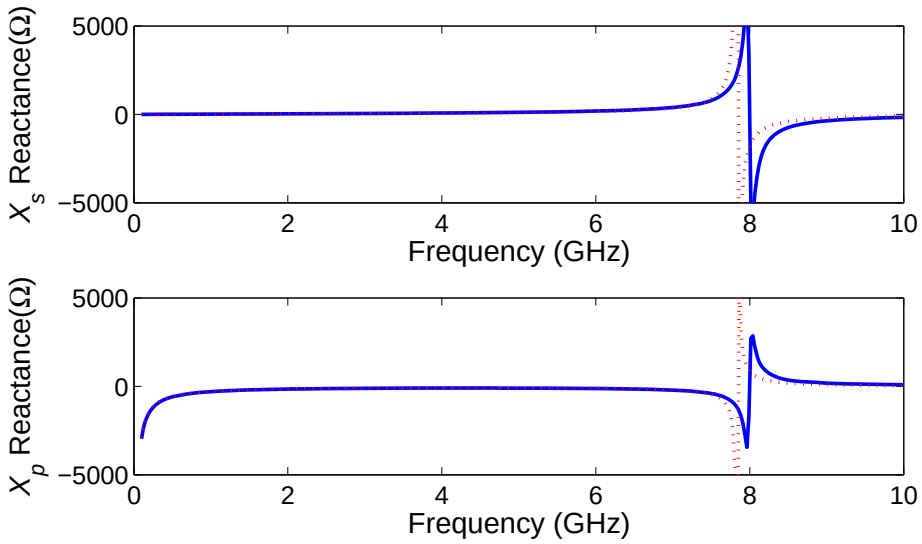


**Figure 6.13.** Series and shunt reactance of EM simulation (solid line), and equivalent circuit model (dotted line).

## 6.2.2 Optimization by means of the ASM algorithm

Our goal is to obtain a specified inductance and considering that at low frequencies the structure behaves as and inductor with value:

$$L_{eq} = 2L_1 + L \tag{6.22}$$

Then the target is to reach a topology giving the inductance value $L_{eq}$. For the considered structure we have 3 geometrical parameters: $s$, $W$ and $R_{int}$ (see Figure 6.14). This problem has infinite solutions, but if $s$ and $W$ are fixed to be the minimum for a given technology, there is only one physical parameter to optimize ($R_{int}$).

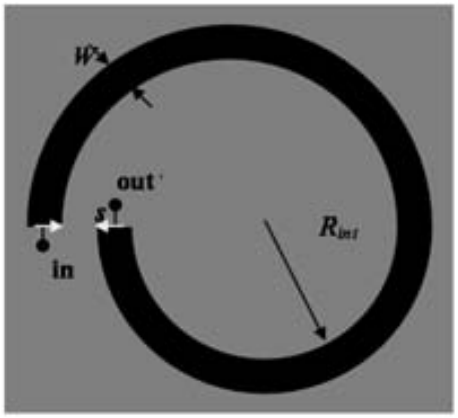


**Figure 6.14**. Topology of spiral inductor

As in the previously presented applications of ASM algorithm, first of all, the initial layout must be estimated, in this case, by using the following expressions:

$$L[nH] = 0.03937 \frac{a^2 n^2}{8a + 11c} K_g \tag{6.23}$$

where

$$a = \frac{D_o + D_i}{4} \qquad c = \frac{D_o - D_i}{4} \tag{6.24}$$

which are related to the geometrical parameters defined in Figure 6.14 as follows:

$$D_i = 2R_{int} \qquad D_o = 2(R_{int} + 2W + s) \tag{6.25}$$

being $K_g$ a correction factor [67] to take into account the presence of the ground plane, $n$ the number of turns (1 in our case), $D_o$ the external diameter and $D_i$ the inner diameter, see Figure 6.8.

The whole process of the ASM algorithm is identical than the previously described but in this case the norm of error function is defined as:

$$\left\| \mathbf{f}(x_f) \right\| = \sqrt{\left( \frac{L_{eq} - L_{eq}^*}{L_{eq}^*} \right)^2} \tag{6.26}$$

### 6.2.3 Examples

Let us consider two illustrative examples, the considered substrate is *Rogers RO3010* with a dielectric constant of $\varepsilon_r$ = 10.2 and substrate height of $h$=1.27mm. In both cases the fixed geometrical parameters are $W$=250μm and $s$=250μm and the frequency range is 0.1 to 5 GHz.

For the first example, the target inductance value is $L_{eq}^*$ = 5.0 nH and the initial value of internal radius is $R_{int}$ = 1.68 mm. After the EM simulation, the extracted parameters are $L$ = 5.25 nH, $C$ = 0.46 pF, $L_1$ = 1.47 nH, that is a resulting equivalent inductance of $L_{eq}$ = 8.20 nH, that leads to an error of 63.9% (see Table XIII). Nevertheless, the convergence is achieved after 2 iterations and the norm of the error function is less than 1%.

TABLE XIII COARSE AND FINE MODEL PARAMETERS OF EXAMPLE 1

| Step | $L_{eq}$[nH]= $L$+2$L_1$ | $R_{int}$[mm] | ‖f($x_f$)‖ |
|---|---|---|---|
| Initial | 8.20 | 1.68 | 0.639 |
| 1 | 5.07 | 1.08 | 0.015 |
| 2 | 5.00 | 1.07 | 0.001 |

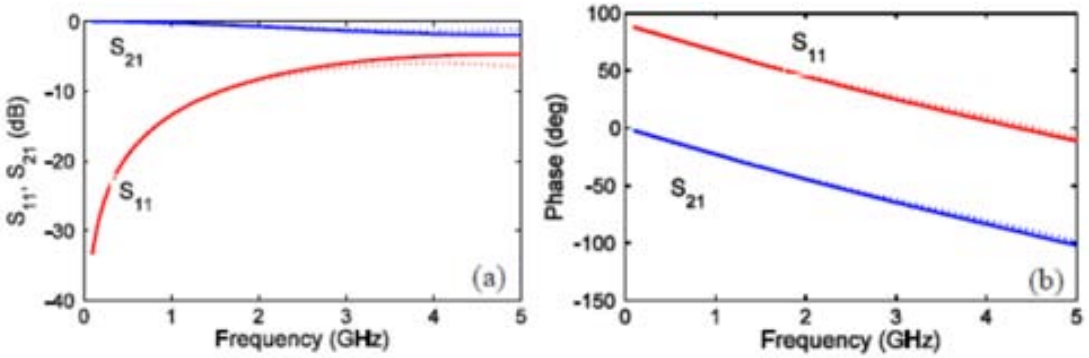


**Figure 6.15.** Magnitude (a) and phase (b) of EM simulation (solid line), and equivalent circuit model (dotted line).

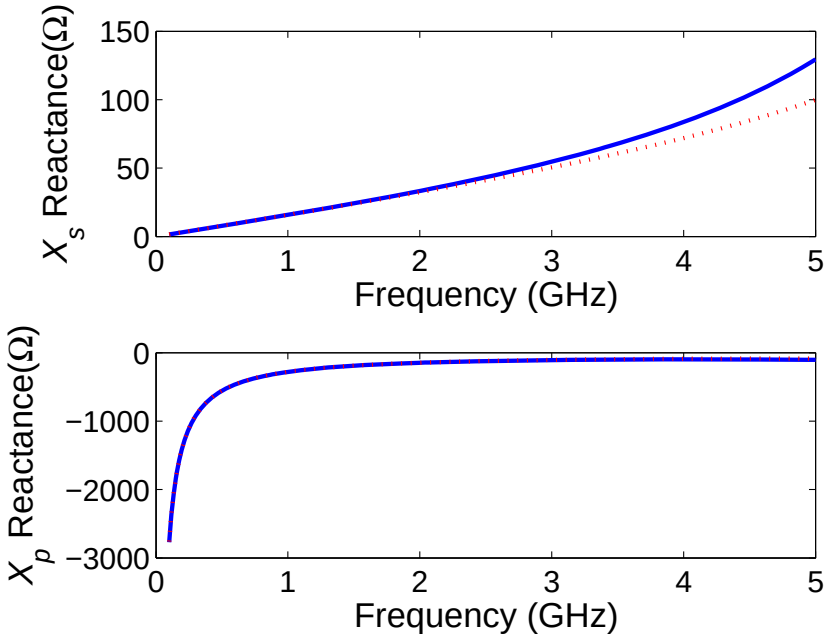


**Figure 6.16.** Series and Shunt reactance: circuit (dashed line) and EM (solid line) of final solution.

The frequency response as well as the series and shunt reactance of the final solution from EM simulation and circuit simulation are depicted in Figure 6.15 and Figure 6.16, respectively. In both figures, the agreement between EM and circuit simulation is good since the model is valid.

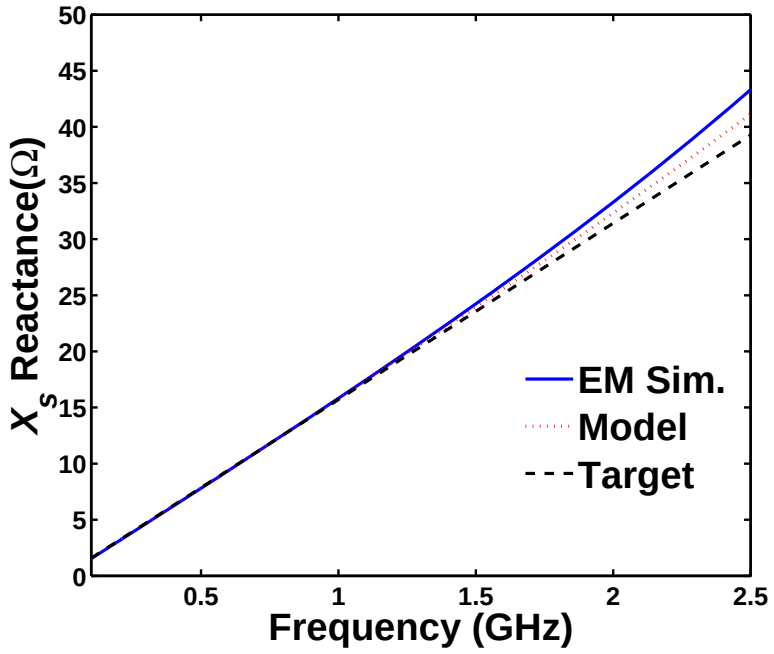


**Figure 6.17.** Series Reactance: circuit (dotted line), EM (solid line) and $L_{eq}^{*}$ (dashed, which corresponds to the simulation of a single inductance of value $L_{eq}^{*}$) of final solution.

In Figure 6.17 series reactance of final solution from EM simulation and circuit simulation is depicted and compared with the simulation of a single inductance of value $L_{eq}^{*}$. It can be seen that the series reactance behaves as a pure inductance with small error up to roughly 2-2.5GHz.

In the second example, the target inductance value is considered to be $L_{eq}^{*}$ = 3.5 nH and the initial value of internal radius obtained by the geometrical estimation module is $R_{int}$ = 1.24 mm. After the first EM simulation, the extracted parameters are $L$ = 3.35 nH, $C$ = 0.34 pF and $L_1$ = 1.27 nH (i.e., $L_{eq}$ = 5.90 nH,) and the initial error is 68.6%. Therefore, an error less than 0.1% is achieved after 2 iterations (the values of the coarse and fine model parameters at each step are given in Table XIV).

TABLE XIV COARSE AND FINE MODEL PARAMETERS OF EXAMPLE 2

| Step | $L_{eq}$[nH]= $L$+2$L_1$ | $R_{int}$[mm] | $\|\|\mathbf{f}(\mathbf{x}_f)\|\|$ |
|---|---|---|---|
| Initial | 5.90 | 1.24 | 0.686 |
| 1 | 3.31 | 0.74 | 0.055 |
| 2 | 3.50 | 0.78 | 0.000 |

Similarly to the example 1, the target inductance has been achieved and the series reactance behaves as a pure inductance with small error up to roughly 2-2.5GHz, as it can be seen in Figure 6.18, where the series reactance of the final solution obtained from the EM, equivalent circuit model and single inductance simulations are compared.

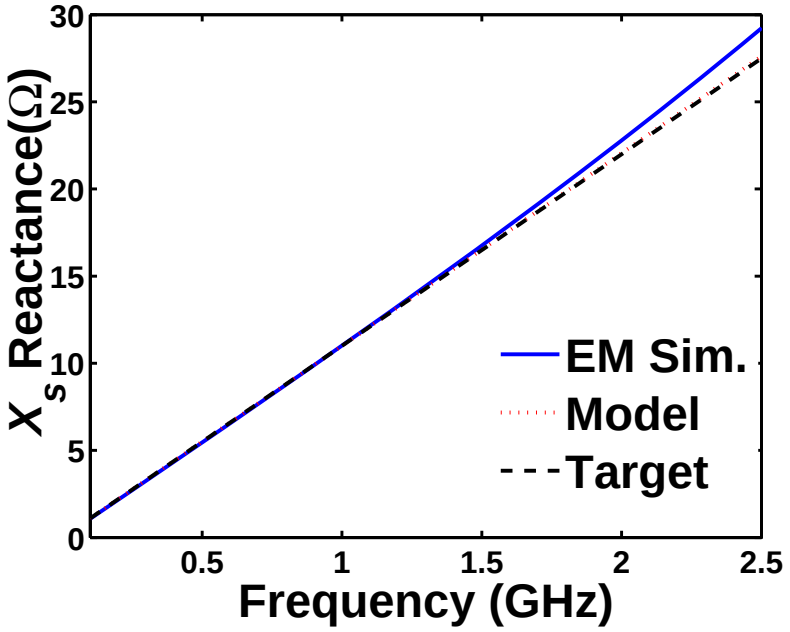


**Figure 6.18.** Series Reactance: circuit (dotted line), EM (solid line) and $L_{eq}^{*}$ (dashed, which corresponds to the simulation of a single inductance of value $L_{eq}^{*}$) of final solution of example 2.

---

In **summary**, in this chapter, on the one hand, it has been demonstrated that ASM optimization is a very efficient tool for the synthesis of SISS resonators in microstrip technology. By choosing the *L* and *C* values of the SISS within the convergence regions of the LC plane, the developed ASM provides excellent accuracy, as revealed by the perfect match between the circuit and EM response of the designed SISS. The synthesized SISS has been used for the design of an elliptic low pass filter, hence demonstrating the utility of the ASM to assist in the design of practical microwave devices. On the other hand, it has been demonstrated that the ASM algorithm can be applied to the design of RF/microwave planar inductors. A first order tool to synthesize a one turn spiral inductor has been developed by using a simplified model and considering only one physical parameter to optimize. However, this opens the path to develop a more realistic optimization tool for the design of RF/microwave planar inductors by using ASM algorithms. In conclusion, the ASM technique presented in this thesis is useful to the design of other microwave structures in addition to those based on metamaterials.

# 7

# Conclusions and future work

This thesis is enclosed on the application of novel techniques of SM to the design of microwave devices and focused on the synthesis of planar metamaterial transmission lines by means of ASM algorithms. Specifically, the CSRR-loaded transmission line unit cells have been considered in this work since they are well-known structures in our group and in the metamaterials community as well. For this purpose, several ASM algorithms have been developed in order to demonstrate the capability and the potentiality of these techniques to the automated synthesis of this kind of lines. Moreover, several design applications have been reported in order to validate the ASM algorithm functionality. Also, improvements of the original algorithm have been investigated. Furthermore, the application of the presented ASM technique to other microwave devices has been discussed. In summary, it has been demonstrated that ASM algorithms are useful for the automated synthesis of metamaterial transmission lines and, in general, for planar microwave circuits that can be described through lumped element equivalent circuits.

The contents of this work have been divided into six chapters (excluding the conclusions). Once the motivation and general objectives have been pointed out in **chapter 1**, the main aspects discussed in each chapter are listed below:

In **chapter 2**, on the one hand, metamaterial transmission line concepts have been introduced, focusing on the CRLH transmission line concept, and the Bloch wave analysis of periodic structures. On the other hand, SM algorithms have been presented

by explaining the general formulation of the algorithm and highlighting the use of ASM. Moreover, a state of the art of SM algorithms has been summarized.

In **chapter 3**, the design and implementation of circuits based on resonant-type CRLH balanced unit cells by means of CSRRs, CSRs and SRRs have been introduced. The analysis of the characteristic impedance and dispersion relation has been reported for the balanced case, and the design equations related to the circuit model parameters have been shown as well. Furthermore, the application of resonant type CRLH balanced lines to the design of microwave broadband filters has been demonstrated and several illustrative examples in microstrip and CPW technology have been designed and fabricated.

In **chapter 4**, the automated synthesis of circuits based on CSRRs by means of ASM algorithms has been demonstrated. Specifically, the synthesis of CSRR-loaded lines with and without series gaps has been considered. The main modules of the ASM algorithm and the automated synthesis have been explained in detail in both cases, by highlighting the main differences. Additionally, the algorithm improvements have been shown, presenting a new fast two step ASM algorithm.

In **chapter 5**, in order to illustrate the viability of the new two-step ASM algorithm presented in chapter 4, two examples of its application in the design of CSRR-based devices have been reported. On the one hand, a stop-band filter formed by three CSRR-loaded unit cells without gaps by applying the aforementioned algorithm has been designed and fabricated. On the other hand, the tool has been applied to the design of a dual-band power divider and the convergence region has revealed that the considered target values are not implementable. However, with the addition of two transmission line sections, these element values have been relaxed and the device has been designed and fabricated. Good agreement between simulations and measurements has been found in both examples.

In **chapter 6**, the application of the ASM algorithm to other microwave devices has been demonstrated. First of all, the automated synthesis of SISS resonators in microstrip technology by means of ASM optimization has been reported. By choosing the $L$ and $C$ values of the SISS within the convergence regions of the LC plane, the developed ASM provides excellent accuracy, as revealed by the perfect match between the circuit and EM response of the designed SISS. In order to illustrate the potential of the algorithm, the synthesized SISS has been used for the design of an elliptic low pass filter. Second, the application of the ASM algorithm to the design of RF/microwave planar inductors has been explored. Specifically, a first order tool to synthesize a one turn spiral inductor has been developed by using a simplified model and considering only one physical parameter to optimize. Accordingly, it has been demonstrated that ASM optimization can be a very efficient tool for the synthesis of other microwave structures in addition to those based on metamaterials.

As a **general conclusion**, the objectives proposed have been achieved. The methodology as well as the results of the work compiled in this thesis consolidate the possibility of applying ASM algorithms to metamaterial transmission lines and opens a new path on the automated synthesis of planar microwave circuits based on parameter extraction.

Different **future research lines** can emerge from this thesis. For instance, ASM algorithm can be applied to open particles: Open Split Ring Resonator (OSRR) and Open Complementary Split Ring Resonator (OCSRR). Indeed, we have started to explore these structures because they are electrically small (electrical size is roughly a half than that of CSRRs and SRRs) and its equivalent circuit model is, in a first approach, a LC series resonator for the OSRR and a LC parallel resonator for the OCSRR. As it has been reported in previous works, like in M. Durán-Sindreu Ph. D. thesis, these particles are useful for the design of microwave band-pass filters, multi-band components, among others with reduced dimensions. For these reasons, the development of a tool based on ASM algorithm to optimize the aforementioned particles is a motivating research line.

Concerning the application of ASM algorithms to other microwave structures, it is noteworthy that, it has been applied to the synthesis of semi-lumped resonators and a tool for automate the design and synthesis of microwave band pass filters based on immitance inverters has been initiated. Specifically, the main objective was to synthetize a filter layout automatically from a given filter response specifications. In order to achieve that, on the one hand, it is necessary to optimize each semi-lumped resonator to match with the required circuit elements of the equivalent circuit model and, on the other hand, the phase shift of each cell (resonator with inverter) must be optimized to be 90º. The aforementioned research line has started in a work co-directed by the author and the supervisor of this thesis and developed by Marc Sans to obtain his Master's degree in Electronic Engineering.

Finally, the possibility to apply the ASM algorithm to structures based on metamaterial based transmission lines and other microwave components opens a new path in microwave design. The idea to integrate an optimization tool based on the algorithms presented in this thesis in commercial electromagnetic software is a potential issue. For instance, one aspect can be the development of a component library capable to optimize several microwave structures or the integration of a design guide for microwave devices based on ASM algorithms.

# References


[1] C. Caloz and T. Itoh, "Novel microwave devices and structures based on the transmission line approach of meta-materials", *IEEE MTT-S International Microwave Symposium Digest*, Philadelphia, PA, USA, pp. 195-198, 8-13 June 2003.

[2] A. K. Iyer and G. V. Eleftheriades, "Negative refractive index metamaterials supporting 2-D waves", *IEEE MTT-S International Microwave Symposium Digest*, Seattle,WA, USA, pp. 1067-1070 2-7 June 2002.

[3] A. A. Oliner, "A periodic-structure negative-refractive-index medium without resonant elements", *IEEE-APS/URSI International Symposium Digest*, San Antonio, Texas, USA, 16-21 June 2002.

[4] F. Martin, J. Bonache, F. Falcone, M. Sorolla, and R. Marques, "Split ring resonator-based left-handed coplanar waveguide", *Applied Physics Letters*, vol. 83, no. 22, pp. 4652-4654, Dec. 2003.

[5] F. Martin, F. Falcone, J. Bonache, R. Marques, and M. Sorolla, "Miniaturized coplanar waveguide stop band filters based on multiple tuned split ring resonators", *IEEE Microwave and Wireless Components Letters*, vol. 13, no. 12, pp. 511-513, Dec. 2003.

[6] F. Falcone, T. Lopetegi, M. A. G. Laso, J. D. Baena, J. Bonache, M. Beruete, R. Marques, F. Martin, and M. Sorolla, "Babinet principle applied to the design of metasurfaces and metamaterials", *Physical Review Letters*, vol. 93, no. 19, pp. 197401(1)-197401(4), Nov. 2004.

[7] M. A. Antoniades and G. V. Eleftheriades, "A broadband series power divider using zero-degree metamaterial phase-shifting lines", *IEEE Microwave and Wireless Components Letters*, vol. 15, no. 11, pp. 808-810, Nov. 2005.

[8] M. A. Antoniades and G. V. Eleftheriades, "A broadband Wilkinson balun using microstrip metamaterial lines", *IEEE Antennas and Wireless Propagation Letters*, vol. 4, pp. 209-212, 2005.

[9] H. Okabe, C. Caloz, and T. Itoh, "A compact enhanced-bandwidth hybrid ring using an artificial lumped-element left-handed transmission-line section", *IEEE Transactions on Microwave Theory and Techniques*, vol. 52, no. 3, pp. 798-804, March 2004.

[10] D. Kholodnyak, E. Serebryakova, I. Vendik, and O. Vendik, "Broadband digital phase shifter based on switchable right- and left-handed transmission line sections", *IEEE Microwave and Wireless Components Letters*, vol. 16, no. 5, pp. 258-260, May 2006.

[11] G. Siso, M. Gil, J. Bonache, and F. Martin, "Application of metamaterial transmission lines to design of quadrature phase shifters", *Electronics Letters*, vol. 43, no. 20, pp. 1098-1100, Sep. 2007.

[12] G. Siso, M. Gil, J. Bonache, and F. Martin, "Applications of resonant-type metamaterial transmission lines to the design of enhanced bandwidth components with compact dimensions", *Microwave and Optical Technology Letters*, vol. 50, no. 1, pp. 127-134, Jan. 2008.

[13] J. Bonache, G. Siso, M. Gil, A. Iniesta, J. Garcia-Rincon, and F. Martin, "Application of composite right/left handed (CRLH) transmission lines based on complementary split ring resonators (CSRRs) to the design of dual-band microwave components", *IEEE Microwave and Wireless Components Letters*, vol. 18, no. 8, pp. 524-526, Aug. 2008.

[14] M. Duran-Sindreu, G. Siso, J. Bonache, and F. Martin, "Planar Multi-Band Microwave Components Based on the Generalized Composite Right/Left Handed Transmission Line Concept", *IEEE Transactions on Microwave Theory and Techniques*, vol. 58, no. 12, pp. 3882-3891, Dec. 2010.

[15] S. H. Ji, C. S. Cho, J. W. Lee, and J. Kim, "Concurrent dual-band class-E power amplifier using composite right/left-handed transmission lines", *IEEE Transactions on Microwave Theory and Techniques*, vol. 55, no. 6, pp. 1341-1347, June 2007.

[16] I. H. Lin, M. DeVincentis, C. Caloz, and T. Itoh, "Arbitrary duad-band components using composite right/left-handed transmission lines", *IEEE Transactions on Microwave Theory and Techniques*, vol. 52, no. 4, pp. 1142-1149, April 2004.

[17] A. C. Papanastasiou, G. E. Georghiou, and G. V. Eleftheriades, "A quad-band Wilkinson power divider using generalized NRI transmission lines", *IEEE Microwave and Wireless Components Letters*, vol. 18, no. 8, pp. 521-523, Aug. 2008.

[18] G. Siso, J. Bonache, and F. Martin, "Dual-Band Y-Junction Power Dividers Implemented Through Artificial Lines Based on Complementary Resonators", *IEEE MTT-S International Microwave Symposium Digest*, Atlanta, Georgia, USA, pp. 924-927, 15-20 June 2008.

[19] I. Arnedo, J. Illescas, M. Flores, T. Lopetegi, M. A. G. Laso, F. Falcone, J. Bonache, J. Garcia-Garcia, F. Martin, J. A. Marcotegui, R. Marques, and M. Sorolla, "Forward and backward leaky wave radiation in split-ring-resonator-based metamaterials", *IET Microwaves Antennas & Propagation*, vol. 1, no. 1, pp. 65-68, Feb. 2007.

[20] F. P. Casares-Miranda, C. Camacho-Penalosa, and C. Caloz, "High-gain active composite right/left-handed leaky-wave antenna", *IEEE Transactions on Antennas and Propagation*, vol. 54, no. 8, pp. 2292-2300, Aug. 2006.

[21] A. Grbic and G. V. Eleftheriades, "Leaky CPW-based slot antenna arrays for millimeter-wave applications", *IEEE Transactions on Antennas and Propagation*, vol. 50, no. 11, pp. 1494-1504, Nov. 2002.

[22] S. J. Lim, C. Caloz, and T. Itoh, "Metamaterial-based electronically controlled transmission-line structure as a novel leaky-wave antenna with tunable radiation angle and beamwidth", *IEEE Transactions on Microwave Theory and Techniques*, vol. 52, no. 12, pp. 2678-2690, Dec. 2004.

[23] J. Bonache, I. Gil, J. Garcia-Garcia, and F. Martin, "Novel microstrip bandpass filters based on complementary split-ring resonators", *IEEE Transactions on Microwave Theory and Techniques*, vol. 54, no. 1, pp. 265-271, Jan. 2006.

[24] M. Duran-Sindreu, A. Velez, G. Siso, P. Velez, J. Selga, J. Bonache, and F. Martin, "Recent Advances in Metamaterial Transmission Lines Based on Split Rings", *Proceedings of the IEEE*, vol. 99, no. 10, pp. 1701-1710, Oct. 2011.

[25] M. Gil, J. Bonache, J. Garcia-Garcia, J. Martel, and F. Martin, "Composite right/left-handed metamaterial transmission lines based on complementary split-rings resonators and their applications to very wideband and compact filter design", *IEEE Transactions on Microwave Theory and Techniques*, vol. 55, no. 6, pp. 1296-1304, June 2007.

[26] J. W. Bandler, R. M. Biernacki, S. H. Chen, P. A. Grobelny, and R. H. Hemmers, "Space Mapping Technique for Electromagnetic Optimization", *IEEE Transactions on Microwave Theory and Techniques*, vol. 42, no. 12, pp. 2536-2544, Dec. 1994.

[27] J. W. Bandler, Q. S. S. Cheng, S. A. Dakroury, A. S. Mohamed, M. H. Bakr, K. Madsen, and J. Sondergaard, "Space mapping: The state of the art", *IEEE Transactions on Microwave Theory and Techniques*, vol. 52, no. 1, pp. 337-361, Jan. 2004.

[28] J. W. Bandler, R. M. Biernacki, S. H. Chen, R. H. Hemmers, and K. Madsen, "Electromagnetic optimization exploiting aggressive space mapping", *IEEE Transactions on Microwave Theory and Techniques*, vol. 43, no. 12, pp. 2874-2882, Dec. 1995.

[29] D. M. Pozar, *Microwave Engineering*, 3rd ed. Hoboken, NJ, J. Wiley, 2005.

[30] R. Marqués, F. Martín, and M. Sorolla, *Metamaterials with Negative Parameter: Theory, Design, and Microwave Applications*, Hoboken, N.J., Wiley-Interscience, 2008.

[31] C. Caloz and T. Itoh, *Electromagnetic Metamaterials: Transmission Line Theory and Microwave Applications*, John Wiley & Sons, 2006.

[32] C. Caloz and T. Itoh, "Application of the transmission line theory of left-handed (LH) materials to the realization of a microstrip", *IEEE Antennas and Propagation Society International Symposium*, San Antonio, Texas, USA, pp. 412-415, 16-21 June 2002.

[33] J. B. Pendry, A. J. Holden, D. J. Robbins, and W. J. Stewart, "Magnetism from conductors and enhanced nonlinear phenomena", *IEEE Transactions on Microwave Theory and Techniques*, vol. 47, no. 11, pp. 2075-2084, Nov. 1999.

[34] F. Falcone, T. Lopetegi, J. D. Baena, R. Marques, F. Martin, and M. Sorolla, "Effective negative-epsilon stopband microstrip lines based on complementary split ring resonators", *IEEE Microwave and Wireless Components Letters*, vol. 14, no. 6, pp. 280-282, June 2004.

[35] J. D. Baena, J. Bonache, F. Martin, R. Marques, F. Falcone, T. Lopetegi, M. A. G. Laso, J. Garcia-Garcia, I. Gil, M. F. Portillo, and M. Sorolla, "Equivalent-circuit models for split-ring resonators and complementary split-ring resonators coupled to planar transmission lines", *IEEE Transactions on Microwave Theory and Techniques*, vol. 53, no. 4, pp. 1451-1461, April 2005.

[36] D. R. Smith, W. J. Padilla, D. C. Vier, S. C. Nemat-Nasser, and S. Schultz, "Composite medium with simultaneously negative permeability and permittivity", *Physical Review Letters*, vol. 84, no. 18, pp. 4184-4187, May 2000.

[37] F. Aznar, J. Bonache, and F. Martin, "Improved circuit model for left-handed lines loaded with split ring resonators", *Applied Physics Letters*, vol. 92, no. 4, pp. 043512(1)-043512(4), Jan. 2008.

[38] J. Bonache, M. Gil, O. Garcia-Abad, and F. Martin, "Parametric analysis of microstrip lines loaded with complementary split ring resonators", *Microwave and Optical Technology Letters*, vol. 50, no. 8, pp. 2093-2096, Aug. 2008.

[39] J. W. Bandler. *http://www.bandler.com/mileston2.htm*.

[40] D. G. Swanson and W. J. R. Hoefer, *Microwave Circuit Modeling Using Electromagnetic Field Simulation*, Boston, MA, Artech House, 2003.

[41] D. C. Swanson Jr, "Computer-aided design of passive components", in *Commercial wireless circuits and components hand book*, ed. CRC Press, Inc., 2003, pp. 21.1-21.12.

[42] S. Koziel, Q. S. Cheng, and J. W. Bandler, "Space mapping", *IEEE Microwave Magazine*, vol. 9, no. 6, pp. 105-122, Dec 2008.

[43] C. G. Broyden, "A Class of Methods for Solving Nonlinear Simultaneous Equations", *Mathematics of Computation*, vol. 19, no. 92, pp. 577-593, Oct. 1965.

[44] M. H. Bakr, J. W. Bandler, M. A. Ismail, J. E. Rayas-Sanchez, and Q. J. Zhang, "Neural space mapping EM optimization of microwave structures", *IEEE MTT-S International Microwave Symposium Digest*, Boston, MA, USA, pp. 879-882, 11-16 June 2000.

[45] J. W. Bandler, M. A. Ismail, J. E. Rayas-Sanchez, and Q. J. Zhang, "Neuromodeling of microwave circuits exploiting space-mapping technology", *IEEE Transactions on Microwave Theory and Techniques*, vol. 47, no. 12, pp. 2417-2427, Dec 1999.

[46] J. W. Bandler, M. A. Ismail, J. E. Rayas-Sanchez, and Q. J. Zhang, "Neural inverse space mapping (NISM) optimization for EM-based microwave design", *International Journal of RF and Microwave Computer-Aided Engineering*, vol. 13, no. 2, pp. 136-147, March 2003.

[47] J. W. Bandler, Q. S. Cheng, N. K. Nikolova, and M. A. Ismail, "Implicit space mapping optimization exploiting preassigned parameters", *IEEE Transactions on Microwave Theory and Techniques*, vol. 52, no. 1, pp. 378-385, Jan 2004.

[48] M. H. Bakr, J. W. Bandler, R. M. Biernacki, S. H. Chen, and K. Madsen, "A trust region aggressive space mapping algorithm for EM optimization", *IEEE Transactions on Microwave Theory and Techniques*, vol. 46, no. 12, pp. 2412-2425, Dec. 1998.

[49] M. H. Bakr, J. W. Bandler, N. Georgieva, and K. Madsen, "A hybrid aggressive space-mapping algorithm for EM optimization", *IEEE Transactions on Microwave Theory and Techniques*, vol. 47, no. 12, pp. 2440-2449, Dec. 1999.

[50] J. W. Bandler, R. M. Biernacki, and S. H. Chen, "Fully automated space mapping optimization of 3D structures", *IEEE MTT-S International Microwave Symposium Digest*, San Francisco, CA, USA, pp. 753-756, 17-21 June 1996.

[51] J. W. Bandler, R. M. Biernacki, S. H. Chen, and D. Omeragic, "Space mapping optimization of waveguide filters using finite element and mode-matching electromagnetic simulators", *International Journal of RF and Microwave Computer-Aided Engineering*, vol. 9, no. 1, pp. 54-70, Jan. 1999.

[52] J. W. Bandler, R. Biernacki, C. Shao Hua, and H. Ya Fei, "Design optimization of interdigital filters using aggressive space mapping and decomposition", *IEEE Transactions on Microwave Theory and Techniques*, vol. 45, no. 5, pp. 761-769, May 1997.

[53] J. W. Bandler, A. S. Mohamed, M. H. Bakr, K. Madsen, and J. Sondergaard, "EM-based optimization exploiting partial space mapping and exact sensitivities", *IEEE Transactions on Microwave Theory and Techniques*, vol. 50, no. 12, pp. 2741-2750, Dec 2002.

[54] J. Bonache, M. Gil, I. Gil, J. Garcia-Garcia, and F. Martin, "On the electrical characteristics of complementary metamaterial resonators", *IEEE Microwave and Wireless Components Letters*, vol. 16, no. 10, pp. 543-545, Oct. 2006.

[55] J. Selga, A. Rodríguez, M. Gil, J. Carbonell, V. E. Boria, and F. Martín, "Synthesis of planar microwave circuits through aggressive space mapping using commercially available software packages", *International Journal of RF and Microwave Computer-Aided Engineering*, vol. 20, no. 5, pp. 527-534, Sep. 2010.

[56] L. J. Rogla, J. E. Rayas-Sanchez, V. E. Boria, and J. Carbonell, "EM-Based Space Mapping Optimization of Left-handed Coplanar Waveguide Filters with Split Ring Resonators", *IEEE MTT-S International Microwave Symposium Digest*, pp. 111-114, 3-8 June 2007.

[57] P. J. Bradley, "Quasi-Newton Model-Trust Region Approach to Surrogate-Based Optimisation of Planar Metamaterial Structures", *Progress In Electromagnetics Research B*, vol. 47, pp. 1-17, 2013.

[58] M. Gil, J. Bonache, J. Selga, J. Garcia-Garcia, and F. Martin, "Broadband resonant-type metamaterial transmission lines", *IEEE Microwave and Wireless Components Letters*, vol. 17, no. 2, pp. 97-99, Feb. 2007.

[59] J. Selga, G. Siso, M. Gil, J. Bonache, and F. Martin, "Microwave circuit miniaturization with Complementary Spiral Resonators: application to high-pass filters and dual-band components", *Microwave and Optical Technology Letters*, vol. 51, no. 11, pp. 2741-2745, Nov. 2009.

[60] M. Gil, J. Bonache, J. Selga, J. Garcia-Garcia, and F. Martin, "High-pass filters implemented by composite right/left handed (CRLH) transmission lines based on complementary split rings resonators (CSRRs)", *PIERS online*, vol. 3, no. 3, pp. 251-253, 2007.

[61] J. Selga, M. Gil, F. Aznar, J. Bonache, and F. Martin, "Composite right-/left-handed coplanar waveguides loaded with split ring resonators and their application to high-pass filters", *IET Microwaves Antennas & Propagation*, vol. 4, no. 7, pp. 822-827, July 2010.

[62] F. Aznar, M. Gil, J. Bonache, L. Jelinek, J. D. Baena, R. Marques, and F. Martin, "Characterization of miniaturized metamaterial resonators coupled to planar transmission lines through parameter extraction", *Journal of Applied Physics*, vol. 104, no. 11, pp. 114501(1) -114501(8), Dec. 2008.

[63] J. Bonache, J. Martel, I. Gil, M. Gil, J. Garcia-Garcia, F. Martin, I. Cairo, and M. Ikeda, "Super compact (< 1cm$^2$) band pass filters with wide bandwidth and high selectivity at C-band", *Proceedings of 36th European Microwave Conference*, Manchester, UK, pp. 177-180, 10-15 Sep. 2006.

[64] J. Bonache, F. Martin, J. Garcia-Garcia, I. Gil, R. Marques, and M. Sorolla, "Ultra wide band pass filters (UWBPF) based on complementary split rings resonators", *Microwave and Optical Technology Letters*, vol. 46, no. 3, pp. 283-286, Aug. 2005.

[65] M. Gil, J. Bonache, and F. Martin, "Ultra compact band pass filters implemented through complementary spiral resonators (CSRs)", *IEEE MTT-S International Microwave Symposium Digest*, Atlanta, GA, USA, pp. 1119-1122, 15-20 June 2008.

[66] J. Garcia-Garcia, F. Martin, F. Falcone, J. Bonache, J. D. Baena, I. Gil, E. Amat, T. Lopetegi, M. A. G. Laso, J. A. M. Iturmendi, M. Sorolla, and R. Marques, "Microwave filters with improved stopband based on sub-wavelength resonators", *IEEE Transactions on Microwave Theory and Techniques*, vol. 53, no. 6, pp. 1997-2006, June 2005.

[67] I. J. Bahl and P. Bhartia, *Microwave Solid State Circuit Design*, 2nd ed. New York, Wiley-Interscience, 2003.

[68] A. Rodriguez, V. E. Boria, J. Selga, and F. Martin, "A robust space mapping method for the practical synthesis of CSRR-based artificial transmission lines from equivalent circuit models", *Proceedings of 42nd European Microwave Conference (EuMC)*, Amsterdam (The Netherlands), pp. 671-674, 28 Oct. - 2 Nov. 2012.

[69] A. Rodriguez, J. Selga, M. Gil, J. Carbonell, V. E. Boria, and F. Martin, "Automated synthesis of resonant-type metamaterial transmission lines using aggressive space mapping", *IEEE MTT-S International Microwave Symposium Digest*, Anaheim,CA, USA, pp. 209-212, 23-28 May 2010.

[70] A. Rodríguez, J. Selga, F. Martín, and V. E. Boria, "Practical Application of Space Mapping Techniques to the Synthesis of CSRR-Based Artificial Transmission Lines", in *Surrogate-Based Modeling and Optimization*, S. Koziel and L. Leifsson, ed. New York Springer 2013, pp. 81-97.

[71] J. E. Rayas-Sanchez and V. Gutierrez-Ayala, "EM-Based Monte Carlo Analysis and Yield Prediction of Microwave Circuits Using Linear-Input Neural-Output Space Mapping", *IEEE Transactions on Microwave Theory and Techniques*, vol. 54, no. 12, pp. 4528-4537, Dec. 2006.

[72] J. Selga, A. Rodriguez, V. E. Boria, and F. Martin, "Synthesis of split rings based artificial transmission lines through a new two-step, fast converging, and robust Aggressive Space Mapping (ASM) algorithm", *IEEE Transactions on Microwave Theory and Techniques*, vol. 61, no. 6, pp. 2295-2308, June 2013.

[73] D. M. Bates and D. G. Watts, *Nonlinear Regression Analysis and Its Applications*, New York, Wiley, 1988.

[74] Agilent Momentum. ver. 8.20.374, Agilent Technologies, 2008.

[75] Ansoft Designer. ver. 6.1.0, Ansys Inc., 2010.

[76] J. Selga, A. Rodriguez, J. Carbonell, V. E. Boria, and F. Martin, "Synthesis of metamaterial transmission lines through aggressive space mapping", *Fourth International Congress on Advanced Electromagnetic Materials in Microwaves and Optics (Metamaterials 2010)*, Karlsruhe (Germany), pp. 690-692, 13-16 Sep. 2010.

[77] M. Makimoto and S. Yamashita, "Compact Bandpass-Filters Using Stepped Impedance Resonators", *Proceedings of the IEEE*, vol. 67, no. 1, pp. 16-19, Jan. 1979.

[78] M. Makimoto and S. Yamashita, "Bandpass-Filters Using Parallel Coupled Stripline Stepped Impedance Resonators", *IEEE Transactions on Microwave Theory and Techniques*, vol. 28, no. 12, pp. 1413-1417, Dec. 1980.

[79] J. Naqui, M. Duran-Sindreu, J. Bonache, and F. Martin, "Implementation of shunt-connected series resonators through stepped-impedance shunt stubs: analysis and limitations", *IET Microwaves Antennas & Propagation*, vol. 5, no. 11, pp. 1336-1342, Aug. 2011.

[80] J. Naqui, "Implementación de resonadores serie en derivación mediante stubs en dericación de salto de impedacia: análisis y limitaciones", *Projecte Final de Carrera d'Enginyeria de Telecomunicació*, June 2010.

[81] T. C. Edwards and M. B. Steer, *Foundations of Interconnect and Microstrip Design, Third Edition*, John Wiley, 2000.

[82] J. Selga, A. Rodriguez, V. E. Boria, and F. Martin, "Application of Aggressive Space Mapping (ASM) to the efficient synthesis of Stepped Impedance Resonators (SIRs)", *Proceedings of 43rd European Microwave Conference (EuMC)*, Nuremberg (Germany), 6-11 Oct. 2013.

# Appendix A

# EM simulator control through MATLAB®

Concerning the EM solver module, mentioned in previous chapters, it is noteworthy that to obtain the frequency response for a given set of geometrical parameters a certain procedure is needed. The aim of this appendix is to describe how MATLAB® software is able to control an EM commercial simulator and transfer the information to the core program of the ASM algorithm.

First of all, it is mandatory to point out that each EM simulator has different ways to define a layout and launch the corresponding simulation. For this reason, we have focused on the one used throughout this thesis, *Agilent Momentum*.

To perform the EM simulation, *Agilent Momentum* needs certain data files to be defined containing the following information: layout coordinates, substrate parameters, simulation options and mesh characteristics.

As it can be seen in Figure A.1, an internal process called *LAY_DRAW* is responsible to create a file with layout coordinates (notice that each shape of the layout is defined as a polygon) from the geometrical variables in the fine model vector, $\mathbf{x}_f$. The main function of the other internal process of the EM solver module (*INIT_EM_SIM* in Figure A.1) is to call *Agilent Momentum* and to obtain a data file containing the

simulation results. To this end, the information of substrate, simulation options and mesh is necessary to be defined previously by means the main program or even manually.

Next step is to obtain the desired S-parameter data from the "ds.txt" file. This task is performed by the *READ_DS* function whose main purpose is to read the dataset file to obtain from it the S-parameter matrix and also the most common related magnitude and phase data, i.e. $mag(S_{11})$, $mag(S_{21})$, $ph(S_{11})$ and $ph(S_{21})$.

Finally, the *PARAM_EXTR* function performs the parameter extraction of the corresponding structure. It consists on computing the parameters of the equivalent circuit model $\mathbf{x}_c$ by means of the S-parameter data provided by the *READ_DS* function through solving the corresponding equations (i.e, in case of CSRR-loaded microstrip lines this function has to solve equations (4.5)-(4.8)).

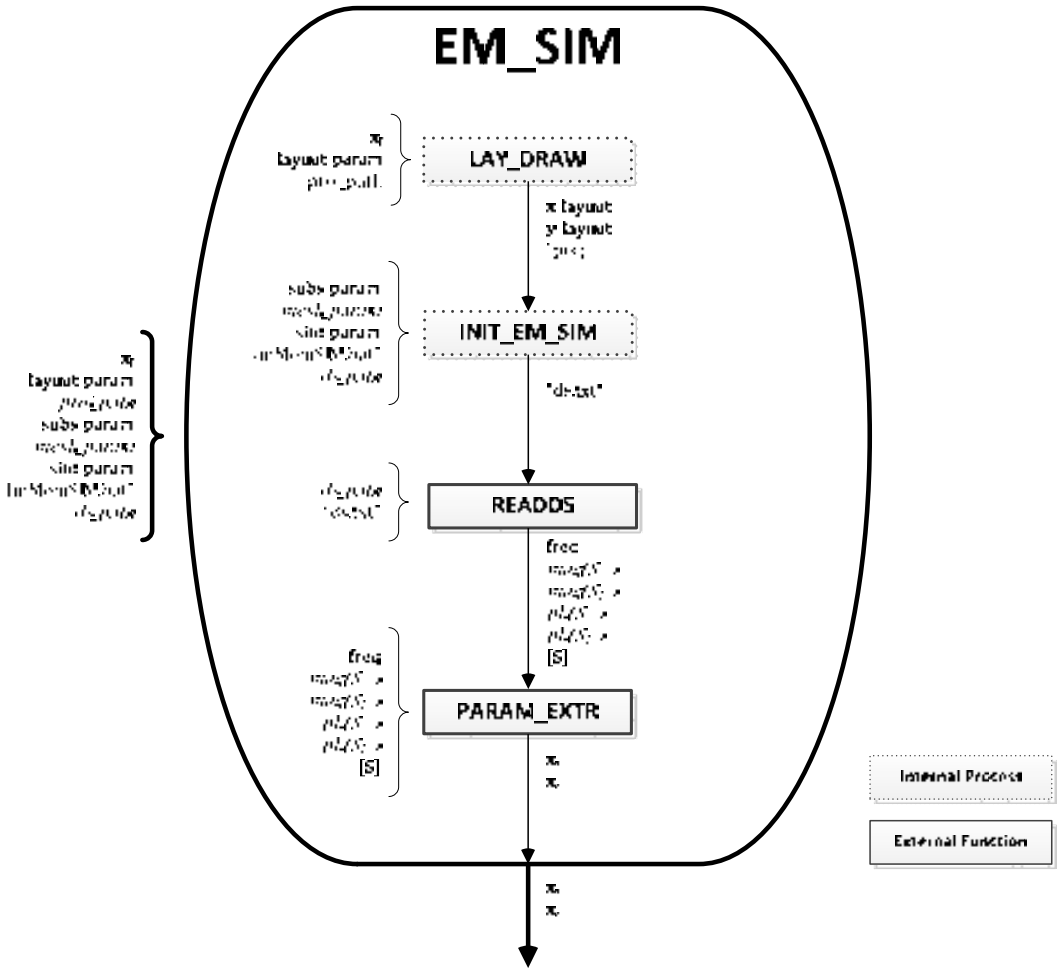


**Figure A.1.** Block diagram of the EM solver module.

# Author list of publications

## International Journals and book chapters

1. M. Gil, J. Bonache, J. Selga, J. Garcia-Garcia, and F. Martin, "Broadband resonant-type metamaterial transmission lines", *IEEE Microwave and Wireless Components Letters*, vol. 17, no. 2, pp. 97-99, Feb. 2007.

2. M. Gil, J. Bonache, J. Selga, J. Garcia-Garcia, and F. Martin, "High-pass filters implemented by Composite Right/Left Handed (CRLH) transmission lines based on Complementary Split Rings Resonators (CSRRs)", *PIERS online*, vol. 3, no. 3, pp. 251-253, 2007.

3. J. Selga, G. Siso, M. Gil, J. Bonache, and F. Martin, "Microwave circuit miniaturization with Complementary Spiral Resonators: application to high-pass filters and dual-band components", *Microwave and Optical Technology Letters*, vol. 51, no. 11, pp. 2741-2745, Nov. 2009.

4. M. Gil, F. Aznar, A. Velez, M. Duran-Sindreu, J. Selga, G. Siso, J. Bonache, and F. Martin, "Electrically small resonators for metamaterial and microwave circuit design", in *Passive Microwave Components and Antennas*, V. Zhurbenko, ed. Dubrovnik (Croacia) InTech, 2010, pp. 403-428.

5. J. Selga, M. Gil, F. Aznar, J. Bonache, and F. Martin, "Composite right-/left-handed coplanar waveguides loaded with split ring resonators and their application to high-pass filters", *IET Microwaves Antennas & Propagation*, vol. 4, no. 7, pp. 822-827, July 2010.

6. J. Selga, A. Rodriguez, M. Gil, J. Carbonell, V. E. Boria, and F. Martin, "Towards the automatic layout synthesis in resonant-type metamaterial transmission lines", *IET Microwaves Antennas & Propagation*, vol. 4, no. 8, pp. 1007-1015, Aug. 2010.

7. J. Selga, A. Rodríguez, M. Gil, J. Carbonell, V. E. Boria, and F. Martín, "Synthesis of planar microwave circuits through aggressive space mapping using commercially available software packages", *International Journal of RF and Microwave Computer-Aided Engineering*, vol. 20, no. 5, pp. 527-534, Sep. 2010.

8. M. Duran-Sindreu, A. Velez, G. Siso, P. Velez, J. Selga, J. Bonache, and F. Martin, "Recent advances in metamaterial transmission lines based on split rings", *Proceedings of the IEEE* vol. 99, no. 10, pp. 1701-1710, Oct. 2011.

9. M. Durán-Sindreu, J. Naqui, J. Selga, P. Vélez, J. Bonache, and F. Martín, "Composite Right/Left Handed Transmission Line Metamaterials", in *Wiley Encyclopedia of Electrical and Electronics Engineering*, ed. John Wiley & Sons, 2013, pp. 1-25.

10. A. Rodríguez, J. Selga, F. Martín, and V. E. Boria, "Practical Application of Space Mapping Techniques to the Synthesis of CSRR-Based Artificial Transmission Lines", in *Surrogate-Based Modeling and Optimization*, ed. Springer New York, 2013, pp. 81-97.

11. J. Selga, A. Rodriguez, V. E. Boria, and F. Martin, "Synthesis of split rings based artificial transmission lines through a new two-step, fast converging, and robust Aggressive Space Mapping (ASM) algorithm", *IEEE Transactions on Microwave Theory and Techniques*, vol. 61, no. 6, pp. 2295-2308, June 2013.

## National and International Conferences

1. M. Gil, J. Bonache, J. Selga, J. Garcia-Garcia, and F. Martin, "High-pass filters implemented by Composite Right/Left Handed (CRLH) transmission lines based on complementary split rings resonators (CSRRs)", *Proceedings of Progress in Electromagnetics Research Symposium (PIERS),* , Beijing (China), pp. 483-485, 26-30 March 2007.

2. J. Selga, M. Gil, G. Siso, J. Bonache, and F. Martin, "Application of Complementary Spiral Resonators (CSRs) to microwave circuit miniaturization", *National Workshop on Metamaterials and Special Materials for Electromagnetic Applications and TL (MMSM)*, Naples (Italy), 18-19 Dec. 2008.

3. J. Selga, F. Aznar, A. Velez, M. Gil, J. Bonache, and F. Martin, "Low-pass and high-pass microwave filters with transmission zero based on metamaterial concepts", *IEEE International Workshop on Antenna Technology: Small Antennas and Novel Metamaterials (IWAT)*, Santa Monica (CA, USA), 2-4 March 2009.

4. J. Selga, M. Gil, F. Aznar, J. Bonache, and F. Martin, "Microwave filters based on composite right/left handed transmission lines", *3rd Young Scientist Meeting on Metamaterials (YSMM'09)*, Leganés (Spain), pp. 305-306, 6-8 July 2009.

5. A. Rodriguez, J. Selga, M. Gil, J. Carbonell, V. E. Boria, and F. Martin, "Automated synthesis of resonant-type metamaterial transmission lines using aggressive space mapping", *IEEE MTT-S International Microwave Symposium Digest*, Anaheim,CA, USA, pp. 209-212, 23-28 May 2010.

6. J. Selga, A. Rodriguez, J. Carbonell, V. E. Boria, and F. Martin, "Synthesis of metamaterial transmission lines through aggressive space mapping", *Fourth International Congress on Advanced Electromagnetic Materials in Microwaves and Optics (Metamaterials 2010)*, Karlsruhe (Germany), pp. 690-692, 13-16 Sep. 2010.

7. J. Naqui, A. Fernandez-Prieto, M. Duran-Sindreu, J. Selga, F. Medina, F. Mesa, and F. Martin, "Split rings-based differential transmission lines with common-mode suppression", *IEEE MTT-S International Microwave Symposium Digest*, Baltimore, MD,USA, pp. 1-4, 5-10 June 2011.

8. A. Rodriguez, J. Selga, F. Martin, and V. E. Boria, "A more robust approach for the automated synthesis of artificial transmission lines combining Aggressive Space Mapping with line search", *4th Young Scientist Meeting on Metamaterials (YSMM'11)*, Valencia (Spain), 14-16 Feb. 2011.

9. J. Selga, A. Rodriguez, V. E. Boria, and F. Martin, "Application of aggressive space mapping to the synthesis of composite right/left handed (CRLH) transmission lines based on complementary split ring resonators (CSRRs)", *Proceedings of 41st European Microwave Conference (EuMC)*, Manchester (UK), pp. 968-971, 10-13 Oct. 2011.

10. J. Selga, A. Rodriguez, V. E. Boria, and F. Martin, "Automated parameter extractor for metamaterial transmission lines based on Complementary Split Ring Resonators (CSRRs) ", *4th Young Scientist Meeting on Metamaterials (YSMM'11)*, Valencia (Spain), 14-16 Feb. 2011.

11. A. Rodriguez, V. E. Boria, J. Selga, and F. Martin, "A robust space mapping method for the practical synthesis of CSRR-based artificial transmission lines from equivalent circuit models", *Proceedings of 42nd European Microwave Conference (EuMC)*, Amsterdam (The Netherlands), pp. 671-674, 28 Oct. - 2 Nov. 2012.

12. J. Selga, A. Rodriguez, V. E. Boria, and F. Martin, "Application of Aggressive Space Mapping (ASM) to the efficient synthesis of Stepped Impedance Resonators (SIRs)", *Proceedings of 43rd European Microwave Conference (EuMC)*, Nuremberg (Germany), 6-11 Oct. 2013.